



Synthesis and properties of some electrolyte additives and electrode materials for lithium-ion batteries

by

Derrick Oupa Sipoyo 11640815

Dissertation submitted for the degree Master of Science in **Chemistry**

School of Mathematical and Natural Sciences

Department of Chemistry

University of Venda

Thohoyandou, Limpopo

South Africa

Supervisor: Prof. T. van Ree




Co-Supervisor: Dr G.F. Ndlovu



Declaration

I, Derrick Oupa Sipoyo, hereby declare that the dissertation for Master of Science (Chemistry) degree at the University of Venda, hereby submitted by me, has not been submitted for any other degree at any other university or tertiary institution. The report does not contain any other persons' writing unless specifically acknowledged and referenced accordingly.

Signed (Student):



Date: 28/04/2021

Derrick Sipoyo

Abstract

Acceptable energy storage technologies are needed for the transition from fossil fuels to renewable energy sources, which can be expected to take place over the next 30 years. Lithium-ion batteries are used extensively but are limited by safety, cycle life, and the availability of materials. This study was aimed at contributing to the development of lithium-ion power sources by synthesizing bifunctional organic electrolyte additives and electrode materials. The bifunctional organic electrolyte additives 2-((2,2-dimethyl-3,6,9,12-tetraoxa-2silatetradecan-14-yl)oxy)-1,3-dihydrobenzo[d][1,3,2]diazaphosphole 2-oxide (DTSDP) and 2-phenylbenzo[d][1,3,2]dioxaborole were characterized by NMR spectroscopy; using these additives will be advantageous in improving the safety of the lithium-ion batteries (LIBs). Because of the presence of groups such as phosphate which is known to have fire retardant properties, and nitrogen within the structure which at high temperature will produce by-product N_2 providing thermal insulation. Li_3VO_4 (LVO) was doped with five different metal ions (i.e., silver (Ag^+), cerium (Ce^{3+}), chromium (Cr^{3+}), magnesium (Mg^{2+}), and zinc (Zn^{2+})) at doping levels $0.05 \leq x \leq 0.5$ using sol-gel methodology, and characterized by XRD, SEM, and EDX. Incorporation of dopants into the LVO orthorhombic crystal structure at low concentration ($x \leq 0.1$) was successful for all the metal ions. However, for the ions $Ag(I)$, $Ce(III)$, $Mg(II)$, and $Zn(II)$ with ionic radii greater than that of $V(V)$ (0.355 \AA) doping with $x \geq 10\%$ was not beneficial for LVO as phase purity deteriorated, as shown by their XRD showing dopant oxide peaks. Chromium doping was the most successful since it did not show any secondary phase; even at high concentrations it was well incorporated in the orthorhombic crystal structure. Microstructures seen in the SEM showed that the size of particles decreases with increased concentration of the dopants and particles become more defined and uniform at high dopant concentration.

Keywords: *Electrochemistry, Electrolyte, Electrolyte additive, Lithium-ion battery, Lithium vanadium oxide, Electrode material.*

ACRONYMS AND ABBREVIATIONS

CV	Cyclic voltammetry
DMC	Dimethyl carbonate
EC	Ethylene carbonate
EIS	Electrochemical impedance spectroscopy
FTIR	Fourier transform infrared spectroscopy
GHG	Greenhouse gas
HOMO	Highest occupied molecular orbital
IPPP	4-Isopropylphenyl diphenyl phosphate
IR	Infrared spectroscopy
LIB	Lithium-ion battery
LMO	Lithium manganese oxide
LVO	Li_3VO_4
LUMO	Lowest unoccupied molecular orbital
NMC	Lithium nickel manganese cobalt oxide
NMR	Nuclear magnetic resonance spectroscopy
PC	Propylene carbonate
PES	Photoelectron spectroscopy
SEI	Solid-electrolyte Interphase
SEM	Scanning electron microscopy
TGA	Thermogravimetric analysis
Wh	Watt-hour (electrical energy equivalent to the power consumption of one watt for one hour)
XRD	X-ray diffraction

List of figures and schemes

Figure 1.1	Comparison of the different battery technologies in terms of volumetric and gravimetric energy density (Tarascon and Armand, 2011).	2
Figure 1.2	Incidents resulting from faults with LIBs (Brain, 2006; Minter, 2017; Tweed, 2013).	2
Figure 1.3	The world's major vanadium-producing countries (Bushveld Mineral Ltd., 2018).	3
Figure 2.1	Lead-acid battery (Peng, 2011).	6
Figure 2.2	Processes occurring during charge and discharge of LIBs (Bruce <i>et al.</i> , 2008).	8
Figure 2.3	Applications of lithium-ion batteries (Yoo <i>et al.</i> , 2014).	9
Figure 2.4	Schematic of thermal runaway stages of lithium-ion batteries (Liu <i>et al.</i> , 2018).	11
Figure 2.5	Crystal structures of (a) lithiated graphite (Yamada <i>et al.</i> , 2014); (b) lithium titanate (LTO) (Teshima <i>et al.</i> , 2011); and (c) silicon during lithiation (Chan <i>et al.</i> , 2012).	13
Figure 2.6	Crystal structure of orthorhombic Li_3VO_4 (Zeng <i>et al.</i> , 2017).	14
Figure 2.7	Schematic drawing of the solid-electrolyte interface (SEI) (Verma <i>et al.</i> , 2010).	18
Scheme 2.1	The two competing mechanisms for the formation of SEI in carbonate solvents (Zhang, 2006)	19
Scheme 2.2	Coordination of lithium ions with organic carbonate ions.	19
Scheme 2.3	Examples of electropolymerisable additives.	20
Figure 2.8	Typical examples of CC-CV charging curves of a lithium-ion battery (Wang <i>et al.</i> , 2018).	22
Figure 2.9	(a) Voltage profile applied in a cyclic voltammetry measurement; (b) current response versus voltage curve (Yang and Rogach., 2019).	23
Figure 2.10	(a) Applied current profile; (b) typically recorded voltage response versus capacity curves (Yang and Rogach., 2019).	23
Figure 2.11	(a) Electrical circuit model of the Li-ion battery (Buller <i>et al.</i> , 2005); and (b) typical EIS of a cell at 25°C and 50% state of charge (SOC) (Jiang <i>et al.</i> , 2017).	24
Figure 2.12	Overcharge protection mechanism by a redox shuttle molecule S (Zhang <i>et al.</i> , 2011).	26
Figure 4.1	TGA of representative samples: (a) LVO with starch template; (b) 1% Cu doped LVO on starch.	35
Figure 4.2	(a) XRD pattern of $\text{Li}_3\text{V}_{(1-x)}\text{Ag}_x\text{O}_4$ ($x = 0.0, x = 0.01, x = 0.05, x = 0.1, x = 0.3$ and $x = 5$); (b) enlargement of the XRD pattern between 28° and 31° 2 θ values.	37
Figure 4.3	Typical results of Rietveld refinement: (a) $\text{Li}_3\text{V}_{0.99}\text{Ag}_{0.01}\text{O}_4$; (b) $\text{Li}_3\text{V}_{0.99}\text{Ag}_{0.01}\text{O}_4$; (c) $\text{Li}_3\text{V}_{0.99}\text{Ag}_{0.01}\text{O}_4$.	38
Figure 4.4	Crystal structures of $\text{Li}_3\text{V}_{(1-x)}\text{Ag}_x\text{O}_4$ samples for (a) $x = 0$ and (b) $x = 0.01$. Blue atoms = Vanadium, Purple atoms = Lithium, Red atoms = Oxygen and Black atom parts = Silver	39
Figure 4.5	The SEM images of $\text{Li}_3\text{V}_{1-x}\text{Ag}_x\text{O}_4$ samples: (a) $x = 0$, (b) $x = 0.01$, (c) $x = 0.3$, (d) $x = 0.5$.	40
Figure 4.6	(a) EDS mappings of related elements for $\text{Li}_3\text{V}_{1-x}\text{Ag}_x\text{O}_4$ ($x = 0.01$); EDS spectra of Li_3VO_4 and (c) $\text{Li}_3\text{V}_{0.99}\text{Ag}_{0.01}\text{O}_4$.	41
Figure 4.7	(a) XRD pattern of $\text{Li}_3\text{V}_{(1-x)}\text{Ce}_x\text{O}_4$ ($x = 0.0, x = 0.05, x = 0.1, x = 0.3$ and $x = 0.5$); (b) enlargement of the XRD pattern between 35° and 38° 2 θ values	42

Figure 4.8	Typical results of Rietveld refinement of $\text{Li}_3\text{V}_{(1-x)}\text{Ce}_x\text{O}_4$: (a) $x = 0.0$; (b) $x = 0.01$; (c) $x = 0.5$.	44
Figure 4.9	Crystal structures of $\text{Li}_3\text{V}_{(1-x)}\text{Ce}_x\text{O}_4$ samples for (a) $x = 0$; (b) $x = 0.05$; (c) $x = 0.5$. Blue atoms = Vanadium, Purple atoms = Lithium, Red atoms = Oxygen, and Orange atom parts = Cerium.	45
Figure 4.10	SEM images of $\text{Li}_3\text{V}_{1-x}\text{Ce}_x\text{O}_4$ samples: (a) $x = 0$, (b) $x = 0.01$, (c) $x = 0.3$, (d) $x = 0.5$.	46
Figure 4.11	(a) EDS mappings of related elements for $\text{Li}_3\text{V}_{1-x}\text{Ce}_x\text{O}_4$ ($x = 0.01$); EDS spectra of $\text{Li}_3\text{V}_{0.99}\text{Ce}_{0.01}\text{O}_4$ and (c) $\text{Li}_3\text{V}_{0.5}\text{Ce}_{0.5}\text{O}_4$.	47
Figure 4.12	(a) XRD pattern of $\text{Li}_3\text{V}_{(1-x)}\text{Cr}_x\text{O}_4$ ($x = 0.0$, $x = 0.05$, $x = 0.1$, $x = 0.3$ and $x = 0.5$); (b) enlargement of the XRD pattern between 35° and 38° 2θ values.	48
Figure 4.13	Typical results of Rietveld refinement of $\text{Li}_3\text{V}_{(1-x)}\text{Cr}_x\text{O}_4$: (a) $x = 0$; (b) $x = 0.05$; (c) $x = 0.5$.	50
Figure 4.14	Crystal structures of $\text{Li}_3\text{V}_{(1-x)}\text{Cr}_x\text{O}_4$ samples for (a) $x = 0$; (b) $x = 0.05$; (c) $x = 0.5$. Blue atoms = Vanadium, Purple atoms = Lithium, Red atoms = Oxygen and Dark Blue atom parts = Chromium.	51
Figure 4.15	The SEM images of $\text{Li}_3\text{V}_{1-x}\text{Cr}_x\text{O}_4$ samples: (a) $x = 0$, (b) $x = 0.01$, (c) $x = 0.3$, (d) $x = 0.5$.	53
Figure 4.16	(a) EDS mappings of elements of $\text{Li}_3\text{V}_{1-x}\text{Cr}_x\text{O}_4$ ($x = 0.01$); EDS spectra of (b) $\text{Li}_3\text{V}_{0.95}\text{Cr}_{0.05}\text{O}_4$ and (c) $\text{Li}_3\text{V}_{0.5}\text{Cr}_{0.5}\text{O}_4$.	54
Figure 4.17	(a) XRD pattern of $\text{Li}_3\text{V}_{1-x}\text{Mg}_x\text{O}_4$ ($x = 0.0$, $x = 0.05$, $x = 0.1$, $x = 0.3$ and $x = 0.5$); (b) enlargement of the XRD pattern between 35° and 38° 2θ values.	56
Figure 4.18	Typical results of Rietveld refinement of $\text{Li}_3\text{V}_{1-x}\text{Mg}_x\text{O}_4$: (a) $x = 0.0$, (b) $x = 0.01$, and (c) $x = 0.5$.	57
Figure 4.19	(a) Crystal structures of $\text{Li}_3\text{V}_{1-x}\text{Mg}_x\text{O}_4$ samples for $x = 0$, $x = 0.05$ and $x = 0.5$, Blue atoms = Vanadium, Purple atoms = Lithium, Red atoms = Oxygen and Green atom = Magnesium.	58
Figure 4.20	SEM images of $\text{Li}_3\text{V}_{1-x}\text{Mg}_x\text{O}_4$ samples: (a) $x = 0$, (b) $x = 0.01$, (c) $x = 0.3$, (d) $x = 0.5$.	59
Figure 4.21	(a) EDS mappings of the elements of $\text{Li}_3\text{V}_{1-x}\text{Mg}_x\text{O}_4$ ($x = 0.01$); EDS spectra of (b) $\text{Li}_3\text{V}_{0.95}\text{Mg}_{0.05}\text{O}_4$ and (c) $\text{Li}_3\text{V}_{0.5}\text{Mg}_{0.5}\text{O}_4$.	60
Figure 4.22	(a) XRD pattern of $\text{Li}_3\text{V}_{1-x}\text{Zn}_x\text{O}_4$ ($x = 0.0$, $x = 0.05$, $x = 0.1$, $x = 0.3$, and $x = 0.5$); (b) enlargement of the XRD pattern between 35° and 38° 2θ values.	62
Figure 4.23	Typical results of Rietveld refinement of $\text{Li}_3\text{V}_{1-x}\text{Zn}_x\text{O}_4$: (a) $x = 0.0$, (b) $x = 0.01$, (c) $x = 0.5$.	63
Figure 4.24	Crystal structures of $\text{Li}_3\text{V}_{1-x}\text{Zn}_x\text{O}_4$ samples for (a) $x = 0$; (b) $x = 0.05$; (c) $x = 0.5$, respectively. Blue atoms = Vanadium, Purple atoms = Lithium, Red atoms = Oxygen and Grey atom = Zinc.	64
Figure 4.25	SEM images of $\text{Li}_3\text{V}_{1-x}\text{Zn}_x\text{O}_4$ samples: (a) $x = 0$, (b) $x = 0.01$, (c) $x = 0.3$, (d) $x = 0.5$.	65
Figure 4.26	(a) EDS mappings of related elements for $\text{Li}_3\text{V}_{1-x}\text{Zn}_x\text{O}_4$ ($x = 0.01$); EDS spectra of (b) $\text{Li}_3\text{V}_{0.95}\text{Zn}_{0.05}\text{O}_4$ and (c) $\text{Li}_3\text{V}_{0.5}\text{Zn}_{0.5}\text{O}_4$.	66

List of tables

Table 4.1 The key structure parameters of $\text{Li}_3\text{V}_{0.99}\text{Ag}_{0.01}\text{O}_4$ ($x = 0.01$) obtained by Rietveld refinement.	39
Table 4.2 Calculated lattice parameters of $\text{Li}_3\text{V}_{(1-x)}\text{Ag}_x\text{O}_4$ samples, based on XRD data refinement.	39
Table 4.3 Semi-quantitative energy dispersive X-ray microanalysis (wt.%) of the EDS for all the samples.	40
Table 4.4 The key structure parameters of $\text{Li}_3\text{V}_{0.99}\text{Ce}_{0.01}\text{O}_4$ ($x = 0.01$) obtained by Rietveld refinement.	43
Table 4.5 Calculated lattice parameters of $\text{Li}_3\text{V}_{(1-x)}\text{Ce}_x\text{O}_4$ samples, based on XRD data refinement.	45
Table 4.6 Semi-quantitative energy dispersive X-ray microanalysis (wt.%) of the EDS for all the samples.	47
Table 4.7 The key structure parameters of $\text{Li}_3\text{V}_{0.99}\text{Cr}_{0.01}\text{O}_4$ ($x = 0.01$) obtained by Rietveld refinement.	49
Table 4.8 Calculated lattice parameters of $\text{Li}_3\text{V}_{(1-x)}\text{Cr}_x\text{O}_4$ samples, based on XRD data refinement.	52
Table 4.9 Semi-quantitative energy dispersive X-ray microanalysis (wt.%) of the EDS for all the samples.	53
Table 4.10 The key structure parameters of $\text{Li}_3\text{V}_{0.99}\text{Mg}_{0.01}\text{O}_4$ ($x = 0.01$) obtained by Rietveld refinement.	55
Table 4.11 Calculated lattice parameters of $\text{Li}_3\text{V}_{1-x}\text{Mg}_x\text{O}_4$ samples, based on XRD data refinement.	56
Table 4.12 Semi-quantitative energy dispersive X-ray microanalysis (wt.%) of the EDS for all the samples.	60
Table 4.13 The key structure parameters of $\text{Li}_3\text{V}_{0.99}\text{Zn}_{0.01}\text{O}_4$ ($x = 0.01$) obtained by Rietveld refinement.	62
Table 4.14 Calculated lattice parameters of $\text{Li}_3\text{V}_{1-x}\text{Zn}_x\text{O}_4$ samples, based on XRD data refinement.	64
Table 4.15 Semi-quantitative energy dispersive X-ray microanalysis (wt.%) of the EDS for all the samples.	66

Acknowledgments

1. I would like to express my deep sense of gratitude to my supervisor Prof Teuns van Ree for his continuous guidance and supervision throughout the course of the study. I would like to thank him for his continuous support, useful discussions, and encouragement which made me enjoy and fall in love more with the study.
2. The University of Venda, National Research Foundation (NRF), and SASOL Inzalo Foundation are thanked for the financial support during the study.
3. I would like to thank my co-supervisor Dr. G.F. Ndlovu for the contribution and support, together with MINTEK (Advanced Material Division) staff for assistance with XRD and SEM/EDS analysis.
4. I would like to express my deep sense of gratitude to my late grandmother Jessie Lina Masina for her love and support.
5. Special thanks to my parents Gloria Mokutoane and Lucky Sipoyo, my siblings Phindile Mfobela, Gift Jamekwane, Jessies Jamekwane, and Mthetheleli Mokutoane for their care and believing in me throughout my studies.
6. Special thanks to my girlfriend Ntiyiso Privy Hlungwani for her support, prayers, and keeping her faith in me always.
7. Finally, I would like to thank the Author and Finisher, the almighty God in the Name of Jesus, for His Love, mercy, grace, and for protection toward me, and everyone who contributed to the study.

Table of Contents

Declaration.....	i
Abstract	ii
ACRONYMS AND ABBREVIATIONS	iii
List of figures and schemes	iv
List of tables	vi
Acknowledgments.....	vii
1. Introduction	1
1.1 Background.....	1
1.2 Problem statement.....	3
1.3 Aims and objectives	4
2. Literature Review	5
2.1 Lithium-ion battery principles.....	5
2.2 The electrolyte in lithium-ion batteries.....	9
2.3 Negative electrode materials.....	11
2.4 Positive electrode materials	15
2.5 The solid-electrolyte interphase	17
2.6 Battery charge-discharge cycling	21
2.7 Protecting electrode materials against decay and overcharge	25
3. Experimental.....	29
3.1 General Experimental Conditions.....	29
3.2 Synthesis of organic electrolyte additives	29
3.2.1 Synthesis of 2-((2,2-dimethyl-3,6,9,12-tetraoxa-2-silatetradecan-14yl)oxy)- 1,3-dihydrobenzo[d][1,3,2]diazaphosphole 2-oxide.....	29
3.2.2 2-Phenylbenzo[d][1,3,2]dioxaborole	30
3.3 Synthesis of new electrode materials.....	31
3.3.1 Synthesis of Li_3VO_4 using the sol-gel method	31
3.3.2 Synthesis of doped $\text{Li}_3\text{V}_{1-x}\text{M}_x\text{O}_4$ using the sol-gel method.....	31

3.4 Characterization of electrode materials and electrolyte additives	32
4. Results and Discussion	33
4.1 Electrolyte additives	33
4.1.1 2-((2,2-Dimethyl-3,6,9,12-tetraoxa-2-silatetradecan-14-yl)oxy)-1,3-dihydrobenzo[d][1,3,2]diazaphosphole 2-oxide	33
4.1.2 2-Phenylbenzo[d][1,3,2]dioxaborole	34
4.2 Electrode Materials	34
4.2.1 Thermogravimetric Analysis	34
4.2.2 Silver Doped Lithium Vanadates, $\text{Li}_3\text{V}_{1-x}\text{Ag}_x\text{O}_4$	35
4.2.3 Cerium Doped Lithium Vanadates, $\text{Li}_3\text{V}_{1-x}\text{Ce}_x\text{O}_4$	41
4.2.4 Chromium Doped Lithium Vanadates, $\text{Li}_3\text{V}_{1-x}\text{Cr}_x\text{O}_4$	48
4.2.5 Magnesium Doped Lithium Vanadates, $\text{Li}_3\text{V}_{1-x}\text{Mg}_x\text{O}_4$	54
4.2.6 Zinc Doped Lithium Vanadates, $\text{Li}_3\text{V}_{1-x}\text{Zn}_x\text{O}_4$	61
5. Conclusions and Future Work.....	67
References.....	68
Appendix A NMR Spectra of 2-((2,2-dimethyl-3,6,9,12tetraoxa-2-silatetradecan-14-yl)oxy)-,3-.....	76
Appendix B NMR Spectra of 2-phenylbenzo[d][1,3,2]dioxaborole.....	79

1. Introduction

1.1 Background

About eighty-six percent of the world's energy needs are provided by non-renewable resources ("fossil fuels") such as coal, crude oil, and natural gas (World Energy Council, 2018). However, there is a rapidly increasing gap between fossil energy supply and demand. The explanation of this imbalance points to an increase in population, rising living standards, and technological advancements (Gautam *et al.*, 2019). Moreover, when fossil fuels are combusted, carbon dioxide and other combustion products trap heat in the atmosphere, resulting in global warming and climate change. Significant efforts have been made to minimize environmental impact and balance the energy gap between supply and demand by the development of renewable energy technologies such as biofuels, fuel cells, wind turbines, and solar cells. Of the different electrochemical energy storage systems, the lithium-ion battery is considered in the following discussion.

Lithium-ion batteries (LIBs) are of great importance as they are currently the preferred energy source for portable electric devices because of their rechargeable property, being lightweight, and having a high volumetric and gravimetric energy density. LIBs are also being developed as power sources for electric vehicles since they have a higher energy density than competitive technologies such as nickel-metal hybrid systems, as shown in Figure 1.1. Electric vehicles are a good alternative for petrol and diesel vehicles since they significantly contribute to reducing greenhouse gas (GHG) emissions and air pollution.

In addition, factors such as energy density, rate capability, working voltage, cost of materials, and safety issues of LIBs still confine their commercial application. Incidents such as fire and explosion of the Samsung Galaxy Note 7, Tesla Model S, laptops, etc. which were due to faulty wiring resulting in external short circuits, cell defects resulting from lithium dendrites, and overcharging which results in a thermal runaway (Figure 1.2), have attracted mass media attention and have brought uncertain-

ty on the future of LIBs. Battery safety can be ensured by two mechanisms - external or internal protection. The internal protection scheme focuses on improving battery safety by improving the material used in the battery, for example by coating electrodes or adding electrolyte additives to decrease flammability. External protection depends on electronic devices that can be installed in the battery to monitor battery behavior, such as pressure valves and temperature sensors (Lui *et al.*, 2018).

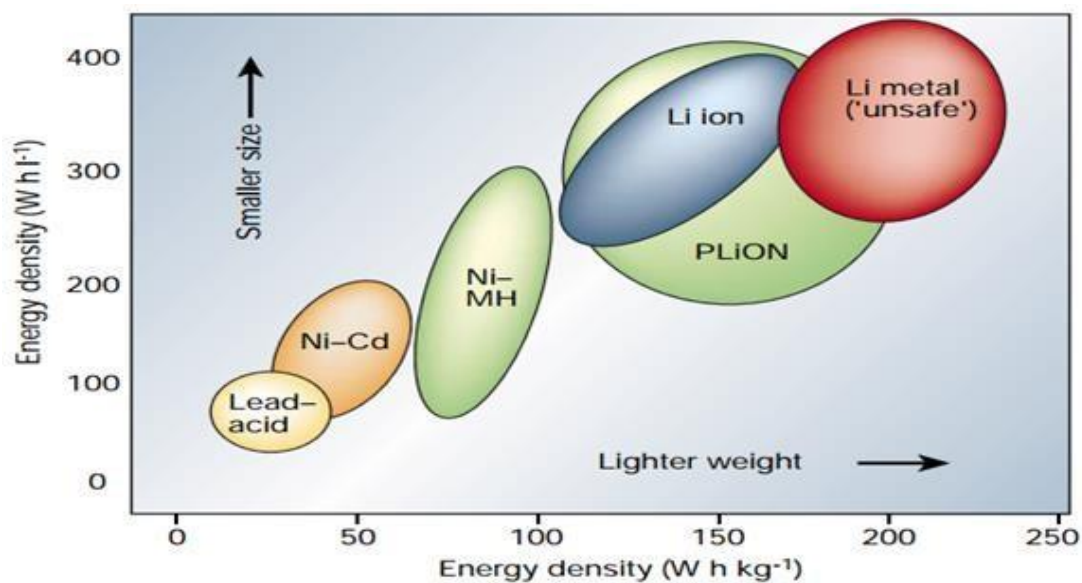


Figure 1.1 Comparison of the different battery technologies in terms of volumetric and gravimetric energy density (Tarascon and Armand, 2011).



Figure 1.2 Incidents resulting from faults with LIBs (Brain, 2006; Minter, 2017; Tweed, 2013).

This work is motivated by the need for improvement of internal protection and improvement schemes by investigating the effect of additives and dopants on the electrochemical performance and structural properties of novel Li_3VO_4 (LVO) materials. They are currently promising negative electrode materials for LIBs, as LVO has a higher specific capacity than several other transition metal-based electrode materials. Furthermore, vanadium is also a readily available metal in South Africa, with South Africa ranked number 3 producer globally (Figure 1.3); this will help in reducing the battery cost since electrode costs are one of the drivers of battery costs.

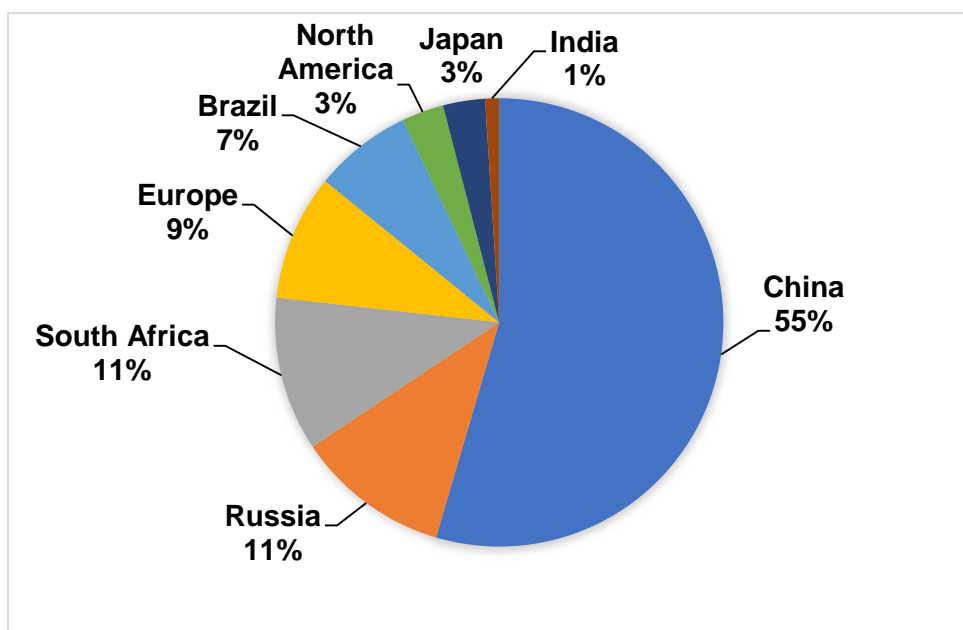


Figure 1.3 The world's major vanadium-producing countries (Bushveld Mineral Ltd., 2018).

1.2 Problem statement

The development of lithium-ion batteries has been very rapid since their appearance in the early 1990s due to several dominant advantages over the traditional rechargeable batteries, such as high output voltage, high energy density, freedom of memory effects, and long cycling life, and they are also relatively benign to the environment. However, in the case of large-scale applications as a power source, the safety problem becomes serious. The main reason is that the liquid electrolyte will react with the cathode materials at high current densities, leading to the production of high thermal enthalpy and thermal run-away. It is very important to find new kinds of

electrode materials (TED, 2012; Whitacre, 2012), electrolyte additives (Armand and Tarascon, 2008; Haregewoin *et al.*, 2016), and polymer electrolytes to reduce this thermal production.

1.3 Aims and objectives

The main aim of this study is to find new electrode materials and organic electrolyte additives to try to improve the performance and safety behavior of lithium-ion power sources, providing a better way for the commercial production of electric vehicles.

This study, therefore, seeks to achieve the following objectives:

- Synthesis of a series of novel bifunctional organic compounds by linking known electrolyte additives.
- Chemical and electrochemical characterization of the synthesized organic additives using a standard electrolyte solution and electrodes.
- Synthesis and characterization of undoped Li_3VO_4 and doped $\text{Li}_3\text{V}_{1-x}\text{M}_x\text{O}_4$ (where the dopants $\text{M} = \text{Cr}, \text{Zn}, \text{Mg}, \text{Ag}, \text{and Ce}$).
- Determination of the effect of dopants ($\text{Cr}, \text{Zn}, \text{Mg}, \text{Ag}, \text{and Ce}$) on the particle morphology, particle size, and electrochemical properties of LVO electrode materials.

2. Literature Review

2.1 Lithium-ion battery principles

A galvanic cell is a single unit device that converts chemical energy into electrical energy, while a collection of electrochemical cells that are connected in series or in parallel forms a battery. Each cell in the battery consists of two electrodes that are separated by a separator and soaked in an electrolyte which promotes the movement of ions. This is done by means of an electrochemical oxidation-reduction reaction of its active materials; the process involves the transfer of electrons from one material to another through an electric circuit, with its scale in energy ranging from nano- to mega-Wh (Wu *et al.*, 2015). In this report, for simplicity, the term battery will be used as equivalent to the cell.

The first true battery was invented by Alessandro Volta in 1800 (Scrosati, 2011). It consisted of alternating zinc and copper discs, with pieces of cardboard soaked in brine between the metallic disks; this voltaic pile produced an electrical current (Wu *et al.*, 2015).

Batteries or cells are divided into two types, primary and secondary. Primary batteries are non-rechargeable and can only provide one continuous or intermittent discharge. Usually, the electrochemical reaction is irreversible and chemical energy can only be transformed into electric energy via the outer circuit (Wu *et al.*, 2015). The first primary cell was the Leclanché cell, invented in 1866 by Georges Leclanché (Wu *et al.*, 2015). It is also known as the “zinc-carbon dry cell” and has a capacity of 1.5 V; once discharged it cannot be charged nor used again. It is used commercially in radios, cameras, flashlights, and most toys. Primary batteries developed from the Zn-C dry cell to modern-day Zn-MnO₂ cells and other primary battery chemistries, such as alkali-manganese, lithium iron disulphide (Li-FeS₂), lithium-thionyl chloride (LiSOCl₂), lithium manganese dioxide (MnO₂ or Li-M), etc. (Linden *et al.*, 2002). The current primary cells have a graphite cathode in an alkaline MnO₂ mixture with carbon kept moist in ammonium chloride electrolyte. The anode is zinc, which forms the container. When the battery is used, electrons flow through the external circuit from the anode to the cathode; this causes the anode to be oxidized and the cathode

to be reduced. Inside the cell in the electrolyte, anions migrate to the anode and cations migrate to the cathode (Cultu, 2009). The discharge reactions for the Leclanché cell are given in Equations 2.1-2.3:

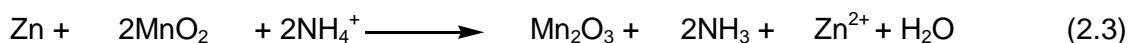
Anode reaction (oxidation, electron generation):



Cathode reaction (reduction, electron consumption):



Overall reaction (cell discharge reaction):



The above reactions are not easily reversible.

Secondary batteries can be repeatedly charged and discharged. To achieve this, their electrochemical reactions must be reversible (Wu *et al.*, 2015). The basic technology of the first rechargeable battery was invented by Gaston Planté in 1859; it was based on lead-acid chemistry. The rechargeable battery contained lead (Pb) as an anode, lead dioxide (PbO_2) as cathode, and an electrolyte dilute sulphuric acid [$\text{H}_2\text{SO}_4(\text{aq})$] (Figure 2.1).

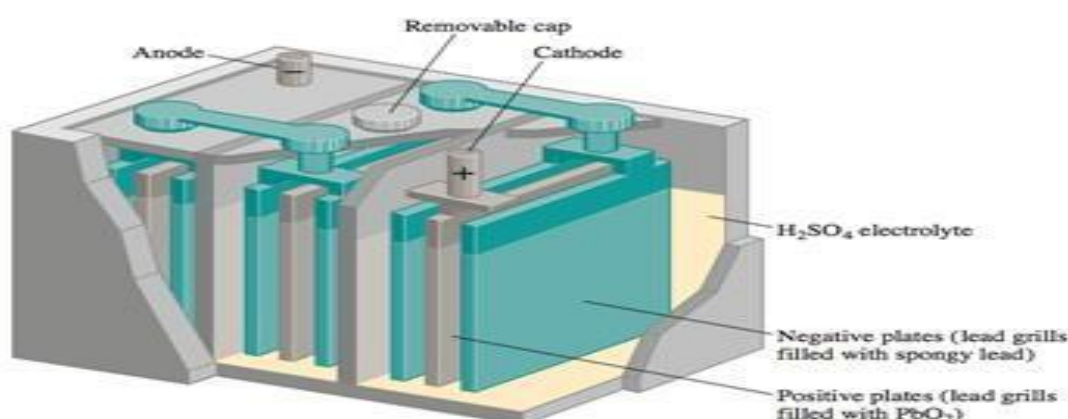
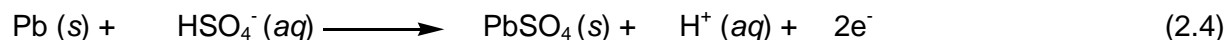


Figure 2.1 Lead-acid battery (Peng, 2011).

The chemical reactions that are taking place are complex but can be summarized as in Equations 2.4 -2.6

Anode reaction (oxidation, electron generation):



Cathode reaction (reduction, electron consumption):



Overall reaction (cell discharge reaction):



Since then there have been many improvements of this invention, but the operating principles remain the same; some other examples of these batteries are nickel-cadmium, lithium-ion, lithium-sulphur, sodium-ion, sodium-sulphur silver-zinc, etc. (Linden *et al.*, 2002; MacFarlane *et al.*, 1999; Ji *et al.*, 2009).

Though lithium is rarely found in nature as a pure metal, it is a lightweight metal, highly reactive, and can be easily electrochemically alloyed with metallic and semimetallic elements (Mo *et al.*, 2017). The physical and chemical properties of lithium are highly suitable for rechargeable battery technology and facilitate very high energy densities (Figure 1.2). Energy density is defined as the total amount of energy (measured in Watt-hours) in a system per unit volume (liter) or unit mass (kg). In comparison with other battery technologies, it has been found that LIBs are stable over more than 500 charge-discharge cycles, can be manufactured in different sizes, and require little maintenance (Roy and Srivastava, 2015).

LIBs are made up of one or more cells and each cell is made of four components: the electrolyte, a separator, anode (negative electrode), and cathode (positive electrode). In most cases, the electrolyte varies with the type of the battery, while the cathode is made of mixed lithium oxides such as lithium iron(II) phosphate (LiFePO_4) (Yang *et al.*, 2002), lithium cobalt(III) oxide (LiCoO_2), and lithium manganese(III/IV) oxide (LiMn_2O_4), and the anode is usually made of carbon (graphite), $\text{Li}_4\text{Ti}_5\text{O}_{12}$,

lithium metal, or Li_3VO_4 (LVO), which will be discussed in this report, as well as other components and their improvements.

During operation, two processes occur charge and discharge. During the charging process, there is intercalation of lithium ions in the anode and deintercalation from the cathode of the battery (Whittingham, 1978), whereas during discharging the lithium ions move from the anode to the cathode through the electrolyte. Electrons move in the opposite direction in the external circuit (Figure 2.2) and the electrode reactions can be expressed as shown in Equations 2.7-2.9:

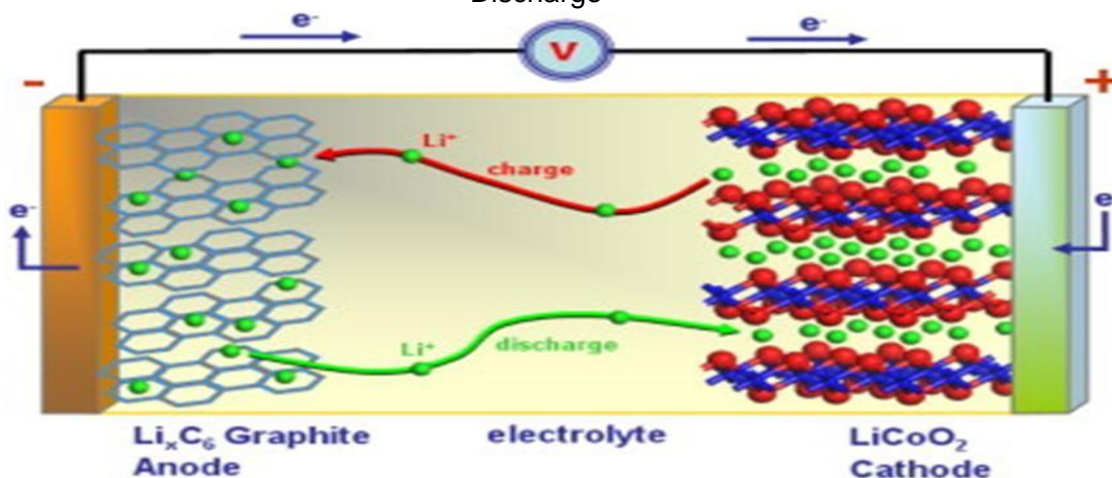
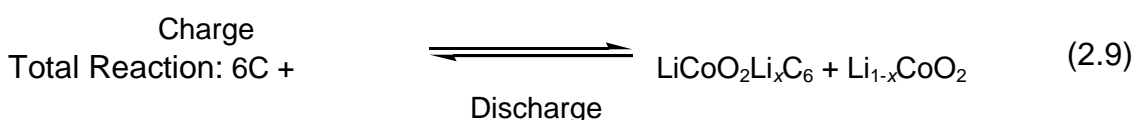
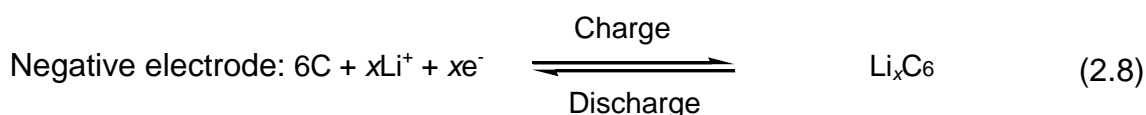
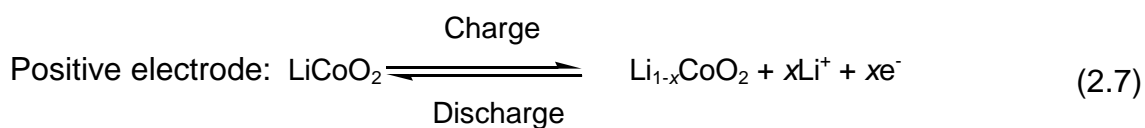


Figure 2.2 Processes occurring during charge and discharge of LIBs (Bruce *et al.*, 2008).

Since the introduction of the lithium-ion battery to the market by Sony in 1991, LIBs are one of the most promising energy storage devices and are widely implemented as the power or energy source in consumer applications (portable electronics) such as computers, notepads, video cameras, cell phones, and other devices (Figure 2.3). LIBs are also entering the hybrid electric vehicle market (Xu *et al.*, 2002; Zhang, 2015).

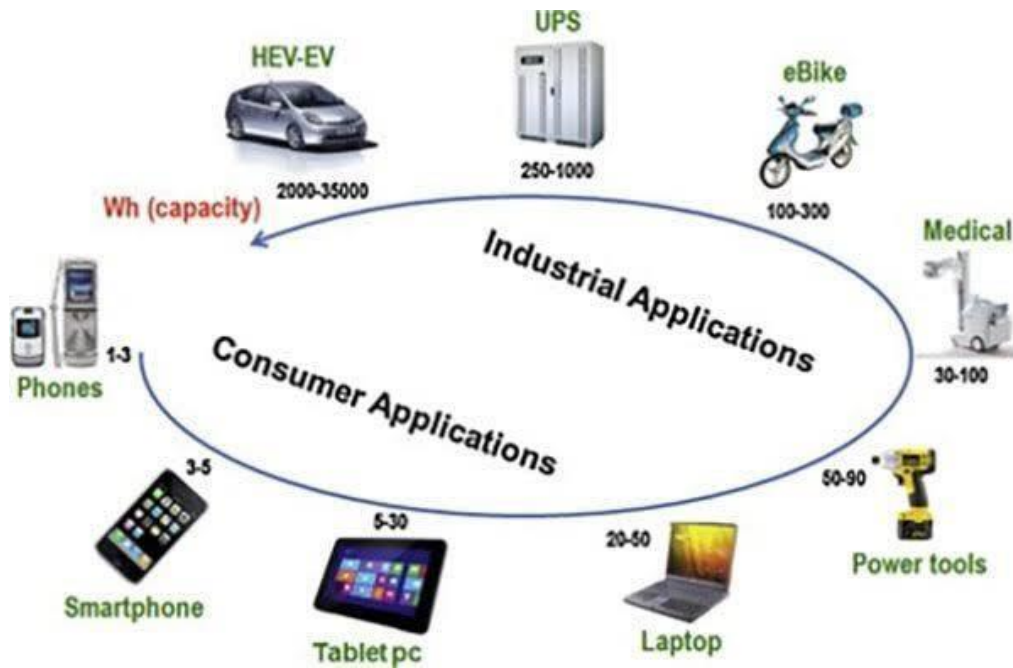


Figure 2.3 Applications of lithium-ion batteries (Yoo *et al.*, 2014).

2.2 The electrolyte in lithium-ion batteries

The electrolyte is one of the most important components of the battery as it acts as a transport system for the lithium ions during the charge and discharge processes. It also contributes to the power density, time stability, and safety of the battery since it is in close interaction with all the other components in the battery, including cathode, anode, and separator. An electrolyte can be regarded as an inert component of the battery since it interfaces (Figure 2.2) with both the negative and the positive electrode, so during the functioning of the battery, it must demonstrate stability against both the anode and the cathode surface. Generally, the electrolyte should have the following characteristics (Xu, 2004):

- It should be a good ionic conductor and electronic insulator, for the transport of lithium ions to be facile and self-discharge to be kept at a minimum.
- It should also be inert to other cell components.
- It should be thermally stable; for liquid electrolytes, both the melting and boiling points should be well outside the operating temperatures.

- It must have low toxicity and successfully meet also other measures of a limited environmental hazard.
- It must be based on sustainable chemistries, meaning that the elements are abundant, and the synthesis processes have as low as possible environmental impact and have a low total cost of materials and production.

Since the development of LIBs, there has been interest in many different types of electrolytes, including non-aqueous electrolytes, aqueous solutions, hybrid electrolytes, polymer electrolytes, including gel and solid polymers, and ionic liquids. Most of the electrolytes used in commercial LIB's are non-aqueous solutions containing a lithium salt such as LiClO_4 , LiFePO_4 , LiBF_4 , LiBC_4O_8 , or LiPF_6 . The salt is dissolved in a mixture of organic carbonates with high ionic and electronic conductivity, such as ethylene carbonate (EC), dimethyl carbonate (DMC), diethyl carbonate (DEC), ethyl methyl carbonate (EMC), and propylene carbonate (PC) (Balbuena and Wang, 2004).

The current status of electrolytes is that there are significant safety concerns for LIB's using LiPF_6 in organic carbonates as an electrolyte because at temperatures beyond 69°C thermal decompositions of electrolyte occurs, accompanied by heat evolution. Moreover, abusive conditions like overcharge, internal short-circuit or extrusion could also lead to exothermic reactions that will result in thermal runaway. Thermal runaway is the main cause of battery safety concerns (Doughty *et al.*, 2012; Bandhauer *et al.*, 2011; Wen *et al.*, 2012; Wang *et al.*, 2012). According to Liu *et al.* (2018), the thermal runaway process occurs in three stages (Figure 2.4):

Stage 1: Onset of overheating

Due to abnormal use of the battery or abuse conditions such as overcharging, faulty wiring resulting in external short circuits, cell defects caused by the formation of lithium dendrite under high current density charging (overcharging), cell fracture caused by car accidents, or improper battery assembly resulting in internal short circuits; these issues result in the battery overheating.

Stage 2: Heat build-up and gas release process

As the temperature rises above 90°C, battery components such as the separator melt results in the cathode and anode getting into contact, which then decomposes lithium oxides of the cathode material and results in the release of oxygen, which catalyzes other reactions, causing a further increase in temperature and pressure (“thermal runaway”). On the other hand, the solid-electrolyte interphase (SEI) layer formed during the first charge cycle decomposes, releasing flammable gaseous products such as ethylene. The SEI will be discussed in detail later in this chapter.

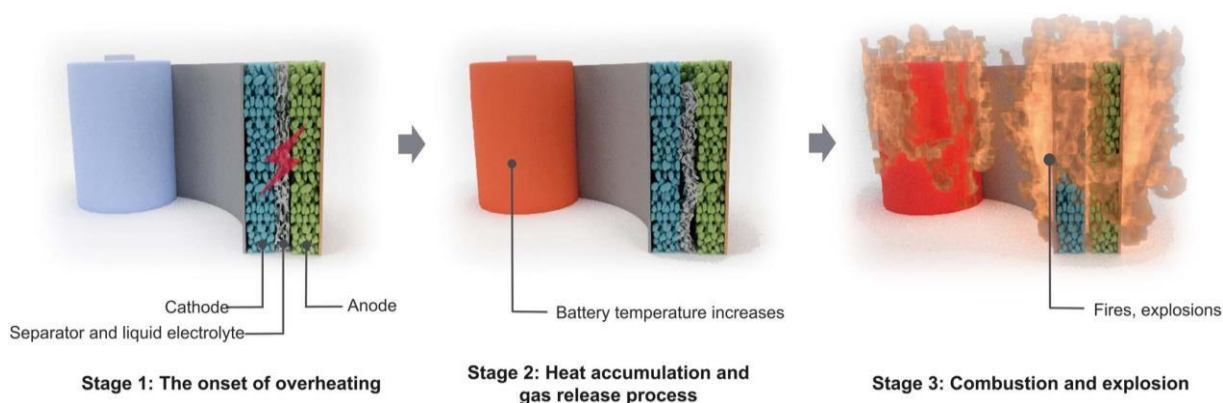


Figure 2.4 Schematic of thermal runaway stages of lithium-ion batteries (Liu *et al.*, 2018).

Step 3: Combustion and explosion

The accumulation of oxygen and an increase in pressure from step 2 cause the combustion of flammable gaseous products which eventually results in an explosion. Therefore, there is a need for electrolyte additives that will enhance and improve the performance of the battery, as discussed later, by acting as redox shuttle, flame retardant, and facilitating the formation of an SEI on the surface of the graphite anode. Often, additives are used as cathode protecting agents, LiPF_6 salt stabilizer, Lideposition improver, wetting agent, and corrosion inhibitor (Zhang, 2006), but there is still more to be done.

2.3 Negative electrode materials

The negative electrode plays a crucial role in the LIB as the characteristics of the anode directly influence the battery's electrochemical performance. Since the development of LIBs, there are many anode materials that have been investigated,

such as carbon, alloys, transition metal oxides, and silicon. The battery behaviour may depend on the inherent properties of the anode material, which include physical/chemical properties, energy storage capacity, crystallinity or amorphous structure of anode material, and most importantly the structural architectural arrangement during the charge/discharge process (Qi *et al.*, 2017).

Today most of the commercially used negative electrode materials are carbon-based materials; these materials are used due to their properties of larger crystallite structure, very high surface area, and an open porous structure, which allows more rapid access of lithium ions to the outer surface layers (Yang *et al.*, 1998) (Figure 2.5(a)). However, there are some shortcomings, such as the low working potential of carbon and the continuous deposition of lithium ions, which leads to the formation of tree-like structures called dendrites. As dendrites continue to grow, they cause internal shortcircuits between anode and cathode. In most reported safety-related incidents, these structures are the source of the safety issues - one of the biggest challenges for the prospect of carbon-based anodes in large-scale applications (Aurbach *et al.*, 1997; Aurbach *et al.*, 1999; Sun *et al.*, 2011). $\text{Li}_4\text{Ti}_5\text{O}_{12}$ with a spinel structure is a well-recognized insertion type anode material with good reversibility and small volume changes during the insertion process (Kim *et al.*, 2010; Ohzuku *et al.*, 1995; Wang *et al.*, 2007) (Figure 2.5(b)). However, the relatively high Li insertion potential (~ 1.5 V) and low reversible capacity ($\sim 150 \text{ mAh g}^{-1}$) neutralize its benefits (Chen *et al.*, 2012). Electrochemically alloying materials can form a compound phase with Li; for example, silicon has a high theoretical capacity (3590 mAh g^{-1}), ten times higher than that of carbonaceous material (372 mAh g^{-1}), and has a low voltage profile. However, during lithiation/delithiation there is a challenge with volume change (up to $\sim 300\%$) of the crystal structure (Figure 2.5(c)), which results in the SEI protective layer of the negative electrode being destroyed, and low intrinsic conductivity (Wang *et al.*, 2014).

Most recently, vanadium compounds have been investigated as anode material due to the oxidation state that can vary from V^{5+} to V^{2+} , which makes it an excellent candidate with higher theoretical capacity than many other transition metal-based compounds, and is expected to support higher Li insertion (Liang *et al.*, 2015). The vanadium compounds V_6O_{13} (West *et al.*, 1985), LiV_3O_8 (Pistoia *et al.*, 1985), FeVO_4

(Denis *et al.*, 1997), VO_2 (Mishra *et al.*, 2004), ZnV_2O_4 (Xiao *et al.*, 2009), V_2O_5 (Song *et al.*, 2010), $\text{Li}_{1+x}\text{VO}_2$ (Song *et al.*, 2010), $x\text{LiV}_3\text{O}_8 \cdot y\text{Li}_{0.3}\text{V}_2\text{O}_5$ (Qiao *et al.*, 2011), and LiVO_3 (Pralong *et al.*, 2012) are recent examples.

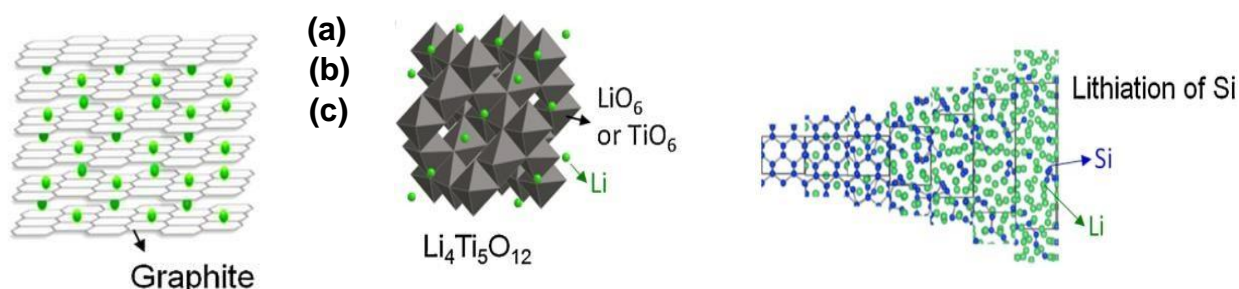


Figure 2.5 Crystal structures of (a) lithiated graphite (Yamada *et al.*, 2014); (b) lithium titanate (LTO) (Teshima *et al.*, 2011); and (c) silicon during lithiation (Chan *et al.*, 2012).

Li_3VO_4 and its derivatives have been reported as potential intercalation/deintercalation anode materials with a safe voltage plateau and relatively high specific capacity (Kim *et al.*, 2010; Ni *et al.*, 2014). Compared to other anode materials for LIB's, Li_3VO_4 not only has negligible volume changes but also possesses a suitable lithium-inserting potential (0.5 V–0.8 V vs. Li^+/Li); this is lower than those of $\text{Li}_4\text{Ti}_5\text{O}_{12}$ and TiNb_2O_7 , which may result in a higher energy density for a Li-ion full cell, since (Li *et al.*, 2015):

$$\text{Energy Density } E = (\Delta V \times C) / (1 + m_c), \quad (2.10)$$

Where ΔV = the operating voltage of the full cell,

C = the capacity of the negative electrode material, and

m_c = the matching mass of the positive electrode material.

The lithium insertion potential is higher than that of graphite, which may avoid the safety issue of short-circuiting associated with the formation of Li dendrites. Moreover, the high ionic conductivity of LVO ($\approx 10^{-6} \text{ S cm}^{-1}$) (Fu *et al.*, 2014) may ensure the rapid diffusion of Li^+ in the crystal structure, leading to good rate performance. With the reversible insertion of two Li-ions, the theoretical capacity ($\sim 394 \text{ mAh g}^{-1}$) of Li_3VO_4 is higher than that of graphite ($\sim 372 \text{ mAh g}^{-1}$) (Li *et al.*, 2014; Liang *et al.*, 2015), with only 4% volume expansion. Its structure, which

consists of corner-shared VO_4 and LiO_4 tetrahedra forming hollow lantern-like three-dimensional structures (Figure 2.6), provides empty sites and intercalation channels for Li^+ (Liang *et al.*, 2015). Thus, Li_3VO_4 is a promising alternative anode material for LIB's. However, there are still some restrictions for Li_3VO_4 to be resolved, because Li_3VO_4 , with its wide bandgap (3.9 eV), has a low intrinsic electronic conductivity and low initial coulombic efficiency, which leads to a large polarization impedance and poor rate performance (Zhao *et al.*, 2018), limiting its large-scale commercial application. The main reasons behind the low initial coulombic efficiency are the exposure of the surface of the material to the electrolyte, which results in the formation of a thick amorphous SEI layer on the surface, and the structural stress (irreversible degradation of the Li_3VO_4 structure) observed by the cracking of the micronized LVO particles due to insertion of Li^+ during the discharge/charge processes (Liu *et al.*, 2015; Liao *et al.*, 2016).

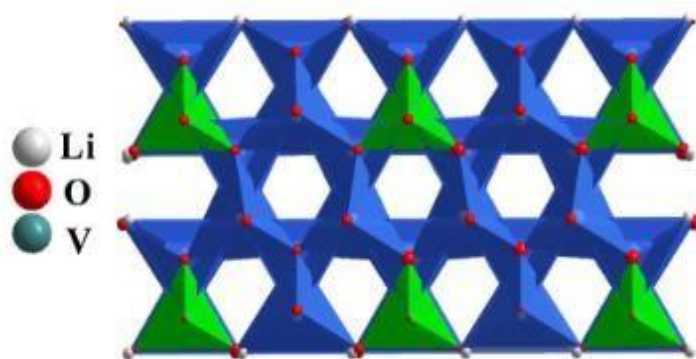


Figure 2.6 Crystal structure of orthorhombic Li_3VO_4 (Zeng *et al.*, 2017).

Many researchers have attempted to resolve the Li_3VO_4 disadvantages of poor rate performance (electrical conductivity and initial coulombic efficiency). Initial coulombic efficiency can be improved by 20% (from 61.6% to 79.5%) (Liao *et al.*, 2016) by relaxing the structural stress of LVO when fully coated with a carbon layer ($\text{Li}_3\text{VO}_4/\text{C}$) (Liang *et al.*, 2015). Alternatively, coating with reduced graphene oxide ($\text{Li}_3\text{VO}_4/\text{C/rGO}$) on mesoporous $\text{Li}_3\text{VO}_4/\text{C}$ composite increases the first coulombic efficiency from 81.9% to 94% (Shi *et al.*, 2013).

Reduction of particle size of the electrode material also improves the electrochemical performance, since the small particle-sized electrode material will shorten the diffusion path length of lithium ions during intercalation/deintercalation and provide a

greater surface area for lithium-ion flux (Zhang *et al.*, 2013; Zhang *et al.*, 2015; Jiang *et al.*, 2016). Many attempts have been made to reduce the particle size of the Li_3VO_4 using different synthesis methods, though it has been difficult to maintain the nanosized particles due to size growth when annealing at high temperature, leading to aggregation (Liao *et al.*, 2016). For example, solid-state reaction resulted in irregular particles of 0.5–2 μm (Li *et al.*, 2013); sol-gel synthesis produced sub-micrometer particles with sizes of 0.1–1 μm (Du *et al.*, 2015); hydrothermal synthesis resulted in mean particle size of 250 nm (Ni *et al.*, 2014); oil-bath synthesis gave a controllable particle size of 1.2 μm to 400 nm (Li *et al.*, 2015); ultrasonic spray pyrolysis resulted in sphere-like particles with sizes of 0.2–2 μm (Kim *et al.*, 2014); and the freeze-drying method gave nanoparticles with diameters of 25–35 nm (Zhao *et al.*, 2015).

Doping has been found to be one of the most effective methods to improve the electrochemical performance of most electrode materials. It is a low-cost feasible approach, with transition metal doping mostly by Fe, Cu, Ni, Cr, Co, and Ti improving the battery performance. For example, partial substitution of Mn in the spinel LiMn_2O_4 with Cr^{3+} (Chen *et al.*, 2010; Feng *et al.*, 2010) or Fe^{3+} (Peng *et al.*, 2010; Xu *et al.*, 2011) improved the stability of the structure, improved the electrochemical performance and weakened the Jahn-Teller effect (Wu *et al.*, 2015). A vanadium-based electrode material such as $\beta\text{-V}_2\text{O}_5$ when doped with Ni resulted in increased lithium-ion intercalation and deintercalation with good specific capacity. Li_3VO_4 , when doped with Cu^{2+} (Wang *et al.*, 2018), resulted in lattice extension improving the electronic conductivity; and Mg (Dong *et al.*, 2016), Mo (Dong *et al.*, 2017), and Ni (Zhang *et al.*, 2016) improved cycling stability and specific capacity.

2.4 Positive electrode materials

As shown in Figures 2.2 and 2.5, the cathode acts as a host network that stores guest lithium ions, which are later removed, reversibly. The positive electrode can be made of different compounds in different structures; these can be perovskite, spinel, layered, or olivine. Good cathode materials should have good structural stability to prevent structural changes during the charge and discharge processes; they should

have a high capacity, high electronic conductivity, have a low lithium diffusion barrier, and low lithium chemical potential. The early studies of cathode materials were based on metal chalcogenides (NbSe_3 and TiS_3). LiTiS_2 (LTS) has been widely studied due to its high gravimetric energy and long cycle life (1000+ cycles) but during lithiation, TiS_3 exhibited only partial reversibility due to irreversible structure change from a trigonal prismatic to an octahedral structure (Murphy and Trumbore, 1976). However, today high-potential oxide cathode materials with high storage capacities are studied.

The layered materials are the most successful and widely used cathode materials, even today, from the first LIB that was commercialized by Sony in 1991. They have relatively high specific capacities, good cycling performance, high volumetric capacity, low self-discharge, and high discharge voltages. LiCoO_2 is the most attractive cathode material, but it is very expensive because of the high cost of cobalt. When overcharged, this cathode material is less stable, and it can fail and undergo degradation resulting from the exothermic release of oxygen and other gases, because of its low thermal stability. This thermal runaway can result in explosion of an appliance so that a more stable alternative is needed.

Alternatives such as LiNiO_2 and LiMn_2O_4 spinel have been studied. Nickel and manganese are much cheaper than cobalt and these materials can be used as alternatives for LiCoO_2 . LiNiO_2 has a higher energy density than LiCoO_2 , similar specific capacity, and the same crystal structure as LiCoO_2 . However, LiNiO_2 is thermally less stable than LiCoO_2 because Ni^{3+} is more readily reduced than Co^{3+} (Arai *et al.*, 1998). During synthesis and delithiation of LiNiO_2 , the Ni^{2+} ions have the tendency of blocking lithium diffusion pathways by substituting Li^+ sites (Rougier *et al.*, 1996). As a result, partial replacement of Ni by Co can also result in good cathode materials ($\text{LiNi}_{1-x}\text{Co}_x\text{O}_2$) that will have a less cationic disorder. The addition of Al can improve electrochemical performance and thermal stability, resulting in a new low-cost cathode material, $\text{LiNi}_{0.8}\text{Co}_{0.15}\text{Al}_{0.05}\text{O}_2$ (NCA), which has a high charge-discharge capacity (200 mAh/g) and a long storage life compared to Co-based cathodes; however, at elevated temperatures, the capacity fades due to micro-crack formation and solid electrolyte interface (SEI) growth (Bloom *et al.*, 2003; Itou and

Ukyo, 2005), which will be discussed later in this chapter. Addition of Mn to $\text{LiNi}_{1-x}\text{Co}_x\text{O}_2$ to form a compound such as $\text{Li}(\text{Ni}_{1/3}\text{Mn}_{1/3}\text{Co}_{1/3})\text{O}_2$ results in a high capacity material with good rate capability (Wang *et al.*, 2009).

Manganese can form a layered structure with lithium, resulting in LiMnO_2 (LMO) and LiMn_2O_4 cathodes. Manganese oxides are much cheaper and less toxic than Ni and Co oxides. LMO was prepared two decades ago (Armstrong and Bruce, 1996) but its cycle life was still not satisfactory due to the many different oxidation states of manganese. For example, Mn^{3+} ion undergoes a disproportionation reaction to form Mn^{2+} and Mn^{4+} , which are soluble in the electrolyte, which then destabilizes the anode SEI and results in a change from a layered structure to spinel during cycling. To improve the performance of LMO, cationic doping was proposed (Ceder and Mishra, 1999), but this resulted in poor cycle stability. Today researchers are trying to improve the performance of LMO, more recently by the synthesis of novel cathode materials such as $\text{Li}_2\text{Mn}_2\text{O}_4$, spinel LiMn_2O_4 , and monoclinic LiV_3O_8 , since vanadium has several valences and layered vanadium oxides such as orthorhombic V_2O_5 are formed.

2.5 The solid-electrolyte interphase

In LIBs, the most widely used electrolyte is a lithium salt dissolved in an organic carbonate mixture. During the cycling process, the electrolyte undergoes oxidation at the positive electrode at high potential and reduction at the carbon negative electrode, resulting in the formation of some gaseous by-products and a thin layer of about 30 to 50 nm consisting of inorganic and organic decomposition products; this passive layer is known as the solid-electrolyte interphase (SEI) (Huang *et al.*, 2011). In perfect cases, this passive layer inhibits further electrolyte reduction by hindering electron transport through it and allows lithium ions to pass through it during cycling. However, this may reduce the initial performance of the cell and results in the long-term capacity fade, also known as an irreversible capacity loss (ICL) (An *et al.*, 2016). According to many studies of the SEI-like layer on the cathode surface, it does not have much impact on the battery performance. Therefore, the focus is on the SEI formed on the surface of the negative electrode.

The formation of the SEI is important for a battery's electrochemical performance, but if it is unstable and continues to form over the battery's lifetime, it can result in the consumption of lithium ions from the cathode, which will affect the energy density, while consumption of the electrolyte increases the cell resistance and lowers the liquid phase mass transport, which decreases the power density (Goodenough *et al.*, 2013 and Xu *et al.*, 2004). There have been many attempts to characterize the SEI, but they have produced debatable results since the composition of this layer does not stay constant throughout the cycling. The composition changes with temperature and potential, where at the lower potential it is found to be thicker than at higher potential (Xu *et al.*, 2004), and as cycling continues some of its components dissolve in the electrolyte (Zheng *et al.*, 1999); this makes it a complicated issue.

An extensive study of the SEI layer using spectroscopic techniques has shown that the composition of the SEI layer is highly dependent on the electrolyte composition and carbon material, but electrolyte decomposition products such as Li_2CO_3 , LiOH , LiF , Li_2O , ROCO_2Li , and RCO_2Li (Figure 2.7) were generally found (Verma *et al.*, 2010). Zhang *et al* found that the formation of the SEI layer is based mainly on the reduction of cyclic carbonates and proposed two competing reduction mechanisms for ethylene carbonate, thought to be due to its high polarity and dielectric constant (Okamoto, 2003).

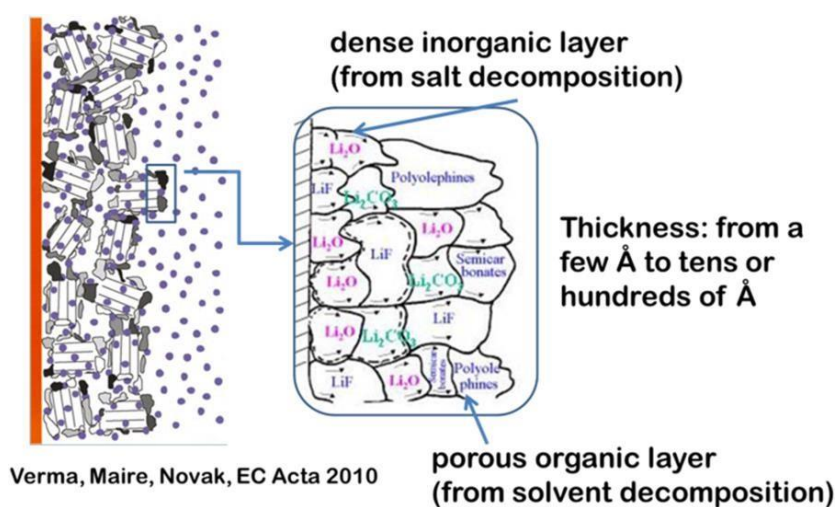
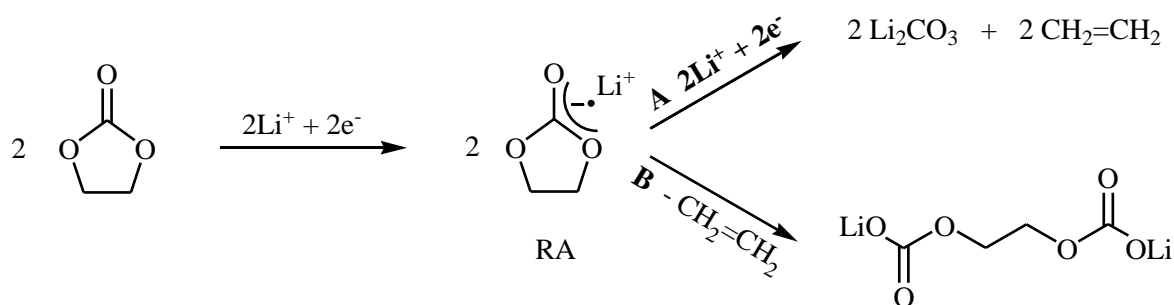
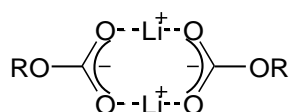


Figure 2.7 Schematic drawing of the solid-electrolyte interface (SEI) (Verma *et al.*, 2010).

SEI layer formation starts with a ring-opening reaction of the ethylene carbonate influenced by reaction with inorganic electrolyte salts such as LiPF_6 where the anion (PF_6^-) acts as a catalyst for the reaction (Okamoto, 2013; Henschel *et al.*, 2019; Lee *et al.*, 2000). According to Zhang's accepted mechanism and an EIS study of the formation of SEI, it occurs over two voltage ranges. In the first stage (mechanism A), before intercalation of lithium ions into the graphite, the solvent is reduced to form gaseous products (such as ethylene), causing a layer that is structurally porous, highly resistive, dimensionally unstable, and rich in Li_2CO_3 . The second stage (mechanism B) results in the formation of fewer gaseous products with the formation of a more compact, stable, and highly conductive SEI (Scheme 2.1). The stability in the second stage is brought by coordination of lithium ion to a cyclic carbonate ion, which is adsorbed on the carbon surface and reduces the strain in the ring structure, lowering the activation energy for the reaction (Scheme 2.2) (Collins *et al.*, 2015; Balbuena *et al.*, 2001; Wang *et al.*, 2001; Matsuta *et al.*, 2000).



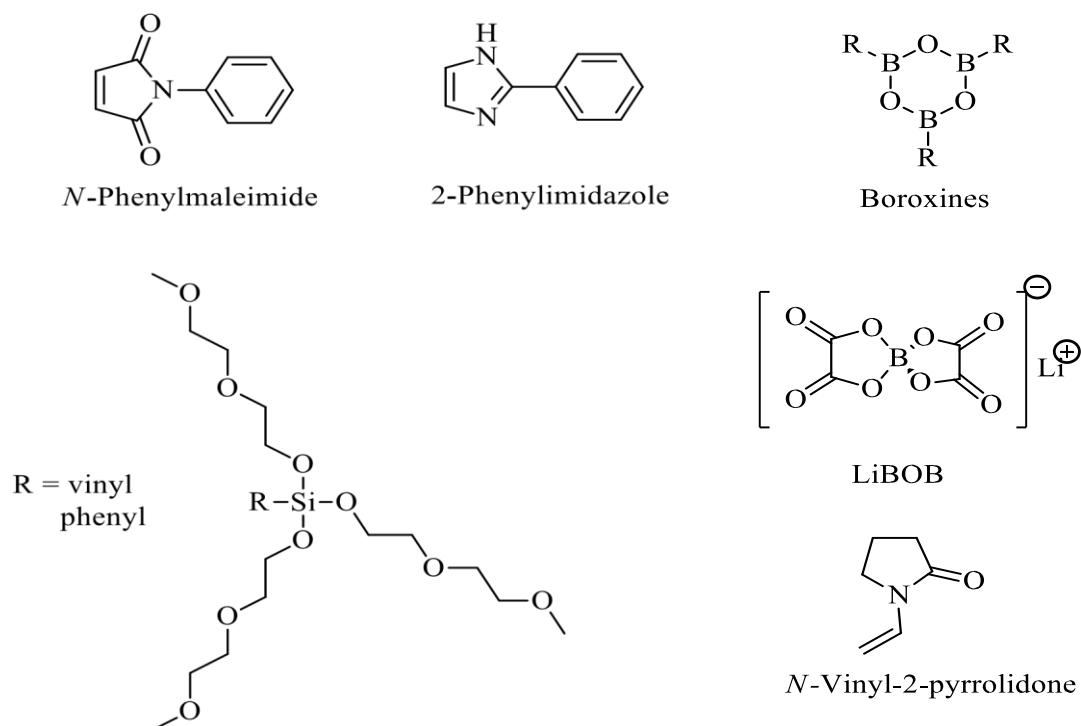
Scheme 2.1 The two competing mechanisms for the formation of SEI in carbonate solvents (Zhang, 2006).



Scheme 2.2 Coordination of lithium ions with organic carbonate ions.

The studies by Yang *et al.* (1998) show that the formation of a stable, continuous, and permissive SEI layer on the anode is a crucial aspect of the first charge event because such layer (Mai *et al.*, 2009) protects the electrode against exfoliation and permits the ion conduction needed for lithium-ion insertion and extraction (Jeong *et al.*, 2011). The SEI is also a cushion to electron flow and limits further decomposition of electrolytes (Agubra and Fergus, 2013).

The formation of a stable SEI layer and reduction of gas generation in the first intercalation of lithium ions can be facilitated by modification of the surface of the graphite electrode, such as mild chemical oxidation (Wu *et al.*, 2002) or by coating the graphite anode with a permeable polymer film, or using reduction type electrolyte additives (e.g., Scheme 2.3). These types of additives have a higher reduction potential than the electrolyte solvent so that the additives are ideally reduced or electropolymerized on the surface of the graphite and deactivate the catalytic activity. Hence, utilization of these additives not only secures the graphite surface by electropolymerization but also decreases gas generation and increases the stability of the SEI because of the cooperation of additive molecular moieties into the SEI (Zhang, 2006).



Scheme 2.3 Examples of electropolymerisable additives.

At most, approximately 5% by volume or weight of the additive is used, which significantly improves the cyclability and cycle life of LIBs (Zhang, 2006). The study conducted by Bebede and van Ree (2015) also shows that boronic acids and boronate esters are good electrolyte additives. For example, 3,5-bis(trifluoromethyl)phenylboronic acid is reduced at higher potential because its lowest unoccupied molecular orbital (LUMO) energy level is significantly lower than

that of the commonly used carbonate solvents. This greatly suppresses the decomposition of organic carbonates and exfoliation of the graphite anode, which allows Li^+ ions to reversibly intercalate/deintercalate from the graphite into the electrolyte (Wang *et al.*, 2008). It is therefore not surprising that, according to quantum chemical calculations, phenylboronic acid can be expected to form a stable dimer with ethylene carbonate (Ramaite and van Ree, 2017). This observation will be tested and exploited in the current project.

Many additives have been developed, such as vinylene carbonate (VC), which is extensively used in carbonate-based electrolytes. The VC additive firstly undergoes an intermediate reduction reaction and forms a stable ion-pair, which then undergoes ring-opening by homolysis of the carbonate solvent (Campion *et al.*, 2004; Li *et al.*, 2005). The stable ion-pair is terminated to form unsaturated complexes of lithium vinylene carbonate $(\text{CHOCO}_2\text{Li})_2$ and lithium divinylene dicarbonate $(\text{CH}_2=\text{CHOCO}_2\text{Li})_2$ (Balbuena and Wang, 2004). The active film-forming products consist of polymerization products of VC, which are deposited on the electrode (Agubra and Fergus, 2013). This results in an SEI layer that enhances lithium-ion transport at the electrode/electrolyte interface (Joho and Novák, 2000). The VC effectively deactivates the graphite anode surface active sites to avoid carbonate solvent co-intercalation (Wang *et al.*, 2002; Vetter *et al.*, 2005) and direct solvent decomposition on the graphite. The VC additive also significantly reduces the amount of propylene, hydrogen, ethylene, and other gases formed on the cathode from the decomposition of carbonate solvent (Buqa *et al.*, 2006). The effectiveness of VC as an additive is due to its higher negative reduction potential vs Li^+/Li relative to the supporting solvents such as EC, PC, and DMC (Agubra and Fergus, 2013).

2.6 Battery charge-discharge cycling

The battery performance in terms of charge-discharge rate is the speed at which current can be put into and taken from storage. Charge-discharge characteristics of the battery are measurements of voltage under constant charge and discharge current input, in terms of ampere-hour efficiency or voltage or watt-hour efficiency; ampere-hour efficiency indicates how much-stored electricity is used during discharge. Charge/discharge measures are controlled by current or voltage, as it is

measured either at constant current (CC) or constant voltage (CV). For example, in Figure 2.8 the voltage is brought up to CV level by initially applying CC charge. The battery is charged/discharged (cycled) at a constant low current (C/20) several times for the first time after being assembled to form the SEI layer on the surface of the electrode and prevent internal shorting, allowing a stable flow of lithium ions.

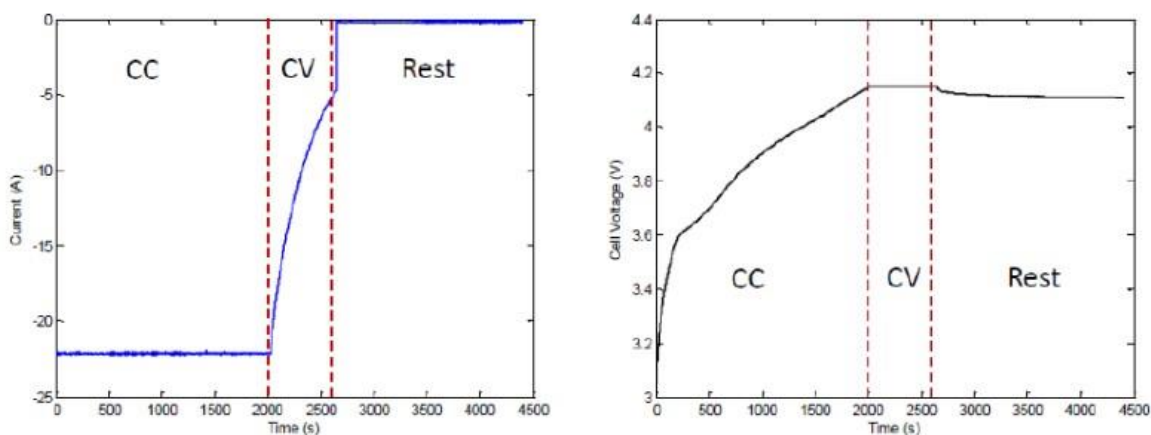


Figure 2.8 Typical examples of CC-CV charging curves of a lithium-ion battery (Wang *et al.*, 2018).

There are several electrochemical techniques that are most useful in studying battery performance, such as electrochemical impedance spectroscopy (EIS), galvanostatic charge-discharge (GCD), and cyclic voltammetry (CV). Cyclic voltammetry is a potential technique that studies the redox behavior of a compound and probes coupled chemical reactions. To perform cyclic voltammetry the terminal voltages (E_1 and E_2), scan rate (v) are first determined (Figure 2.9(a)) and then applied to the electrochemical system which is going to be tested (Brett *et al.*, 1993). The current response i of the reaction of interest in the working electrode is measured against the reference electrode over a specified voltage range at a fixed scan rate. A typical voltammogram for an electrochemical system consisting of a reversible single electron transfer reaction is shown in Figure 2.9(b); the voltage is swept from E_1 to the switching potential E_2 to cause oxidation at a fixed scan rate, resulting in the anodic current (i_{pa}) at the corresponding potential E_{pa} (where E_{pa} is the potential reached when all the substrate in the surface of the electrode has been oxidized). After the switching potential has been reached the voltage is swept backward to E_1 and the current flows in the opposite direction, resulting in the cathodic current (i_{pc}),

with the cathodic peak potential E_{pc} being reached when all the substrate at the surface of the electrode has been reduced.

Galvanostatic charge-discharge (GCD) cycling is an electrochemical technique that measures the voltage response of electrode material to an applied current; this technique is used to investigate rate capability, reversibility, and capacity of electrode material. In this technique, the potential of the reaction of interest in the working electrode is measured as a function of time against the reference electrode. As in cyclic voltammetry, to conduct GCD measurements, the terminal voltage is determined first in the direction of the inverted current (Figure 2.10(a)).

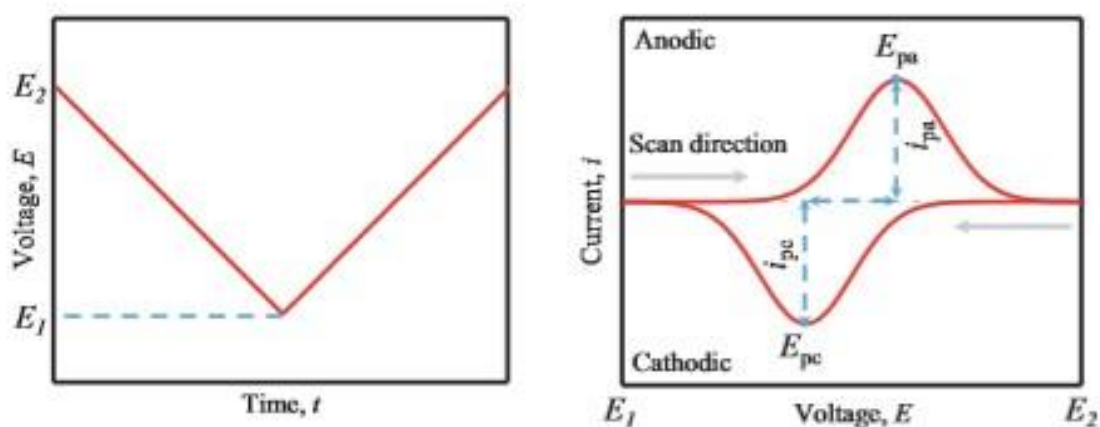


Figure 2.9 (a) Voltage profile applied in a cyclic voltammetry measurement; (b) current response versus voltage curve (Yang and Rogach., 2019).

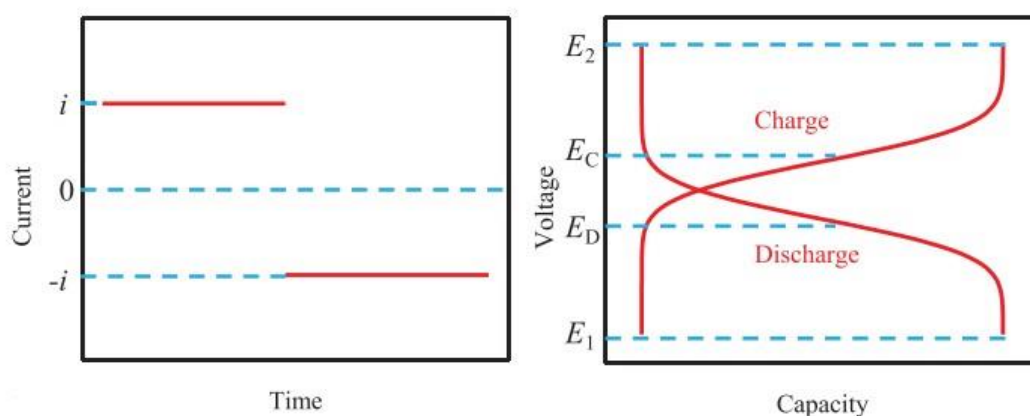


Figure 2.10 (a) Applied current profile; (b) typically recorded voltage response versus capacity curves (Yang and Rogach., 2019).

Electrochemical impedance spectroscopy (EIS) is a non-destructive alternating current (AC) spectroscopy technique that measures the ratio of applied sinusoidal

voltage with low amplitude to the current response over a frequency range (e.g. 10^{-2} Hz to 10^5 Hz) (Bard *et al.*, 1980). In this method, the electrochemical cell is represented as an electrical circuit as shown in Figure 2.11(a), where:

L = inductance,

R_i = ohmic resistance,

Z_{ZARC} = depressed semicircle in the complex plane,

Z_w = Warburg impedance, and

C_{dl} and R_{ct} represent a non-linear RC circuit (Buller, 2003; Karden, 2001)

Figure 2.11(b) shows a typical electrochemical impedance spectrum with three frequency regions (low frequency, high frequency, and medium frequency). All these frequency regions describe the battery dynamic characteristics, and we can study different processes. For example, in the high-frequency region ($f > 79$ Hz), we can study the movement of charges carried through the electrolyte and the battery's ohmic resistance. Whereas in the medium frequency region ($79 \text{ Hz} < f < 1.76 \text{ Hz}$), we can study the electrochemical double layers formed at the electrolyte/electrode interface. The charge transfer resistance R_{ct} ($R_{ct} = R_d - R_0$) (Jiang *et al.*, 2017) resulting from the electrode surface where the charge is transferred; and in the low-frequency region ($f < 1.76 \text{ Hz}$), the effect of Li-ion diffusion inside the electrode material is seen (Barsoukov *et al.*, 2000).

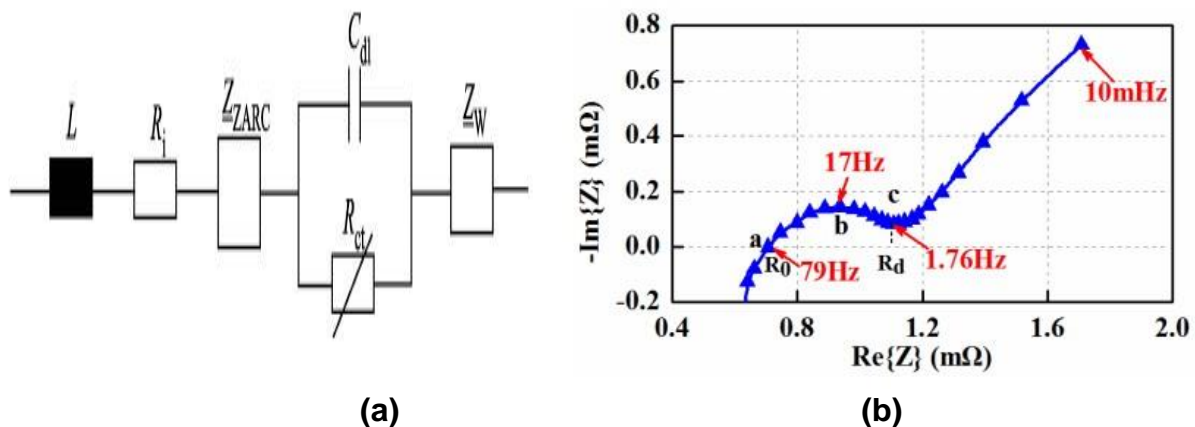


Figure 2.11 (a) Electrical circuit model of the Li-ion battery (Buller *et al.*, 2005); and (b) typical EIS of a cell at 25°C and 50% state of charge (SOC) (Jiang *et al.*, 2017).

2.7 Protecting electrode materials against decay and overcharge

Electrode decay is one of the problems encountered because of the decomposition of the electrolyte (Figure 2.2), which increases the electrode resistance and at the same time decreases the electrode's capability to reversibly accommodate Li-ions and reduces the electrode's storage capacity (Zavalis *et al.*, 2013; Amine *et al.*, 2005), causing voltage decrease (Safari and Delacourt, 2011; Smith *et al.*, 2011). According to the study conducted by Li *et al.* (2016), electrode decay is associated with structural deterioration and can be limited by the formation of a stable SEI with a compact inner layer.

Overcharge occurs when the battery is being charged beyond the designed voltage (Zhang, 2006; Chen *et al.*, 2009), initially resulting in overheating of the battery, as seen in Figure 2.2. Overcharging causes a series of problems that result in LIBs being currently unpopular, but necessary, battery technology for application in hybrid electric vehicles (HEVs). A large body of research has established that the overcharging problem can be resolved by the use of overcharge protection additives, classified as shutdown additives that permanently terminate battery operation and redox shuttle additives that reversibly protect the battery from overcharging (Zhang *et al.*, 2012; Haregewoin *et al.*, 2016; Xu *et al.*, 2004; Xu, 2014).

Overcharge protection additives should at least have a suitable redox potential, good solubility, a large diffusion coefficient, and excellent reversibility. On the overcharged positive electrode surface (Figure 2.12), the required shuttle molecule (S) should undergo reversible oxidation to its radical cation ($S^{\cdot+}$) at a higher potential than the normal end-of-charge potential of the positive electrode, and then diffuse via the electrolyte to the negative electrode, where it undergoes reversible reduction at a lower potential than the normal end-of-charge potential of the negative electrode, returning to its original state (S) (Wang *et al.*, 2008b; Thomas *et al.*, 1996).

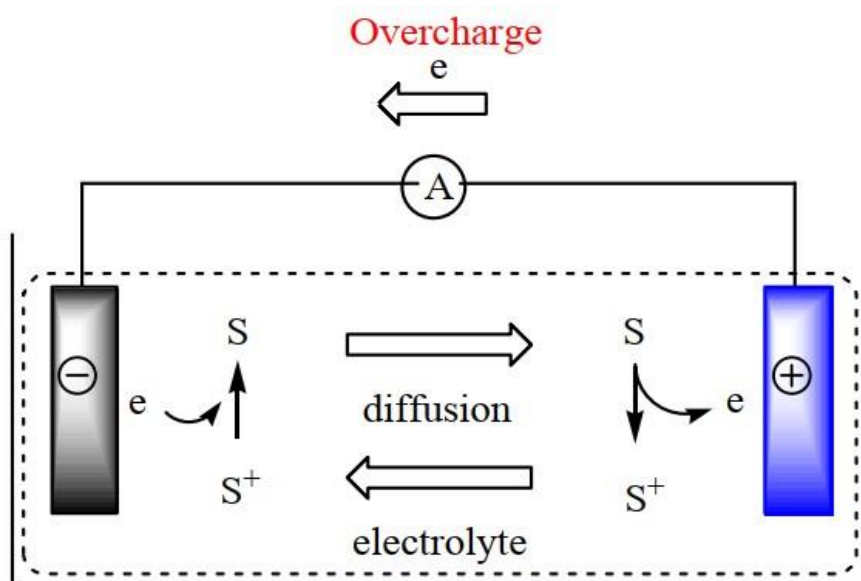


Figure 2.12 Overcharge protection mechanism by a redox shuttle molecule S (Zhang *et al.*, 2011).

A study conducted by Chen *et al.* (2010) found that inorganic electrolyte salts such as the lithium boronate cluster salt $\text{Li}_2\text{B}_{12}\text{H}_{12-x}\text{F}_x$ (where $x = 9$ and 12) can serve as a redox shuttle additive; the degree of fluorination adjusts the redox potential of this molecule and the boron center, which is a strong Lewis acid, acts as anion receptor in breaking down LiF produced during the operation of the lithium-ion battery. Boron can attain several oxidation states and therefore boronates can be used as electrolyte shuttle components (Bebeda and van Ree 2015; Hu *et al.*, 2014; Zhang *et al.*, 2012; Wang *et al.*, 2008).

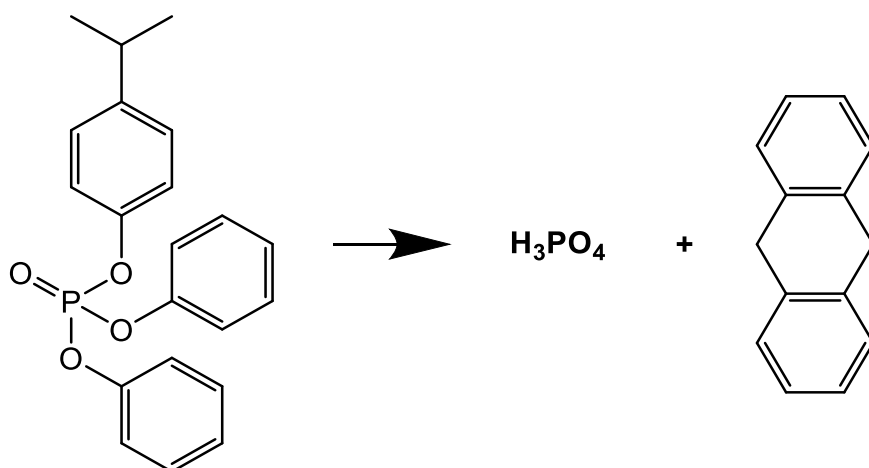
Electrochemical polymerization additives such as biphenyl (Matadi *et al.*, 2017), cyclohexylbenzene (Lee *et al.*, 2006), or xylene (Zhang *et al.*, 2009) can be used as overcharge protection additives since they polymerize on the surfaces of the electrodes or separator and result in the formation of polymer dendrites. Polymer dendrites penetrate the separator forming a conductive bridge between the two electrodes and result in an internal micro-short circuit to lower the voltage (Wang *et al.*, 2019). Feng *et al.* (2013) synthesized tri-(4-methoxyphenyl) phosphate, which was used as an electrolyte additive that polymerizes at 4.35 V and was also found to reduce the flammability of the electrolyte due to the presence of the phosphate group (organic phosphorus additive).

Because of their good thermal stability, high efficiency, low volatility (Levchik and Weil, 2006), and most notably, their ability to function in the vapor phase (Wang et al., 2005) to activate the formation of hydrogen radicals ($H\cdot$) that react with oxygen to create oxygen free radicals ($O\cdot$), suppressing combustion of the electrolyte additive solvent containing alkyl carbonate after being added, organic phosphorus additives that are non-halogen containing are widely studied (Baginska *et al.*, 2018; Wang *et al.*, 2005; Dixon *et al.*, 2004).

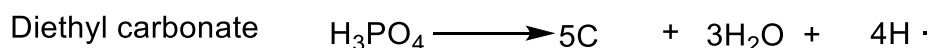
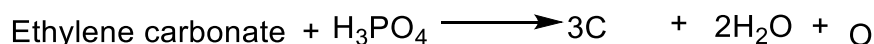
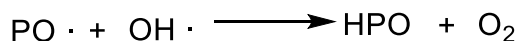
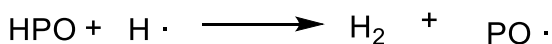
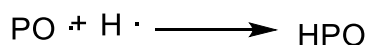
The propagation of the radical reaction must be stopped in order to prevent the combustion of the electrolyte solvent. The organophosphorus flame retardants are strong radical scavengers since they decompose at high temperatures to create H_3PO_4 (Equation 2.11). The H_3PO_4 then transforms into HPO_2 , $PO\cdot$, and $PO_2\cdot$ will absorb $H\cdot$ and $O\cdot$, while HPO_2 will stimulate the carbonation reaction of carbonate (Equation 2.12) (Jin *et al.*, 2013; Wang *et al.*, 2019; Xiang *et al.*, 2007). For example, 4-isopropyl phenyl diphenyl phosphate (IPPP) when about 10%, 15%, and 20% are used as an electrolyte additive in an electrolyte containing EC: DEC (1:1 wt%) increases the onset temperature from 140 °C (no IPPP) to 170, 175 and 184 °C, this strongly propose that using IPPP in the electrolyte greatly slows the initiation of decomposition and increases the electrolyte's thermal stability.

Decomposition of electrolyte additive

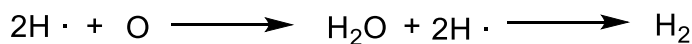
(2.11)



Production of Radicals in a gas phase (2.12)



Char formation (2.13)



1-Diphenylphosphoryloxy-4-methylbenzene (Yan *et al.*, 2021), tris(2,2,2-trifluoroethyl) phosphite (Pires *et al.*, 2015), tris(pentafluorophenyl) phosphine (Xu *et al.*, 2014), dimethyl methylphosphonate (Xiang *et al.*, 2007), and triphenyl phosphate (Ciosek Högström *et al.*, 2014) have been used as phosphorus flame-retardant additives and were found to be effective in terms of their retardant properties which improves the battery safety. However, the most significant disadvantage of using phosphate flame retardants as electrolyte additives comprises electrochemical efficiency, due to their reduction and cointercalation of the graphite anode.

Therefore it is important to find phosphorus flame-retardant additives that will have effective retardant properties and also improve the electrochemical performance of the battery without reduction on the graphite anode. In this study, we are linking known electrolyte additives together to make a bifunctional additive such as 2-((2,2-dimethyl-3,6,9,12-tetraoxa-2-silatetradecan-14-yl)oxy)-1,3-dihydrobenzo[d][1,3,2]-diazaphosphole 2-oxide (**DTSDP**) which contains an *ortho*-phenylenediamine group, which was found to electropolymerize on the graphite anode (Bottari *et al.*, 2020). (Diethylene glycol methyl-(3-dimethyl(trimethylsiloxy)silyl propyl)ether) polyether siloxanes, investigated by Inose *et al.* (2006), improved the electrolyte thermal stability and had good cycle performance.

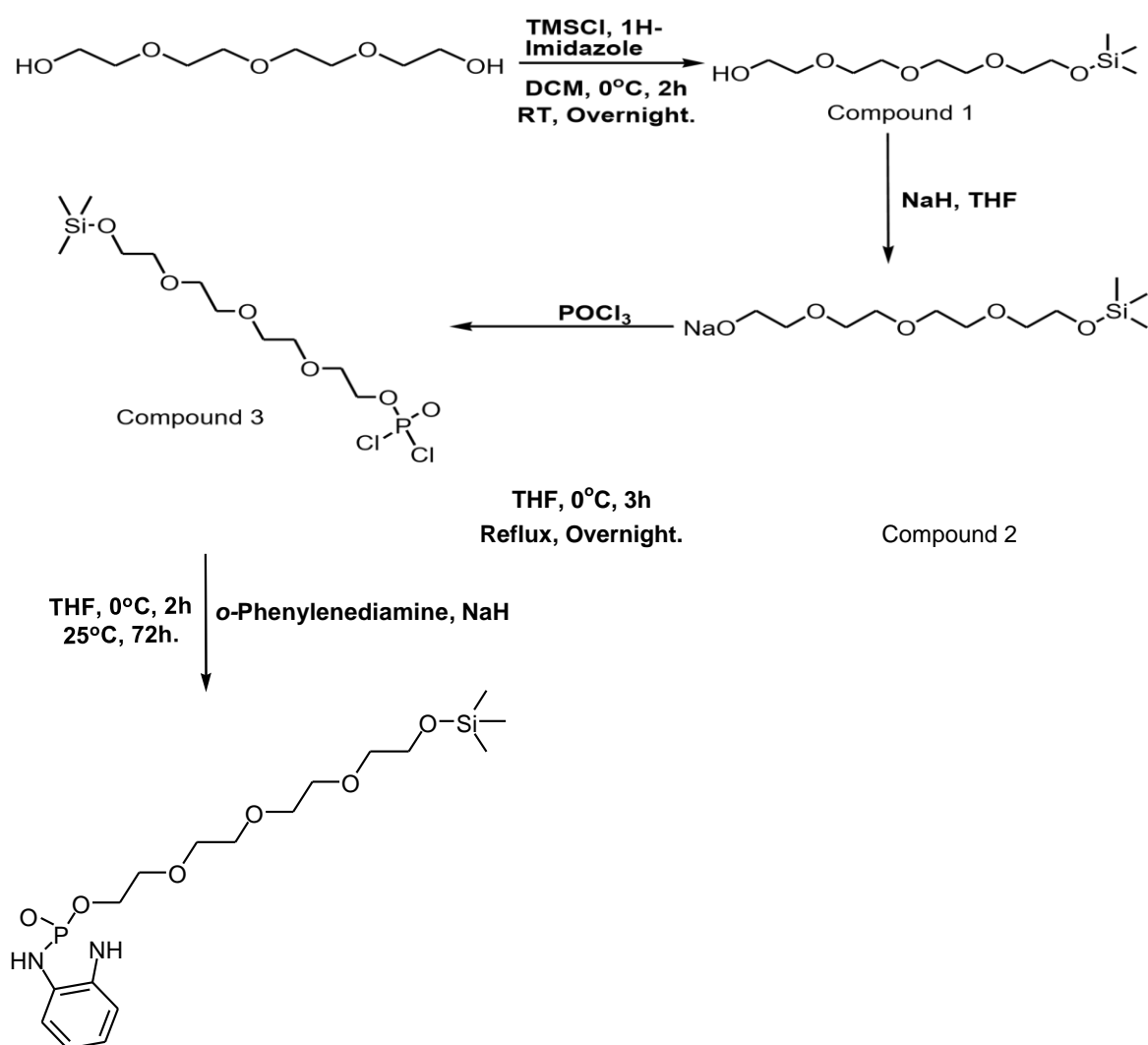
3. Experimental

3.1 General Experimental Conditions

All reagents and solvents were Reagent Grade and purchased from Sigma-Aldrich. Solid reagents were used without purification and solvents were distilled and dried before use. A Büchi rotatory evaporator was used to evaporate the solutions, and a Scientific muffle oven was used for the temperature-programmed calcination of samples.

3.2 Synthesis of organic electrolyte additives

3.2.1 Synthesis of 2-((2,2-dimethyl-3,6,9,12-tetraoxa-2-silatetradecan-14yl)oxy)-1,3-dihydrobenzo[d][1,3,2]diazaphosphole 2-oxide.

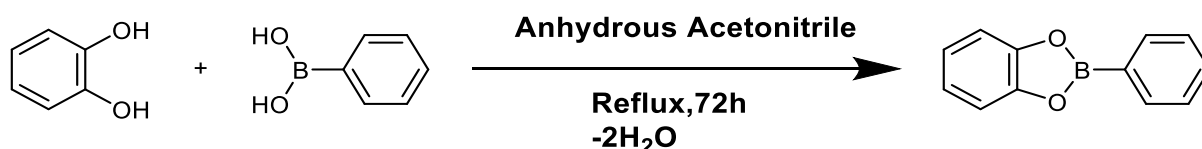


An oven-dried three-necked round-bottomed flask equipped with a magnetic stirrer bar, thermometer, and CaCl_2 drying tube was charged with 102.68 mmol (2.464 g) NaH in 10 ml anhydrous THF under an argon atmosphere. Compound **1** was obtained according to the method reported by Das *et al.* (2018). Tetraethyleneglycol (32 mmol) in 10 ml anhydrous THF was added dropwise at 0°C over 0.5 h, releasing H_2 gas. The reaction proceeded for 1.5 hours at room temperature; the colourless solution turned light yellow. The reaction was then cooled down to 0°C , then 32.09 mmol (4.92 g) POCl_3 was added drop-wise over a period of 3 h, resulting in a heterogeneous mixture with NaCl residue and Compound **2**. The resulting mixture was then refluxed overnight. *Ortho*-phenylenediamine (32 mmol) in 20 ml anhydrous THF was added dropwise to the mixture containing Compound **2** over a period of 2 h at 0°C , increasing to room temperature after 2 h, and the reaction ran for 72 h, monitored by TLC till the starting material was consumed. The NaCl residue was filtered off, and the filtrate was concentrated by rotary evaporation, followed by extraction with 15 ml dilute HCl and chloroform to remove the unreacted *o*-phenylenediamine dihydrochloride, resulting in orange viscous oil that was then further purified by silica gel column chromatography using chloroform: methanol (95%:5%) to give a pink viscous oil (8.72g, yield 64.9%).

^1H NMR (400 MHz, Methanol- d_4) δ_{H} 6.71 (2H, t, $J = 2.5$ Hz), 6.68 – 6.63 (2H, m), 4.40 (2H, s), 4.17 (2H, t, $J = 4.7$ Hz), 3.86 (2H, t, $J = 4.6$ Hz), 3.68 (2H, dd, $J = 5.8$, 3.7 Hz), 3.57 – 3.53 (8H, m), 3.45 (2H, d, $J = 5.1$ Hz), 0.22 (9H, s) ppm (Appendix A).

^{13}C NMR (100 MHz, Methanol- d_4) δ_{C} 133.91, 119.46, 109.07, 71.56, 70.49, 70.20, 70.00, 69.45, 67.71, 3.54 ppm (Appendix A).

3.2.2 2-Phenylbenzo[d][1,3,2]dioxaborole



An oven-dried two-necked round-bottomed flask (100 ml) equipped with a magnetic stirrer bar and CaCl_2 drying tube was charged with a mixture of 12.3 mmol (1.5 g) phenylboronic acid and 12.3 mmol (1.35 g) 1,2-dihydroxybenzene in 20 ml anhydrous acetonitrile under an argon atmosphere. The resulting solution was then

refluxed for 72 h and the reaction was monitored by TLC till the starting material was consumed. The resulting solution was then concentrated by rotary evaporation, resulting in an orange viscous oil which was then further purified by column chromatography on silica gel using chloroform: methanol (95:5) to yield a white crude product (8.72 g, yield 64.9%).

^1H NMR (400 MHz, CDCl_3) δ_{H} 7.95 – 7.89 (2H, m), 7.65 (3H, m), 7.51 (2H, t, $J = 7.4$ Hz), 7.32 – 7.27 (2H, m) ppm (Appendix B).

^{13}C NMR (100 MHz, CDCl_3) δ_{C} 148.21, 133.43, 132.73, 128.77, 122.97, 122.22 ppm (Appendix B).

3.3 Synthesis of new electrode materials

3.3.1 Synthesis of Li_3VO_4 using the sol-gel method

Anhydrous lithium nitrate (LiNO_3 , 93 mmol) and 14.95 mmol vanadium pentoxide (V_2O_5) were dissolved completely in de-ionized water along with an appropriate quantity of starch or chitosan as fuel. The resulting orange homogeneous mixture was then stirred for 1 h using a magnetic stirrer at 90°C . The resultant blue gel solution was then evaporated at 110°C for 12 hours to get precursor in the form of a foam, which was then ground. The precursor was then calcined by heating at a rate of $2^\circ\text{C}/\text{minute}$ at 700°C for 5 h to obtain Li_3VO_4 .

3.3.2 Synthesis of doped $\text{Li}_3\text{V}_{1-x}\text{M}_x\text{O}_4$ using the sol-gel method

Similarly, $\text{Li}_3\text{V}_{1-x}\text{M}_x\text{O}_4$ was synthesized by adding an appropriate amount of V_2O_5 ($1-x$ moles of V_2O_5) to 93 mmol of anhydrous lithium nitrate (LiNO_3) with starch or chitosan as fuels; the orange resulting solution was then heated at 80°C for 1 h. The resulting blue solution (as above) shows that LVO was then formed, and it was then cooled to room temperature and the appropriate amount x of M salt (dopant) was added. The resulting solution was then heated at 90°C for 1.5 h. The resulting gel was then evaporated at 110°C for 12 hours to get precursor in the form of a foam which was then ground and calcined by heating at a rate of $2^\circ\text{C}/\text{minute}$ at 700°C for 5 h to obtain $\text{Li}_3\text{V}_{1-x}\text{M}_x\text{O}_4$ particles. The dopant salts used were $\text{Cr}(\text{NO}_3)_3 \cdot 9\text{H}_2\text{O}$, basic zinc carbonate ($2\text{ZnCO}_3 \cdot 3\text{Zn}(\text{OH})_2$), MgOH , AgNO_3 , and $(\text{NH}_4)_2\text{Ce}(\text{NO}_3)_6$.

3.4 Characterization of electrode materials and electrolyte additives

The synthesized materials were characterized by thermogravimetric analysis (TGA), X-ray diffraction (XRD), scanning electron microscopy (SEM), electron dispersive X-ray spectroscopy (EDX), and the synthesized electrolyte additive was characterized by nuclear magnetic resonance spectroscopy (NMR).

For thermogravimetric analysis (TGA) the sample (8 mg) was heated in a Perkin Elmer TGA4000 at a heating rate of 10°C/min, airflow rate 20 ml/min (at 2.9–3 bar), nitrogen flow rate 20 ml/min (at 2.8–3 bar), and temperature range: 35–900°C.

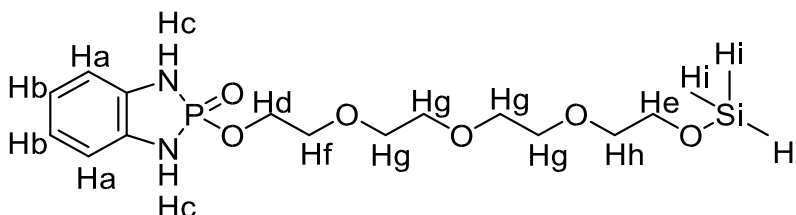
Powder X-ray diffraction (PXRD) is an analytical technique used to determine and identify the phase(s) and structure type of crystalline materials. The Rietveld refinement of the PXRD data provides information about the lattice parameters, d-spacing, and crystal density. A PANalytical X'Pert Pro diffractometer with CuK α radiation ($\lambda = 1.5046 \text{ \AA}$, 45 kV, 40 mA, step size = 0.02°) was used. The XRD diffractograms were obtained in a scan range between 0 and 90°. The lattice parameters and crystal information were obtained by Rietveld refinement using Match XRD with Fullprof software (Rodriguez-Carjaval, 2001).

The scanning electron microscope (SEM) is a form of an electron microscope that images the sample by scanning it with a focused high-energy electron beam in a raster scan pattern. This technique can be used to determine the morphology, particle size, and shape of the sample particles. The prepared samples were examined using a field emission scanning electron microscope (FE-SEM) (JSM-7500F, JEOL) with an acceleration voltage of 2.00 kV. The samples were coated with carbon during sample preparation to prevent charging. Energy Dispersive X-ray Spectroscopy (EDX) was used for the elemental analysis of the sample. An SEM/EDX combined instrument was used for the analysis of the sample.

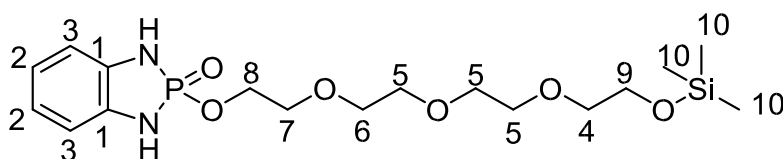
4. Results and Discussion

4.1 Electrolyte additives

4.1.1 2-((2,2-Dimethyl-3,6,9,12-tetraoxa-2-silatetradecan-14-yl)oxy)-1,3-dihydrobenzo[d][1,3,2]diazaphosphole 2-oxide



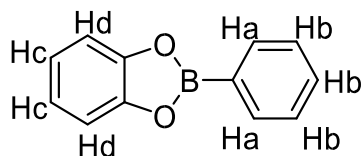
2-((2,2-Dimethyl-3,6,9,12-tetraoxa-2-silatetradecan-14-yl)oxy)-1,3-dihydrobenzo[d][1,3,2]diazaphosphole 2-oxide was obtained as viscous light pink oil, using POCl_3 , *o*-phenylenediamine, tetraethylene glycol and trimethylchlorosilane (TMSCl). The product structure was confirmed by the ^1H NMR and the ^{13}C NMR (Appendix A). As expected the ^1H NMR has nine signals, two in the aromatic region; a triplet (Ha) around 6.71 ppm for two equivalent protons, a multiplet (Hb) around 6.46 ppm for two equivalent protons. In the aliphatic region, there are eight peaks, a singlet (Hc) around 4.40 ppm for two equivalent (NH) protons, a triplet (Hd) around 4.17 ppm, a triplet (He) around 3.86 ppm, a triplet (Hf) around 3.68 ppm, a multiplet (Hg) around 3.5 ppm for eight equivalent protons, a triplet (Hh) around 3.44 ppm and a singlet (Hi) around 7.44 ppm for nine equivalent protons.



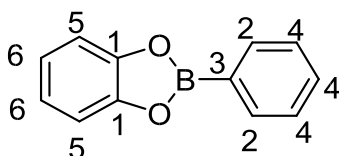
The ^{13}C NMR spectrum of the product has ten peaks as expected. One quaternary carbon at 133.91 ppm (C1) for two equivalent carbons, the peak at 119.46 ppm (C2) for two equivalent methines, 109.07 ppm (C3) for two equivalent methine carbon, 71.56 ppm (C4) for methylene carbon, 70.49 ppm (C5) for three equivalent methylene carbons, 70.20 ppm (C6) methylene carbon, 70.00 ppm (C7) for methylene carbon. Other signals are 69.45 ppm (C8) for methylene carbon, 67.71

ppm (C₉) for methylene carbon, and 3.54 ppm (C₉) for three equivalent methyl carbons.

4.1.2 2-Phenylbenzo[d][1,3,2]dioxaborole



2-Phenylbenzo[d][1,3,2]dioxaborole was obtained as an oil, by refluxing the mixture of phenylboronic acid and 1,2-dihydroxybenzene. The product structure was confirmed by the ¹H NMR and the ¹³C NMR spectra (Appendix B). 2-Phenylbenzo[d][1,3,2]dioxaborole has four peaks in the ¹H NMR aromatic region (7-8 ppm) with the disappearance of the OH (-2H₂O) peaks shows that the product was successfully formed, all the peaks were observed. Therein a multiplet (Ha) around 7.92 ppm for two equivalent protons, a triplet (Hb) around 7.65 ppm for three equivalent protons, a triplet (Hc) around 7.51 ppm for two equivalent protons, and a doublet of triplet (Hd) around 7.44 ppm for two equivalent protons.



The ¹³C NMR spectrum of the product has six peaks as expected, two quaternary carbon at 148.21 ppm (C₁) and 132.73 ppm (C₃), four equivalent methine carbons at 133.43 ppm (C₂), 128.77 ppm (C₄), 122.97 ppm (C₅) and 122.22 ppm (C₆).

4.2 Electrode Materials

4.2.1 Thermogravimetric Analysis

TGA was executed by the Department of Chemistry at Witwatersrand University. TGA of Li₃VO₄ (undoped and doped) prepared by starch-, citric acid-, and cellulose

mediated sol-gel synthesis (Fig. 4.1) confirmed that calcination should be done up to 700°C. All samples were calcined to 730°C as described in the Experimental section.

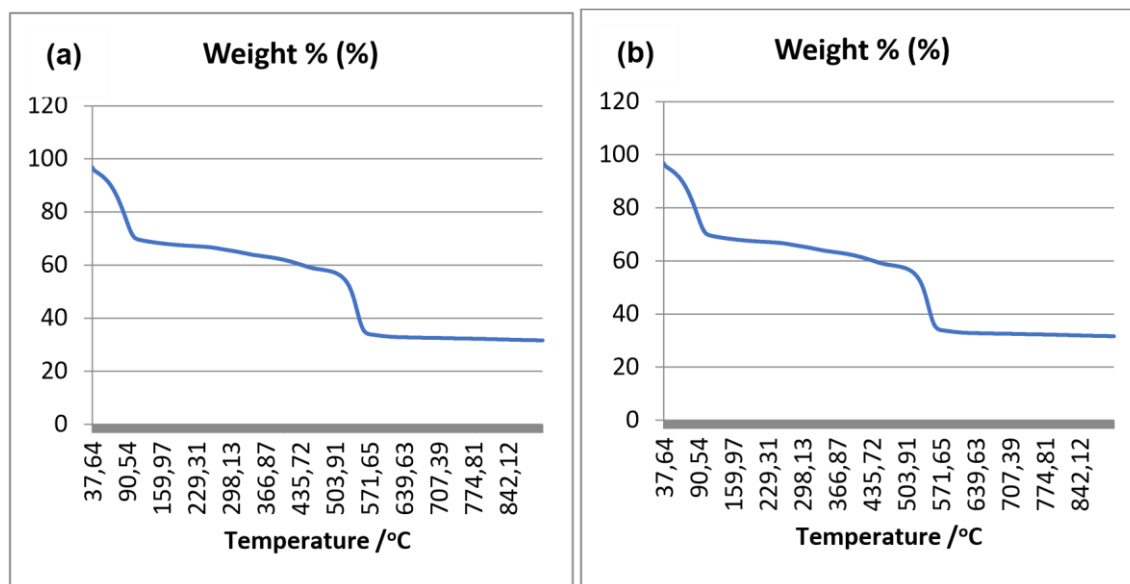


Figure 4.1 TGA of representative samples: (a) LVO with a starch template; (b) 1% Cu doped LVO on starch.

4.2.2 Silver Doped Lithium Vanadates, $\text{Li}_3\text{V}_{1-x}\text{Ag}_x\text{O}_4$

Figure 4.2(a) shows the XRD pattern of Li_3VO_4 and a series of Ag-doped Li_3VO_4 samples. The peaks in these patterns can be assigned to the low-temperature orthorhombic phase of Li_3VO_4 which belongs to the $Pmn21$ (31) space group (crystallography open database file number 1528868, entry number 96-152-8869). At low Ag content, there are only single-phase Li_3VO_4 indicating that Ag^+ successfully substituted V^{5+} to form $\text{Li}_3\text{V}_{1-x}\text{Ag}_x\text{O}_4$ (for $x < 0.1$). However, at high Ag content ($x \geq 0.1$) the presence of AgO is evident, due to the ionic radius of Ag^{2+} (0.94 Å) that is greater than that of V^{5+} (0.46 Å) (Zhao *et al.*, 2018). Figure 4.2(b) shows the expanded region between 30° and 31° (peak (111)), showing that the diffraction of the doped sample has shifted to a lower 2θ value compared to undoped Li_3VO_4 ($x = 0$); thus, Ag doping has enlarged the interlayer spacing.

To further understand the effect of Ag doping on the Li_3VO_4 crystal structure, Rietveld refinement of the XRD patterns was carried out using Match XRD with Fullprof software (Rodriguez-Carjaval, 2001); the single Li_3VO_4 phase with space group $Pmn21$ was selected as the initial refining structure (Table 4.1). Refined XRD patterns are shown in Figure 4.3(a-c) for the samples with $x = 0$, $x = 0.01$ and $x =$

0.5, it can be seen clearly that there are two different phases (two Bragg positions, one for Li_3VO_4 and one for AgO_2) as mentioned above at $x = 0.5$. Their crystal structures (Figure 4.4(a-b)) were drawn based on the refinement results. The Ag doping does not break the orthorhombic Li_3VO_4 crystal structure, remaining stable as shown in Figure 4.4(b). The lattice parameters are listed in Table 4.2 and show a slight lattice expansion as evidenced in the values of a , b , c , and volume V , caused by doping with Ag. Figure 4.4(b) shows that the doped Ag ions mainly occupy V sites. The tunnel structure of the corner-sharing adjacent LiO_4 and AgO_4 tetrahedra present in the doped samples causes an increase in the lattice parameters. It should be mentioned that the slight lattice expansion of Ag-doped Li_3VO_4 should be beneficial for the intercalation and deintercalation of lithium ions, leading to more rapid Li-ion diffusion. The crystallite size (D) was calculated using Scherrer's Eq. 4.1 (Iqbal *et al.*, 2007) from the broadening of the peaks.

$$D_{hkl} = k\lambda/(\beta\cos\theta) \quad (4-1)$$

Where D_{hkl} is the average diameter of the crystallite, k is 0.89, λ is the wavelength of monochromatic X-ray (for $\text{CuK}\alpha$ radiation, $\lambda = 0.15405$ nm), θ is the Bragg angle, and β the half-width of the diffraction peak (in radians). The approximate crystallite size of samples ranges from $24\text{-}34 \pm 0.01$ nm.

The SEM image (Figure 4.5(a)) of the as-prepared Li_3VO_4 polycrystalline powder shows agglomerated particles with particle size ranging from 200 nm to 100 nm, while the EDS mapping (Figure 4.6, Table 4.3) indicates the presence of V, O, and C. The presence of carbon is due to the use of carbon (conducting layer) as a coating agent for SEM analysis while Li cannot be detected since it has very low energy of characteristic radiation. Figure 4.5(b-d) shows the morphologies of the Ag-doped Li_3VO_4 series with $x = 0.01$, $x = 0.1$, $x = 0.5$, respectively, which are similar to that of undoped Li_3VO_4 . Figure 4.5(b) shows agglomerated particles to chunks with nonuniform particle size. However, Figure 4.5(c, d) shows more uniform particles with smaller particle sizes (average from 90 nm to 5 μm) compared to the particles of the undoped Li_3VO_4 (Figure 4.5(a)). It should be mentioned that the uniformity and particle size of the electrode material play an important role in improving the electrochemical performance of the battery (Zhao *et al.*, 2018; Zhao *et al.*, 2015).

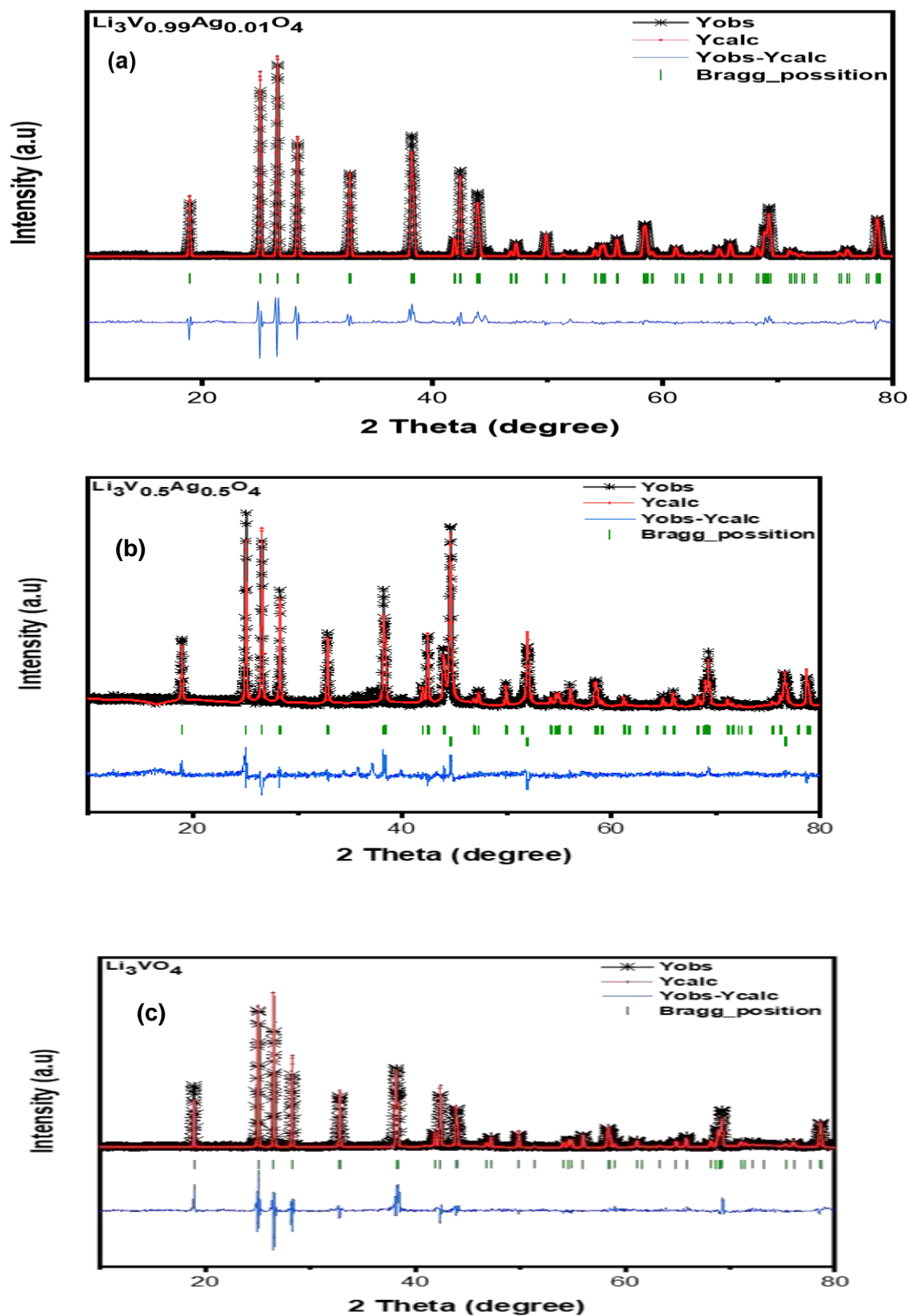


Figure 4.3 Typical results of Rietveld refinement: (a) $\text{Li}_3\text{V}_{0.99}\text{Ag}_{0.01}\text{O}_4$; (b) $\text{Li}_3\text{V}_{0.99}\text{Ag}_{0.01}\text{O}_4$; (c) $\text{Li}_3\text{V}_{0.99}\text{Ag}_{0.01}\text{O}_4$.

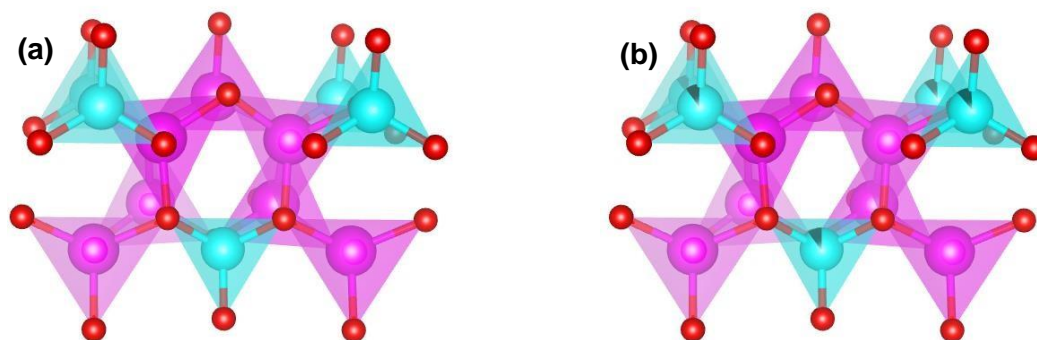


Figure 4.4 Crystal structures of $\text{Li}_3\text{V}_{(1-x)}\text{Ag}_x\text{O}_4$ samples for (a) $x = 0$ and (b) $x = 0.01$. Blue atoms = Vanadium, Purple atoms = Lithium, Red atoms = Oxygen and Black atom parts = Silver.

Table 4.1 The key structure parameters of $\text{Li}_3\text{V}_{0.99}\text{Ag}_{0.01}\text{O}_4$ ($x = 0.01$) obtained by Rietveld refinement.

Atom	Site	x	y	z
Li1	4b	0.24700	0.33150	0.98720
Li2	2a	0.50000	0.83260	0.98480
O1	4b	0.22390	0.68040	0.89100
O2	2a	0.00000	0.12960	0.89520
O3	2a	0.50000	0.17360	0.84780
V1	2a	0.00000	0.82961	0.00000
Ag1	2a	0.00000	0.82961	0.00000

Table 4.2 Calculated lattice parameters of $\text{Li}_3\text{V}_{(1-x)}\text{Ag}_x\text{O}_4$ samples, based on XRD data refinement.

Sample	a [Å]	b [Å]	c [Å]	V (Å ³)	Crystallite size (D) nm
x = 0.00	6.32184	5.44279	4.94440	170.488	32.00
x = 0.01	6.32792	5.44875	4.94909	170.542	25.46
x = 0.05	6.32920	5.44634	4.94872	170.580	34.00
x = 0.1	6.32833	5.44815	4.94817	170.673	24.88
x = 0.3	6.32989	5.44785	4.94729	170.704	28.26
x = 0.5	6.33063	5.44788	4.94778	170.825	26.05

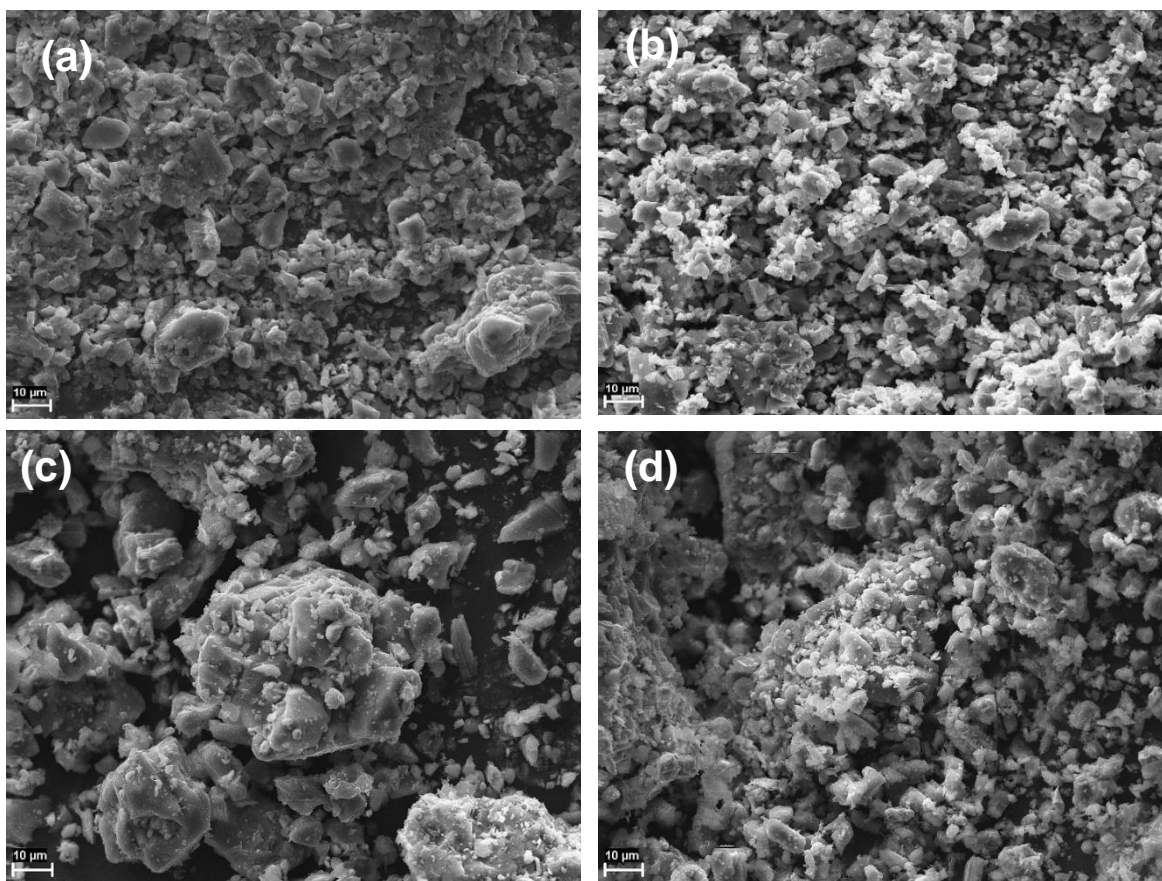


Figure 4.5 The SEM images of $\text{Li}_3\text{V}_{1-x}\text{Ag}_x\text{O}_4$ samples: (a) $x = 0$, (b) $x = 0.01$, (c) $x = 0.3$, (d) $x = 0.5$.

Table 4.3 Semi-quantitative energy dispersive X-ray microanalysis (wt.%) of the EDS for all the samples.

Sample x	O (wt.%)	V (wt.%)	Ag (wt.%)
0.00	33.5	66.5	
0.01	30.4	67.1	2.5
0.05	34.0	61.0	5.1
0.1	33.7	53.5	12.9
0.3	45.5	44.2	10.3
0.5	44.3	43.4	12.3

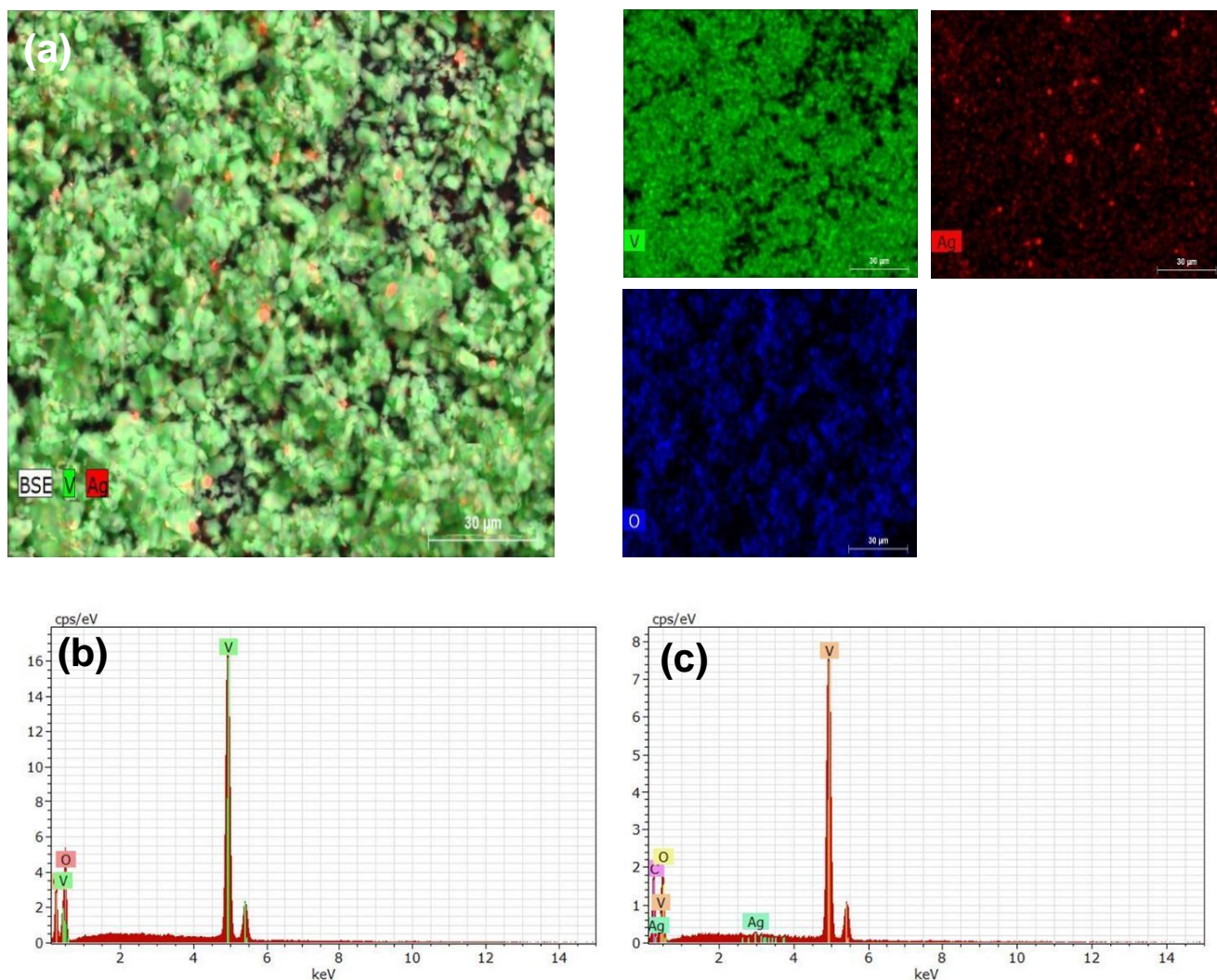


Figure 4.6 (a) EDS mappings of related elements for $\text{Li}_3\text{V}_{1-x}\text{Ag}_x\text{O}_4$ ($x = 0.01$); EDS spectra of (b) Li_3VO_4 and (c) $\text{Li}_3\text{V}_{0.99}\text{Ag}_{0.01}\text{O}_4$.

4.2.3 Cerium Doped Lithium Vanadates, $\text{Li}_3\text{V}_{1-x}\text{Ce}_x\text{O}_4$

Figure 4.7(a) shows the XRD pattern of Li_3VO_4 and a series of Ce-doped Li_3VO_4 samples. The peaks of the as-prepared can be assigned to the low-temperature orthorhombic phase of Li_3VO_4 which belongs to the $Pmn21$ (31) space group (crystallography open database file number 1528868 (entry number 96-152-8869)). At low Ce content ($x \leq 0.01$) there is only single-phase Li_3VO_4 indicating that Ce^{3+} successfully substitutes V^{5+} to form $\text{Li}_3\text{V}_{(1-x)}\text{Ce}_x\text{O}_4$ like Ce^{3+} doped $\text{Li}_4\text{Ti}_5\text{O}_{12}$ (Zhou *et al.*, 2015). However, when the x content is increased to $x > 0.01$ there appear secondary phase peaks of CeO_2 around 32° , 56° , and 66° (indicated by an asterisk). Figure 4.7(a) shows that as the concentration of the dopant increases for $x > 0.01$

the peaks of the main structure weakens; this means that some of the Ce^{3+} ions do not substitute V^{5+} ions, due to the ionic radius of 1.01 Å, which is greater than that of V^{5+} (0.355 Å). However, the successful incorporation of some Ce can be seen from Figure 4.7(b), (the expanded region between 30° and 38° (peak 111 and peak 200), clearly showing the shift of peak 111 and peak 200 to lower 2θ values compared to those of undoped Li_3VO_4 ($x = 0$); the peak shifting to a lower 2θ value indicates that some doping of Ce into Li_3VO_4 occurred and enlarged the interlayer spacing, which results in lattice expansion.

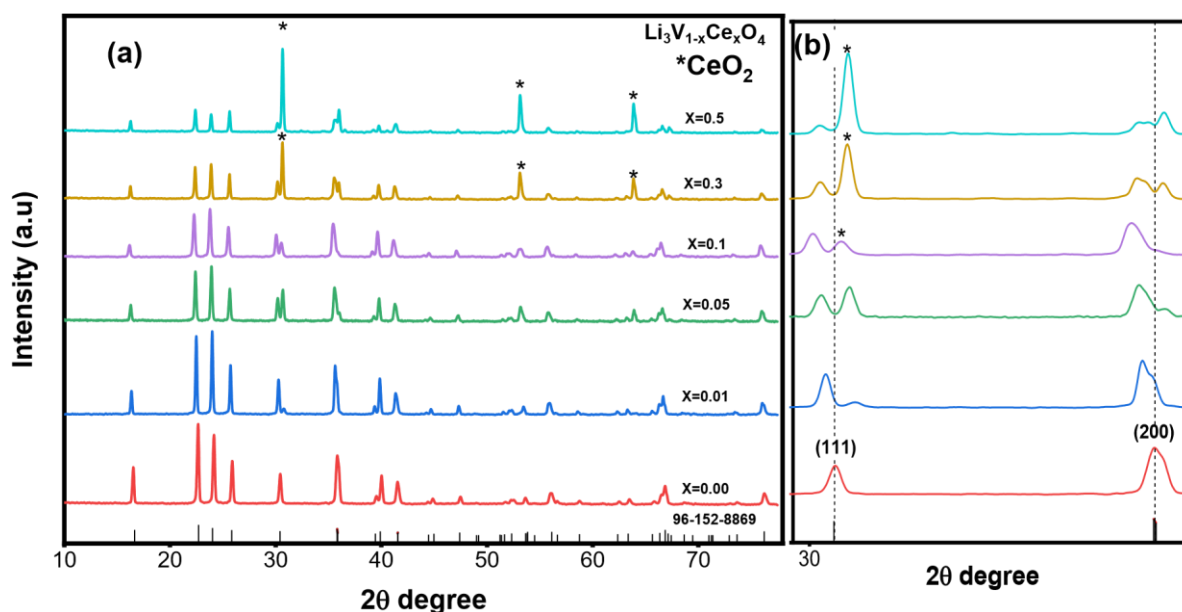


Figure 4.7 (a) XRD pattern of $\text{Li}_3\text{V}_{(1-x)}\text{Ce}_x\text{O}_4$ ($x = 0.0$, $x = 0.05$, $x = 0.1$, $x = 0.3$ and $x = 0.5$); (b) enlargement of the XRD pattern between 35° and 38° 2θ values.

To further understand the effect of Ce doping on the Li_3VO_4 crystal structure, Rietveld refinement of the XRD patterns (Table 4.4) was carried out using Match XRD with Fullprof software (Rodriguez-Carjaval, 2001); the single Li_3VO_4 phase with space group $Pmn21$ was selected as the initial refining structure. Refined XRD patterns are shown in Figure 4.8(a-c) for the samples with $x = 0$, $x = 0.01$, and $x = 0.5$, and their crystal structures (Figure 4.9(a,b)) were drawn based on the refinement results. Figure 4.9(a) clearly shows that at low content ($x \leq 0.01$), Ce^{3+} is incorporated into the orthorhombic Li_3VO_4 crystal structure, since there is a single-phase shown by the Bragg position and shown by the respective crystal structure (Figure 4.10(a)), However, at higher doping content (Figure 4.9(b)), there are two phases (two sets of

Bragg positions, Top- Li_3VO_4 and Bottom- CeO_2), because not all the Ce^{3+} can be incorporated into the orthorhombic Li_3VO_4 crystal structure, resulting in the two-phased crystal structure shown in Figure 4.9(c). The lattice parameters are summarized in Table 4.5, from the values of a , b , c , volume V there is a slight lattice expansion when $x \leq 0.01$, and when $x \geq 0.01$ there is a slight change as the concentration of dopant increase the values of the crystal parameters decreases, this might be due to larger binding energy of Ce^{3+} ions compared to that of V^{5+} which enters the structure to occupy V^{5+} ion in the tetrahedral V sites and weakens the main structure peaks due to decrease of the V^{5+} content as it can be observed in Figure 4.8(a-b). The tunnel structure of corner-sharing adjacent LiO_4 and CeO_4 tetrahedra present in the doped samples causes an increase in the lattice parameters. It should be mentioned that the slight lattice expansion of Ce doped Li_3VO_4 should be beneficial for the intercalation and deintercalation of lithium ions, leading to more rapid Li-ion diffusion. The crystallite size (D) was calculated using Scherrer's Eq. 4-1 (Iqbal et al., 2007) from the broadening of the peaks and the approximate crystallite size of samples ranges from 27- 38 ± 0.01 nm.

Table 4.4 The key structure parameters of $\text{Li}_3\text{V}_{0.99}\text{Ce}_{0.01}\text{O}_4$ ($x = 0.01$) obtained by Rietveld refinement.

Atom	Site	x	y	z
Li1	4b	0.24700	0.33150	0.98720
Li2	2a	0.50000	0.83260	0.98480
O1	4b	0.22390	0.68040	0.89100
O2	2a	0.00000	0.12960	0.89520
O3	2a	0.50000	0.17360	0.84780
V1	2a	0.00000	0.82961	0.00000
Ce1	2a	0.00000	0.82961	0.00000

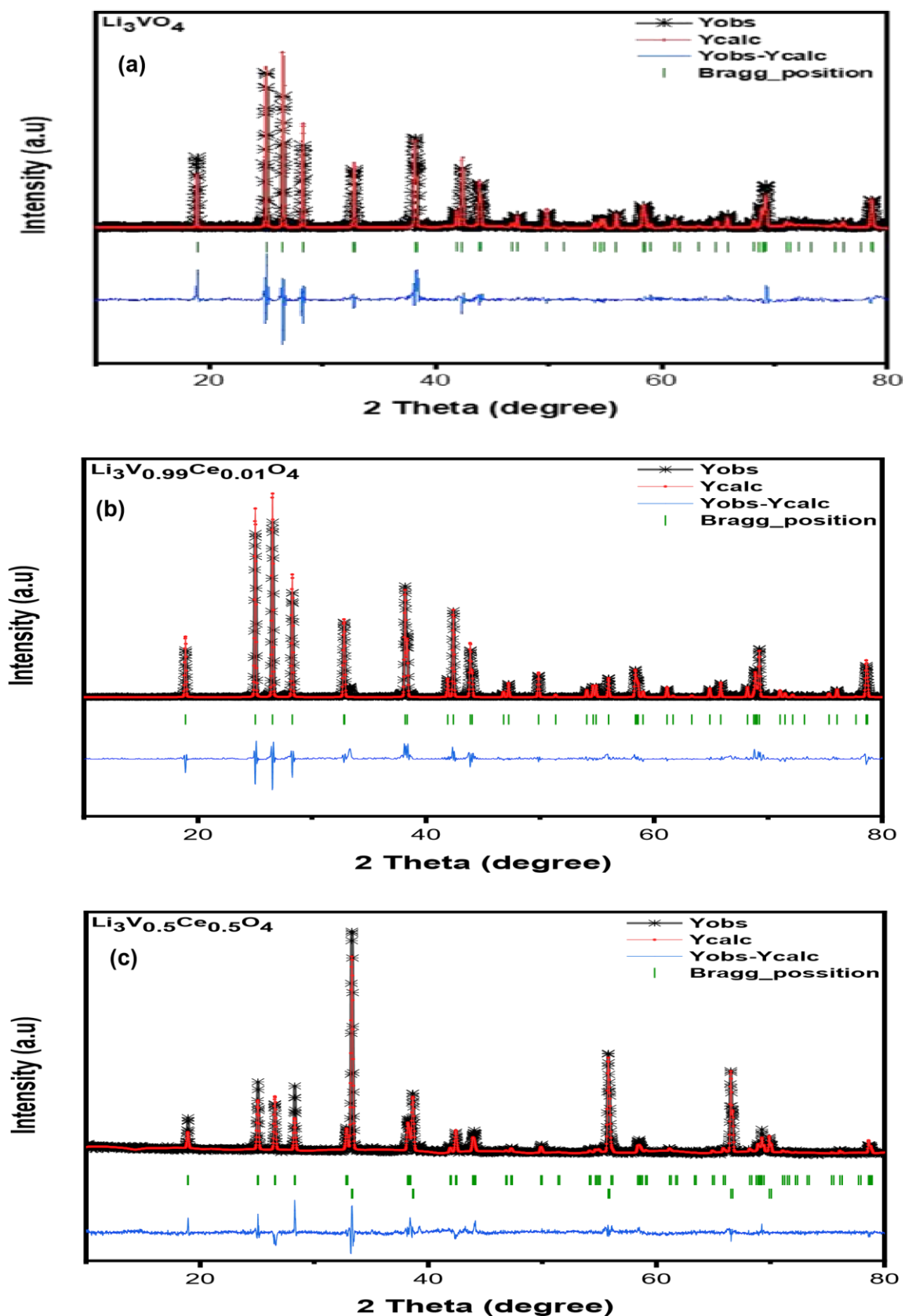


Figure 4.8 Typical results of Rietveld refinement of $\text{Li}_3\text{V}_{(1-x)}\text{Ce}_x\text{O}_4$: (a) $x = 0.0$; (b) $x = 0.01$; (c) $x = 0.5$.

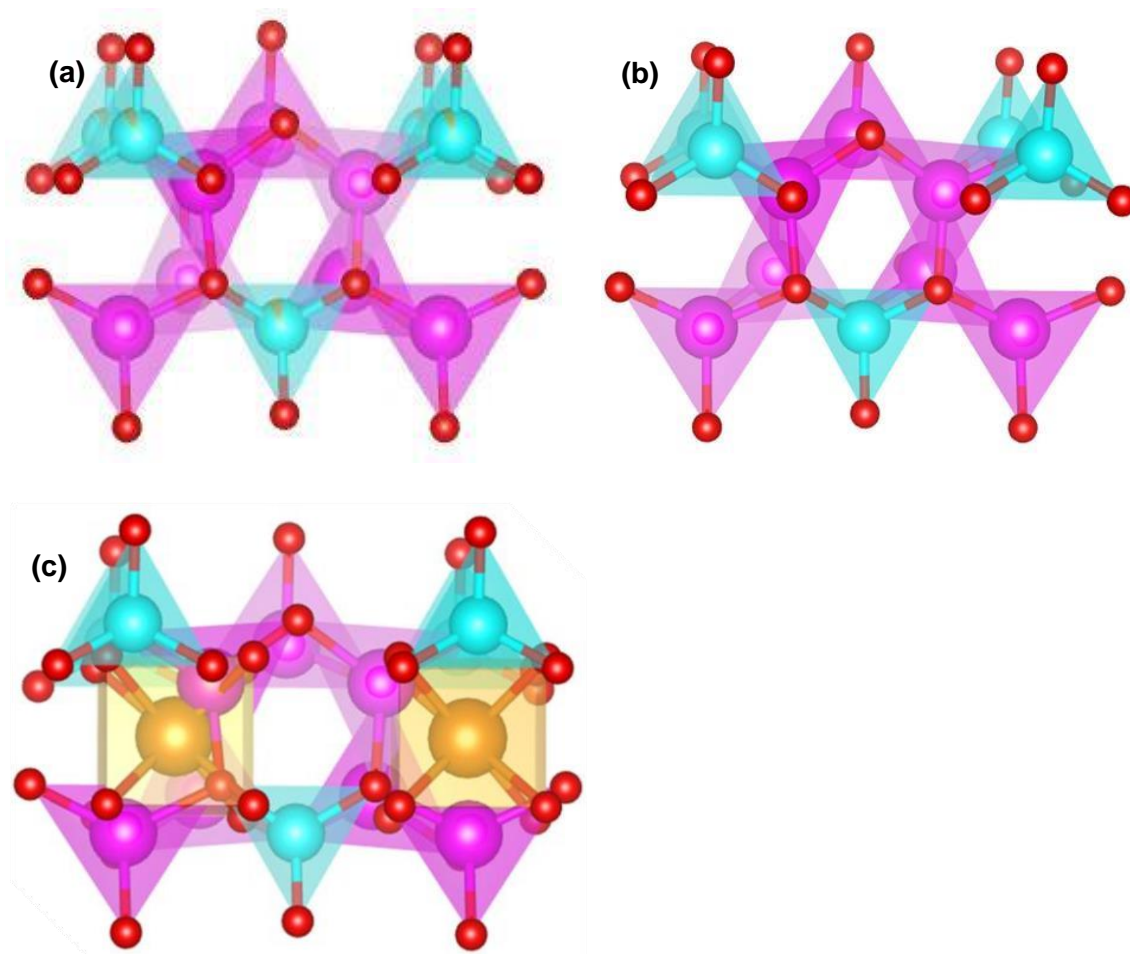


Figure 4.9 Crystal structures of $\text{Li}_3\text{V}_{(1-x)}\text{Ce}_x\text{O}_4$ samples for (a) $x = 0$; (b) $x = 0.05$; (c) $x = 0.5$. Blue atoms = Vanadium, Purple atoms = Lithium, Red atoms = Oxygen, and Orange atom parts = Cerium.

Table 4.5 Calculated lattice parameters of $\text{Li}_3\text{V}_{(1-x)}\text{Ce}_x\text{O}_4$ samples, based on XRD data refinement.

Sample	a [Å]	b [Å]	c [Å]	V (Å ³)	Crystallite size (D) nm
$x = 0.00$	6.32184	5.44279	4.94440	170.489	32.00
$x = 0.01$	6.32320	5.44363	4.94876	170.520	26.68
$x = 0.05$	6.32582	5.44677	4.95028	170.546	33.94
$x = 0.1$	6.32992	5.44991	4.95682	170.582	32.84
$x = 0.3$	6.31211	5.43306	4.93467	170.443	28.46
$x = 0.5$	6.30421	5.42516	4.92677	170.320	36.42

The SEM images in Figure 4.10 show the morphologies of the as-prepared Li_3VO_4 and Ce doped Li_3VO_4 . Agglomerated porous particles with non-uniform particle size

can be seen in Figure 4.10(b-d). At a low concentration of dopant Ce in Figure 4.10(b-c), smaller particles with average particle size ranging from 80 nm – 2 μ m can be seen; the particle size increases with increasing dopant concentration as can be seen in Figure 4.10(c), where $x = 0.5$; the particles are bigger than those when $x < 0.5$. The porosity of the particles could facilitate the transport of lithium ions while uniformity and particle size of the electrode material play an important role in improving the electrochemical performance of the battery (Zhao *et al.*, 2018; Zhao *et al.*, 2015). The EDS mapping indicates the presence of V, O, Ce, and C (Figure 4.11, Table 4.6), distributed uniformly (Figure 4.5 (b-c)); the presence of carbon is due to the use of carbon (conducting layer) as a coating agent for SEM analysis while Li cannot be detected since it has very low energy of characteristic radiation.

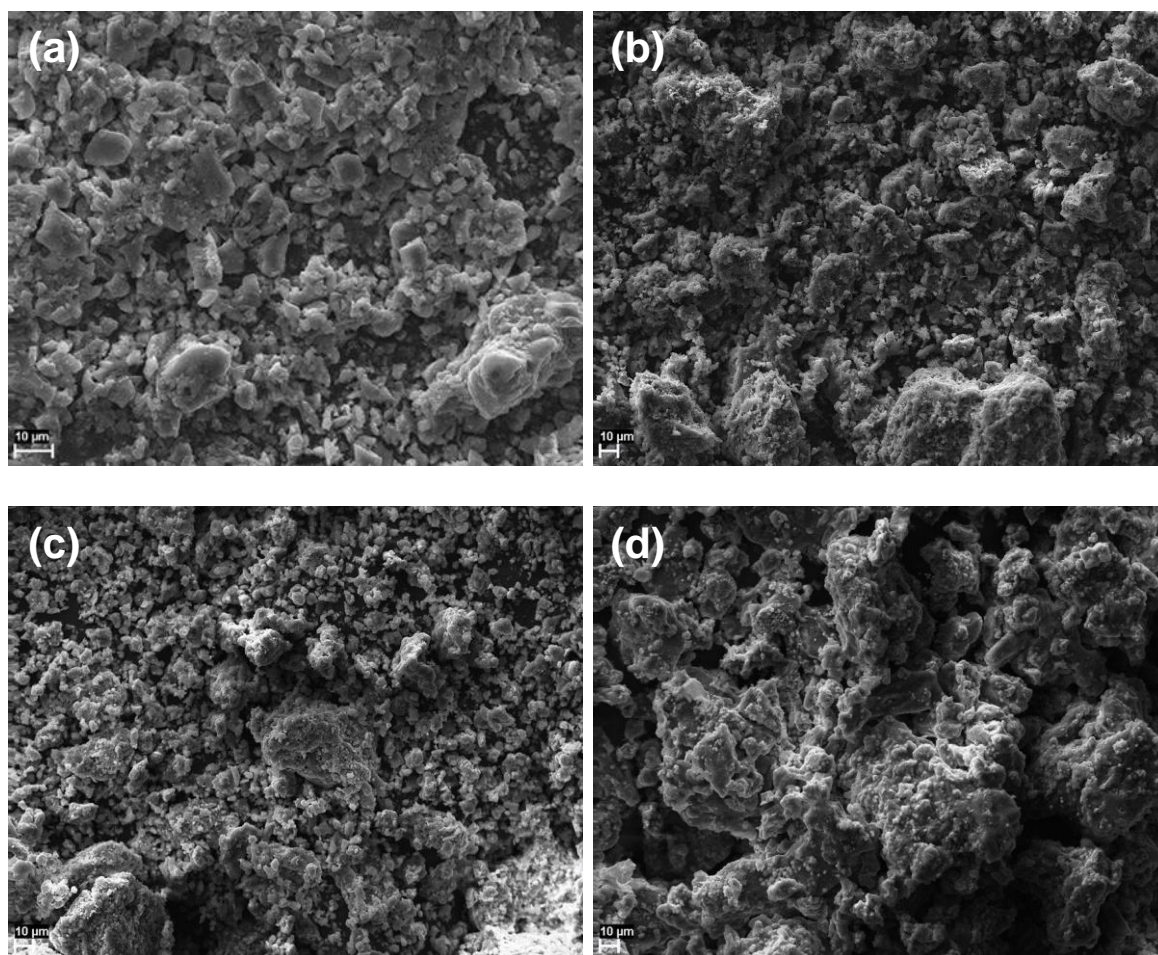


Figure 4.10 SEM images of $\text{Li}_3\text{V}_{1-x}\text{Ce}_x\text{O}_4$ samples: (a) $x = 0$, (b) $x = 0.01$, (c) $x = 0.3$, (d) $x = 0.5$.

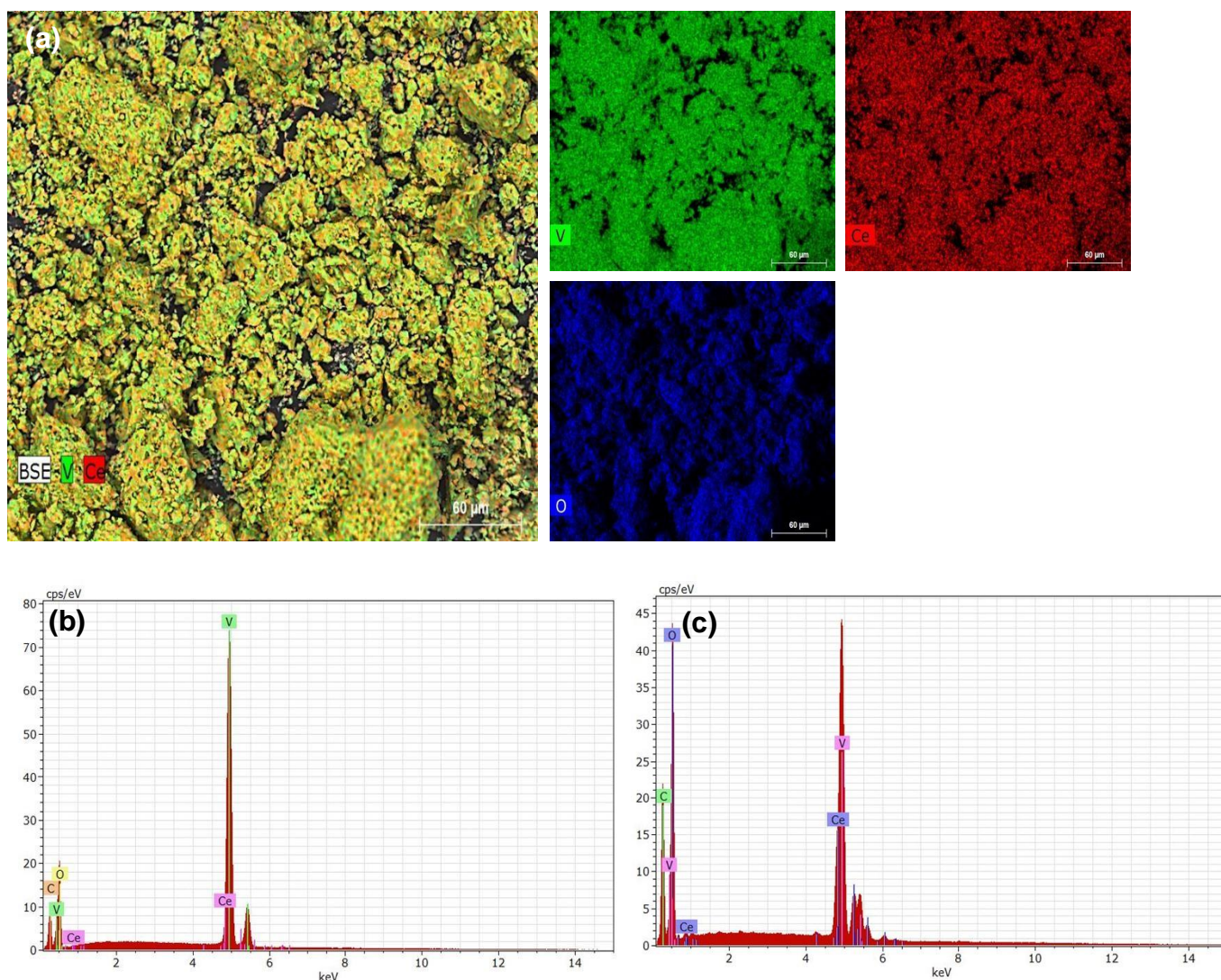


Figure 4.11 (a) EDS mappings of related elements for $\text{Li}_3\text{V}_{1-x}\text{Ce}_x\text{O}_4$ ($x = 0.01$); EDS spectra of (b) $\text{Li}_3\text{V}_{0.99}\text{Ce}_{0.01}\text{O}_4$. and (c) $\text{Li}_3\text{V}_{0.5}\text{Ce}_{0.5}\text{O}_4$.

Table 4.6 Semi-quantitative energy dispersive X-ray microanalysis (wt.%) of the EDS for all the samples.

Sample x	O (wt.%)	V (wt.%)	Ce (wt.%)
0.00	33.5	66.5	
0.01	27.4	67.9	4.7
0.05	30.2	62.6	7.2
0.1	31.8	58.9	9.3
0.3	38.4	27.5	32.1
0.5	40.4	41.2	20.4

4.2.4 Chromium Doped Lithium Vanadates, $\text{Li}_3\text{V}_{1-x}\text{Cr}_x\text{O}_4$

Figure 4.12(a) shows the XRD pattern of Li_3VO_4 and a series of Cr-doped Li_3VO_4 samples. All the diffraction peaks could be indexed to the low-temperature orthorhombic phase Li_3VO_4 which belongs to the $Pmn21$ (31) space group (crystallography open database file number 1528868, entry number 96-152-8869) without any peak of impurity (single-phase), showing that Cr^{3+} has successfully substituted V^{5+} to form $\text{Li}_3\text{V}_{1-x}\text{Cr}_x\text{O}_4$ ($0.01 \leq x \leq 0.5$), similar to Fe^{3+} (Liu *et al.*, 2019) and Ti^{4+} doping (Mu *et al.*, 2017). Figure 4.12(b) shows the expanded region between 35° and 37° (peak (200)), showing that the diffraction of the doped sample has shifted to a lower 2θ value compared to that of undoped Li_3VO_4 ($x = 0$); thus, Cr doping has enlarged the interlayer spacing. All the peaks are well defined and sharp indicated that the prepared samples are crystalline.

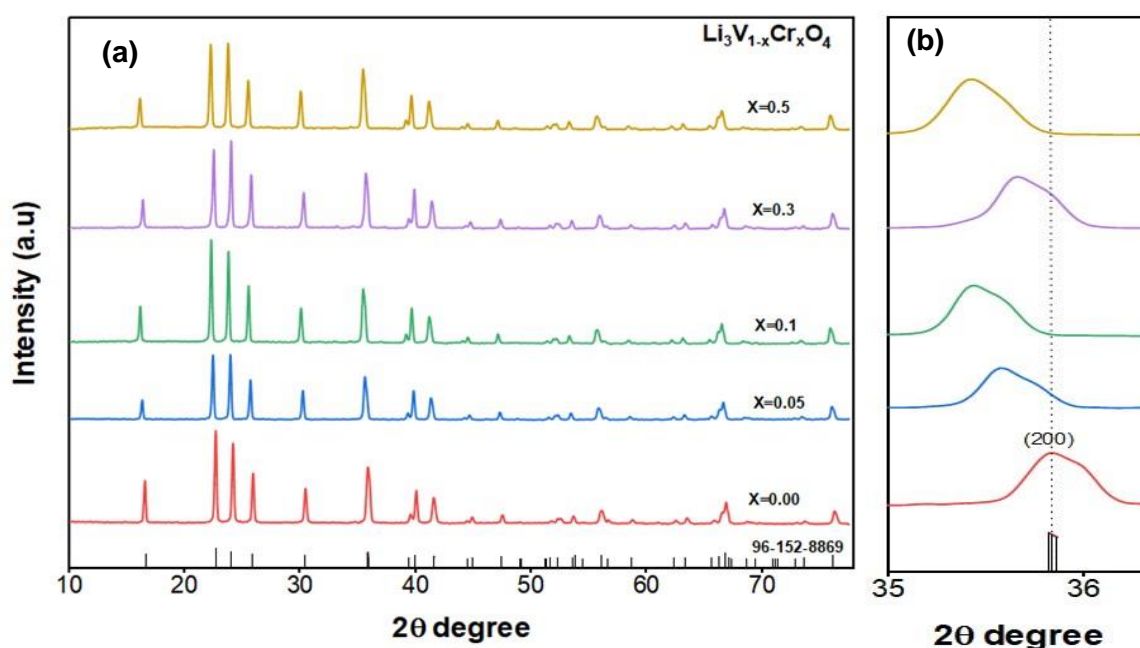


Figure 4.12 (a) XRD pattern of $\text{Li}_3\text{V}_{(1-x)}\text{Cr}_x\text{O}_4$ ($x = 0.0$, $x = 0.05$, $x = 0.1$, $x = 0.3$ and $x = 0.5$); (b) enlargement of the XRD pattern between 35° and 38° 2θ values.

To further understand the effect of Cr doping on the Li_3VO_4 crystal structure, Rietveld refinement of the XRD patterns was carried out (Table 4.7) using Match XRD with Fullprof software (Rodriguez-Carjaval, 2001); the single Li_3VO_4 phase with space group $Pmn21$ was selected as the initial refining structure. Refined XRD patterns are shown in Figure 4.13(a-c) for the samples with $x = 0$, $x = 0.05$, $x = 0.5$, and their

crystal structures (Figure 4.14(a-c)) were drawn based on the refinement results. The Cr doping does not break the orthorhombic Li_3VO_4 crystal structure, remaining stable as in Figure 4.14(a). The lattice parameters are listed in Table 4.8 and show a slight lattice expansion as evidenced in the values of a , b , c , and volume V , caused by doping with Cr. As represented in Figure 4.14(b) the Cr ions share the tetrahedron 2a site with V ions, upon the increase in the concentration of Cr ions (Figure 4.14(c)), the uniform incorporation of Cr ions into the structure becomes clearer.

Table 4.7 The key structure parameters of $\text{Li}_3\text{V}_{0.99}\text{Cr}_{0.01}\text{O}_4$ ($x = 0.01$) obtained by Rietveld refinement.

Atom	Site	X	Y	Z
Li1	4b	0.24700	0.33150	0.98720
Li2	2a	0.50000	0.83260	0.98480
O1	4b	0.22390	0.68040	0.89100
O2	2a	0.00000	0.12960	0.89520
O3	2a	0.50000	0.17360	0.84780
V1	2a	0.00000	0.82961	0.00000
Cr1	2a	0.00000	0.82961	0.00000

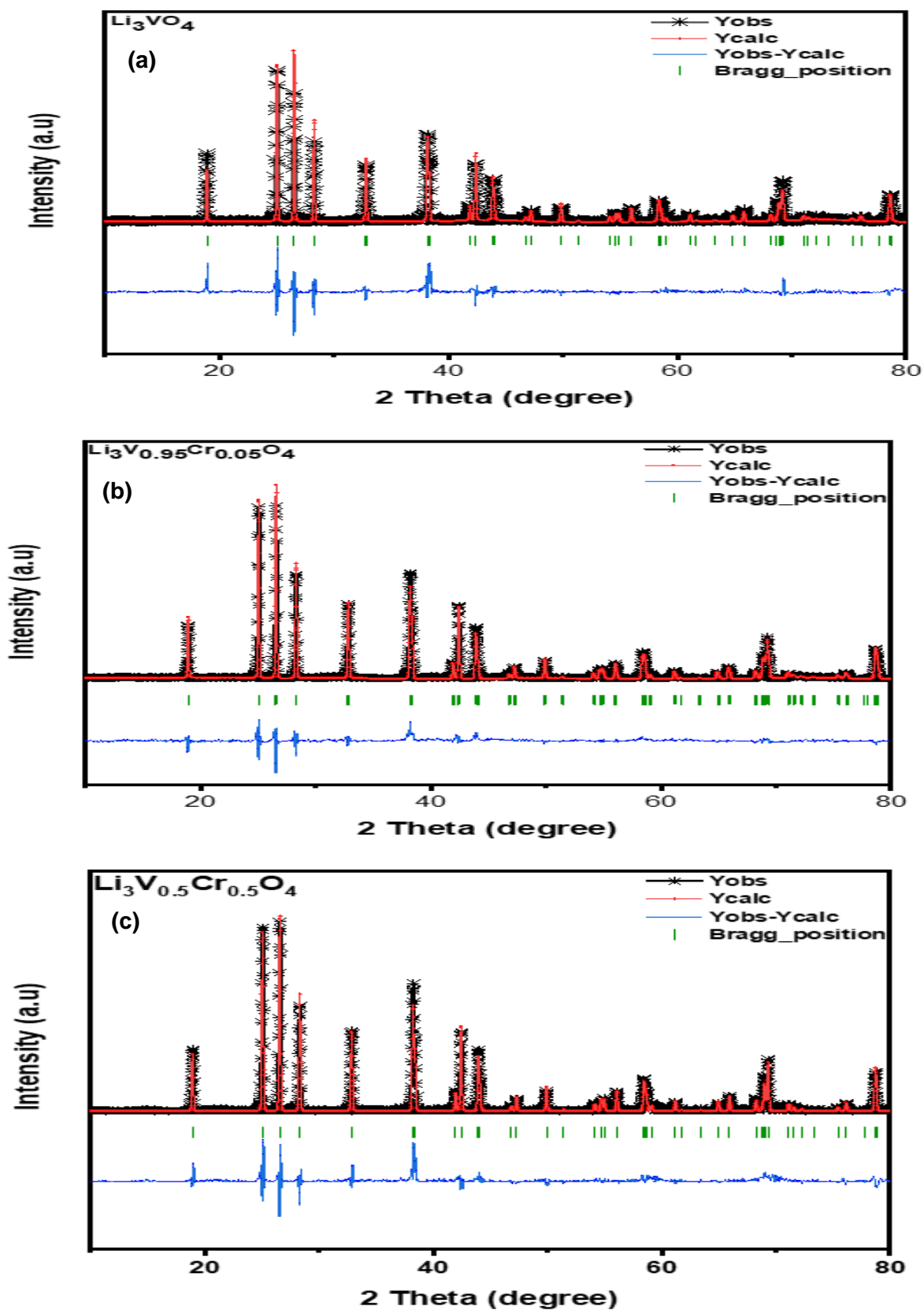


Figure 4.13 Typical results of Rietveld refinement of $\text{Li}_3\text{V}_{(1-x)}\text{Cr}_x\text{O}_4$: (a) $x = 0$; (b) $x = 0.05$; (c) $x = 0.5$.

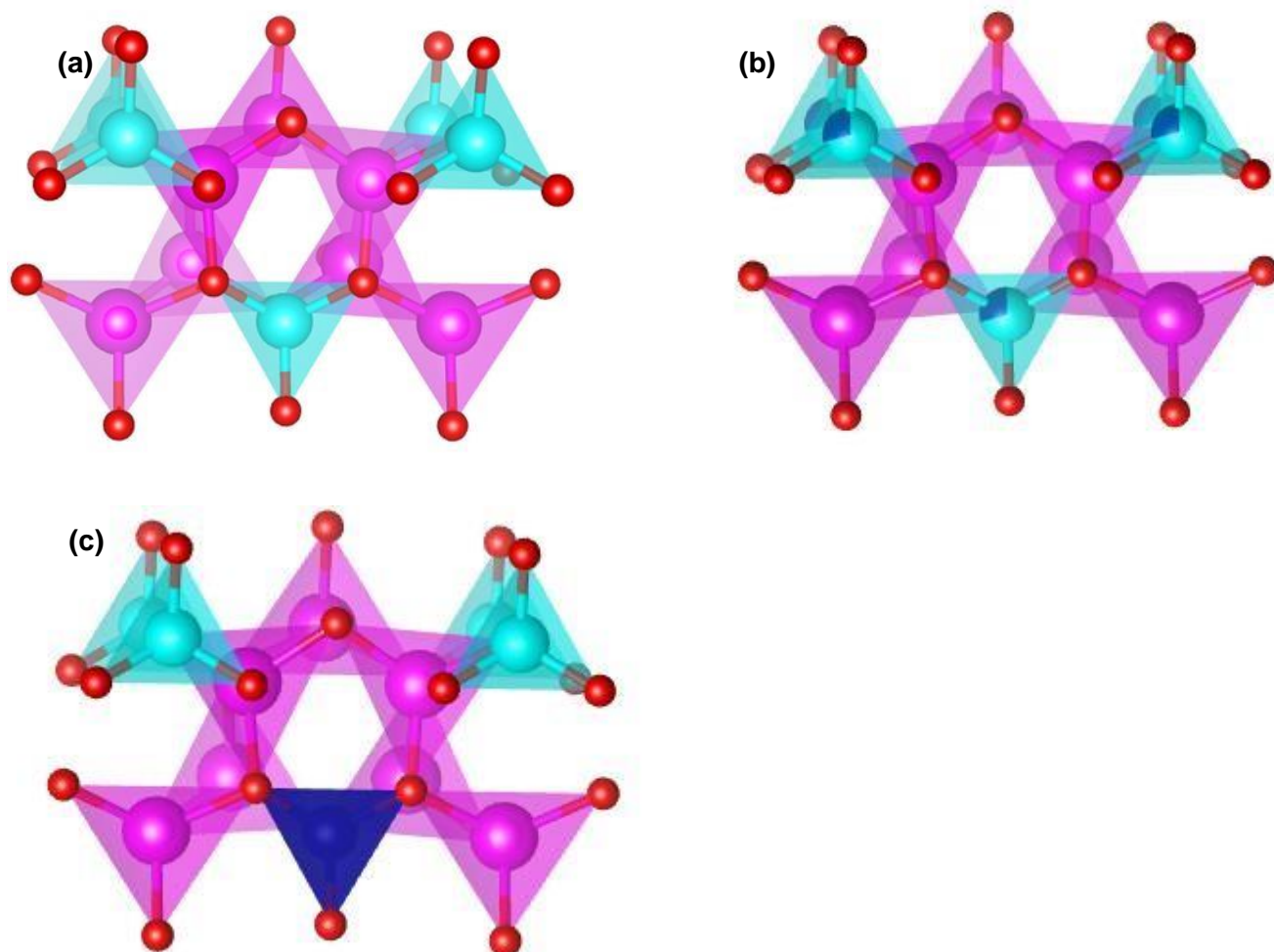


Figure 4.14 Crystal structures of $\text{Li}_3\text{V}_{(1-x)}\text{Cr}_x\text{O}_4$ samples for (a) $x = 0$; (b) $x = 0.05$; (c) $x = 0.5$. Blue atoms = Vanadium, Purple atoms = Lithium, Red atoms = Oxygen and Dark Blue atom parts = Chromium.

The tunnel structure of corner-sharing adjacent LiO_4 and CrO_4 tetrahedrons present in the doped samples causes an increase in the lattice parameters. It should be mentioned that the slight lattice expansion of Cr doped Li_3VO_4 should be beneficial for the intercalation and deintercalation of lithium ions, leading to more rapid Li-ion diffusion. The crystallite size (D) was calculated using Scherrer's Eq. 4.1 (Iqbal et al., 2007) from the broadening of the peaks and the approximate crystallite size of samples ranges from $20\text{-}32 \pm 0.01$ nm.

Table 4.8 Calculated lattice parameters of $\text{Li}_3\text{V}_{(1-x)}\text{Cr}_x\text{O}_4$ samples, based on XRD data refinement.

Sample	a [Å]	b [Å]	c [Å]	V (Å ³)	Crystallite size (D) nm
$x = 0.00$	6.32184	5.44279	4.94440	170.488	32.00
$x = 0.05$	6.32040	5.44280	4.94180	170.482	26.04
$x = 0.1$	6.31937	5.44107	4.93350	170.312	23.820
$x = 0.3$	6.31241	5.43521	4.91633	170.392	22.44
$x = 0.5$	6.31030	5.42610	4.90694	170.237	19.98

The SEM image (Figure 4.15(a)) of the as-prepared Li_3VO_4 polycrystalline powder shows agglomerated particles with particle size ranging from 200 nm to 10 μm , while the EDS mapping (Table 4.9) indicates the presence of V, O, and Cr. The presence of carbon is due to the use of carbon (conducting layer) as a coating agent for SEM analysis while Li cannot be detected since it has very low energy of characteristic radiation. Figure 4.15(b-d) shows the morphologies of the Cr-doped Li_3VO_4 series with $x = 0.01$, $x = 0.1$, $x = 0.5$, like undoped Li_3VO_4 . Figure 4.15(b) shows agglomerated particles to chunks with non-uniform particle size. However, Figure 4.15(c, d) shows more uniform particles with smaller particle sizes (average from 90 nm to 5 μm) compared to the particles of the undoped Li_3VO_4 (Figure 4.15(a)). It should be mentioned that the uniformity and particle size of the electrode material play an important role in improving the electrochemical performance of the battery (Zhao *et al.*, 2018; Zhao *et al.*, 2015). The EDS mapping in Figure 4.16 (a-c) shows that the elements V, O, and Cr are distributed uniformly in $\text{Li}_3\text{V}_{0.99}\text{Cr}_{0.01}\text{O}_4$. Figure 4.16 c clearly shows the increase of the Cr intensity as the concentration of the Cr ion doped into Li_3VO_4 is increased and the EDS spectrum doesn't show any foreign elements.

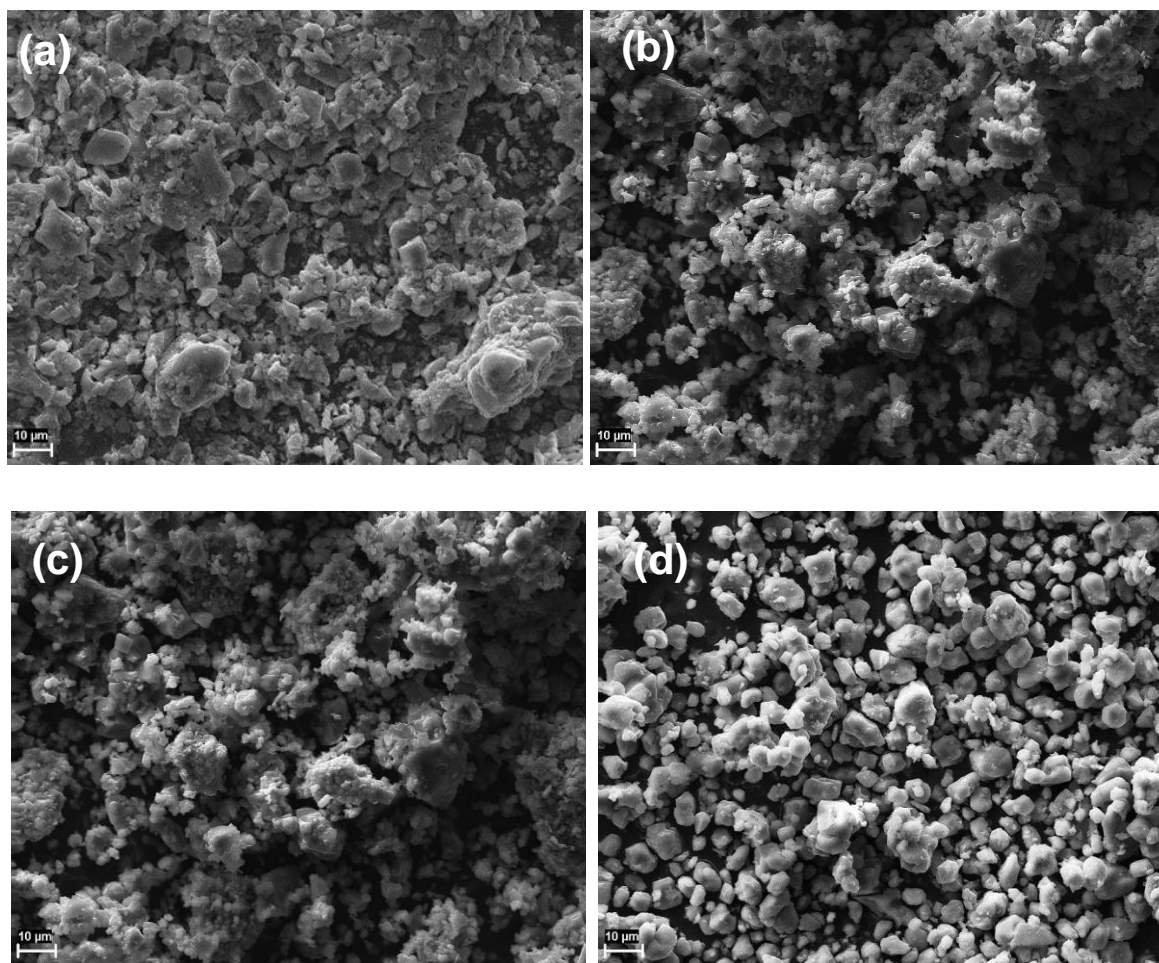


Figure 4.15 The SEM images of $\text{Li}_3\text{V}_{1-x}\text{Cr}_x\text{O}_4$ samples: (a) $x = 0$, (b) $x = 0.01$, (c) $x = 0.3$, (d) $x = 0.5$.

Table 4.9 Semi-quantitative energy dispersive X-ray microanalysis (wt.%) of the EDS for all the samples.

Sample x	O (wt.%)	V (wt.%)	Cr (wt.%)
0.00	33.5	66.5	
0.05	31.7	66.1	2.2
0.1	38.0	58.4	3.5
0.3	38.4	55.5	6.1
0.5	44.7	46.2	9.1

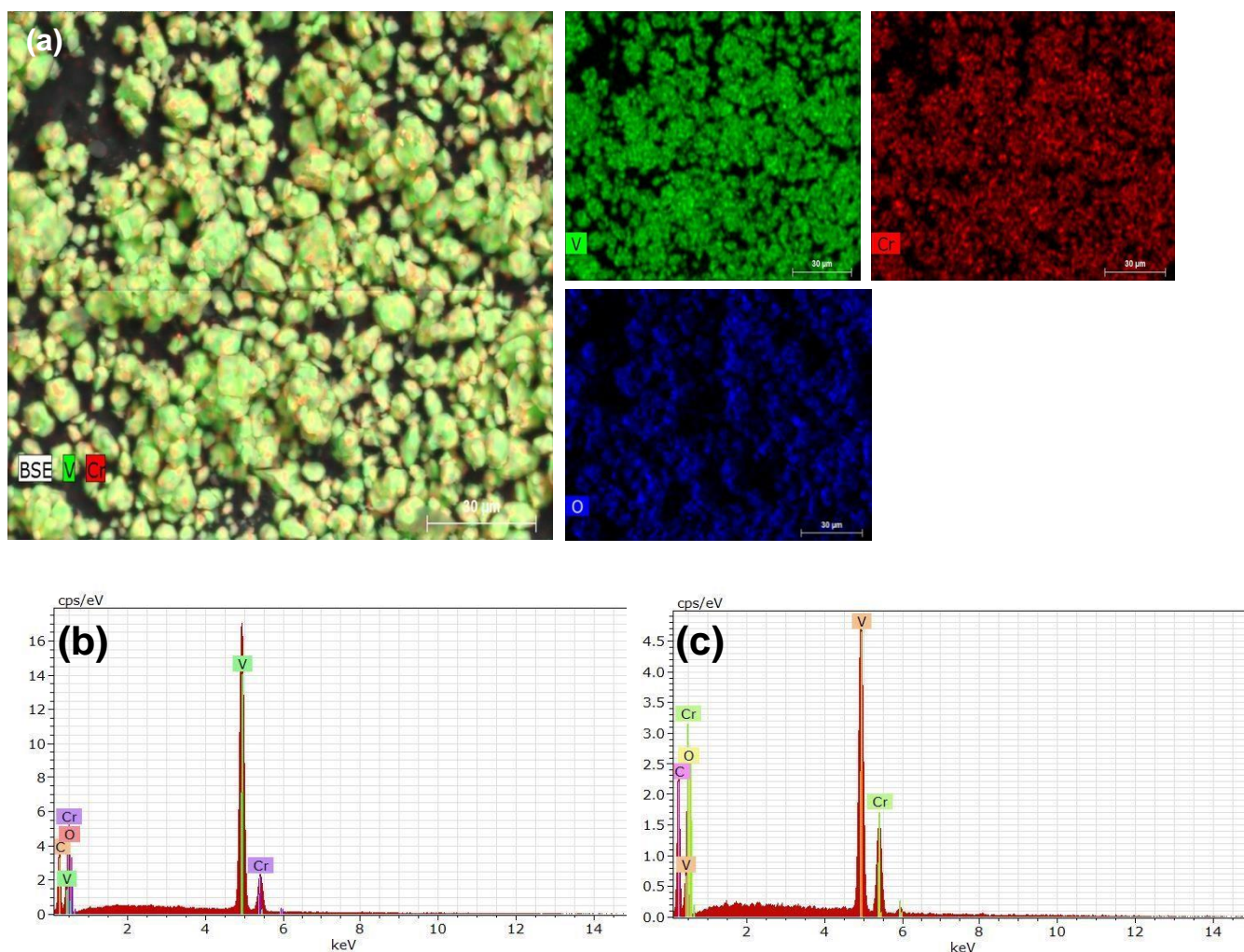


Figure 4.16 (a) EDS mappings of elements of $\text{Li}_3\text{V}_{1-x}\text{Cr}_x\text{O}_4$ ($x = 0.01$); EDS spectra of (b) $\text{Li}_3\text{V}_{0.95}\text{Cr}_{0.05}\text{O}_4$ and (c) $\text{Li}_3\text{V}_{0.5}\text{Cr}_{0.5}\text{O}_4$.

4.2.5 Magnesium Doped Lithium Vanadates, $\text{Li}_3\text{V}_{1-x}\text{Mg}_x\text{O}_4$

Figure 4.17(a) shows the XRD pattern of Li_3VO_4 and a series of Mg-doped Li_3VO_4 samples. The peaks in these patterns can be assigned to the low-temperature orthorhombic phase of Li_3VO_4 which belongs to the $Pmn21$ (31) space group (crystallography open database file number 1528868, entry number 96-152-8869). At low Mg content, there are only single-phase Li_3VO_4 indicating that Mg^{2+} successfully substituted V^{5+} to form $\text{Li}_3\text{V}_{(1-x)}\text{Mg}_x\text{O}_4$ (for $x < 0.1$). However, at high Mg content ($x \geq 0.1$) the presence of MgO is evident, due to the ionic radius of Mg^{2+} (0.72 Å) (Hashem *et al.*, 2019) that is greater than that of V^{5+} (0.355 Å) (Zhao *et al.*, 2018). Figure 4.17(b) shows the expanded region between 30° and 31° (peak (111)),

showing that the diffraction of the doped sample has shifted to a lower 2θ value compared to undoped Li_3VO_4 ($x = 0$); thus, Mg doping has enlarged the interlayer spacing. To further understand the effect of Mg doping on the Li_3VO_4 crystal structure, Rietveld refinement of the XRD patterns was carried out using Match XRD with Fullprof software (Rodriguez-Carjaval, 2001); the single Li_3VO_4 phase with space group $Pmn21$ was selected as the initial refining structure (Table 4.10). Refined XRD patterns are shown in Figure 4.18(a-c) for the samples with $x = 0$, $x = 0.01$, and $x = 0.50$, and their crystal structures (Figure 4.19(a-c)) were drawn based on the refinement results. The Mg doping does not break the orthorhombic Li_3VO_4 crystal structure, remaining stable as in Figure 4.19(a). The lattice parameters are listed in Table 4.11 and show a slight lattice expansion as evidenced in the values of a , b , c , and volume V , caused by doping with Mg. Figure 4.19(c) shows that the doped Mg ions mainly occupy V sites. The tunnel structure of corner-sharing adjacent LiO_4 and MgO_4 tetrahedra present in the doped samples causes an increase in the lattice parameters. It should be mentioned that the slight lattice expansion of Mg-doped Li_3VO_4 should be beneficial for the intercalation and deintercalation of lithium ions, leading to more rapid Li-ion diffusion.

Table 4.10 The key structure parameters of $\text{Li}_3\text{V}_{0.99}\text{Mg}_{0.01}\text{O}_4$ ($x = 0.01$) obtained by Rietveld refinement.

Atom	Site	x	y	z
Li1	4b	0.24700	0.33150	0.98720
Li2	2a	0.50000	0.83260	0.98480
O1	4b	0.22390	0.68040	0.89100
O2	2a	0.00000	0.12960	0.89520
O3	2a	0.50000	0.17360	0.84780
V1	2a	0.00000	0.82961	0.00000
Mg1	2a	0.00000	0.82961	0.00000

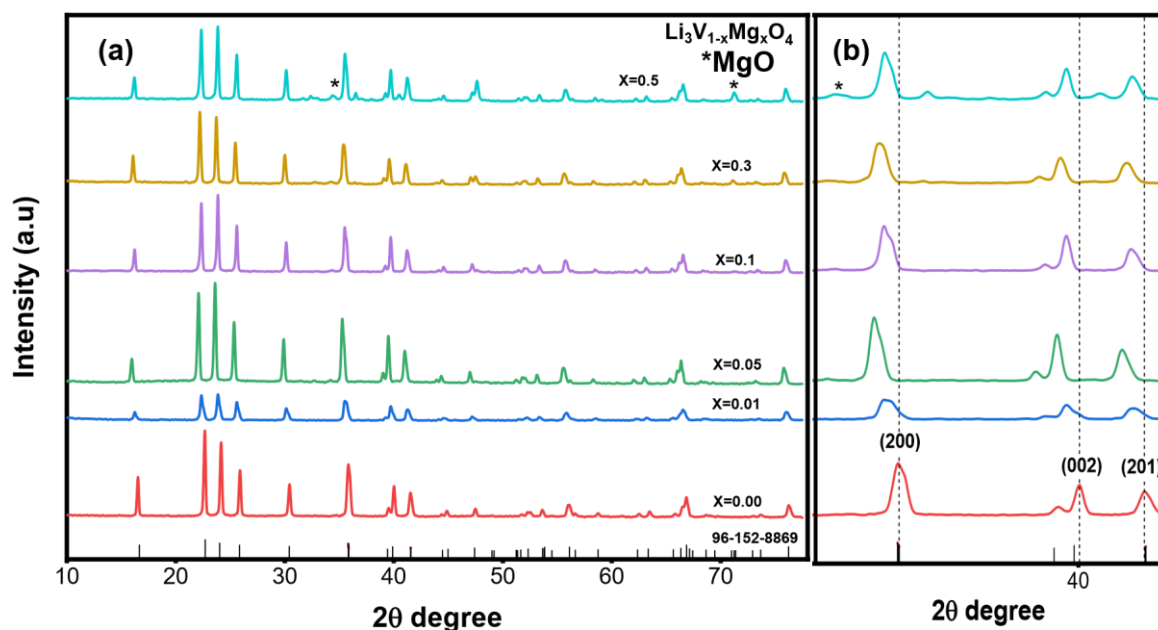


Figure 4.17 (a) XRD pattern of $\text{Li}_3\text{V}_{1-x}\text{Mg}_x\text{O}_4$ ($x = 0.0, x = 0.05, x = 0.1, x = 0.3$ and $x = 0.5$); (b) enlargement of the XRD pattern between 35° and $38^\circ 2\theta$ values.

Table 4.11 Calculated lattice parameters of $\text{Li}_3\text{V}_{1-x}\text{Mg}_x\text{O}_4$ samples, based on XRD data refinement.

Sample	a [Å]	b [Å]	c [Å]	V (Å ³)	Crystallite size (D) nm
$x = 0.00$	6.32184	5.44279	4.94440	170.488	32.00
$x = 0.01$	6.32457	5.44555	4.94541	170.482	33.05
$x = 0.05$	6.32284	5.44684	4.94682	170.462	30.82
$x = 0.1$	6.32124	5.43925	4.94104	170.370	24.74
$x = 0.3$	6.32199	5.44117	4.94228	170.414	23.43
$x = 0.5$	6.32018	5.43134	4.93957	170.207	22.62

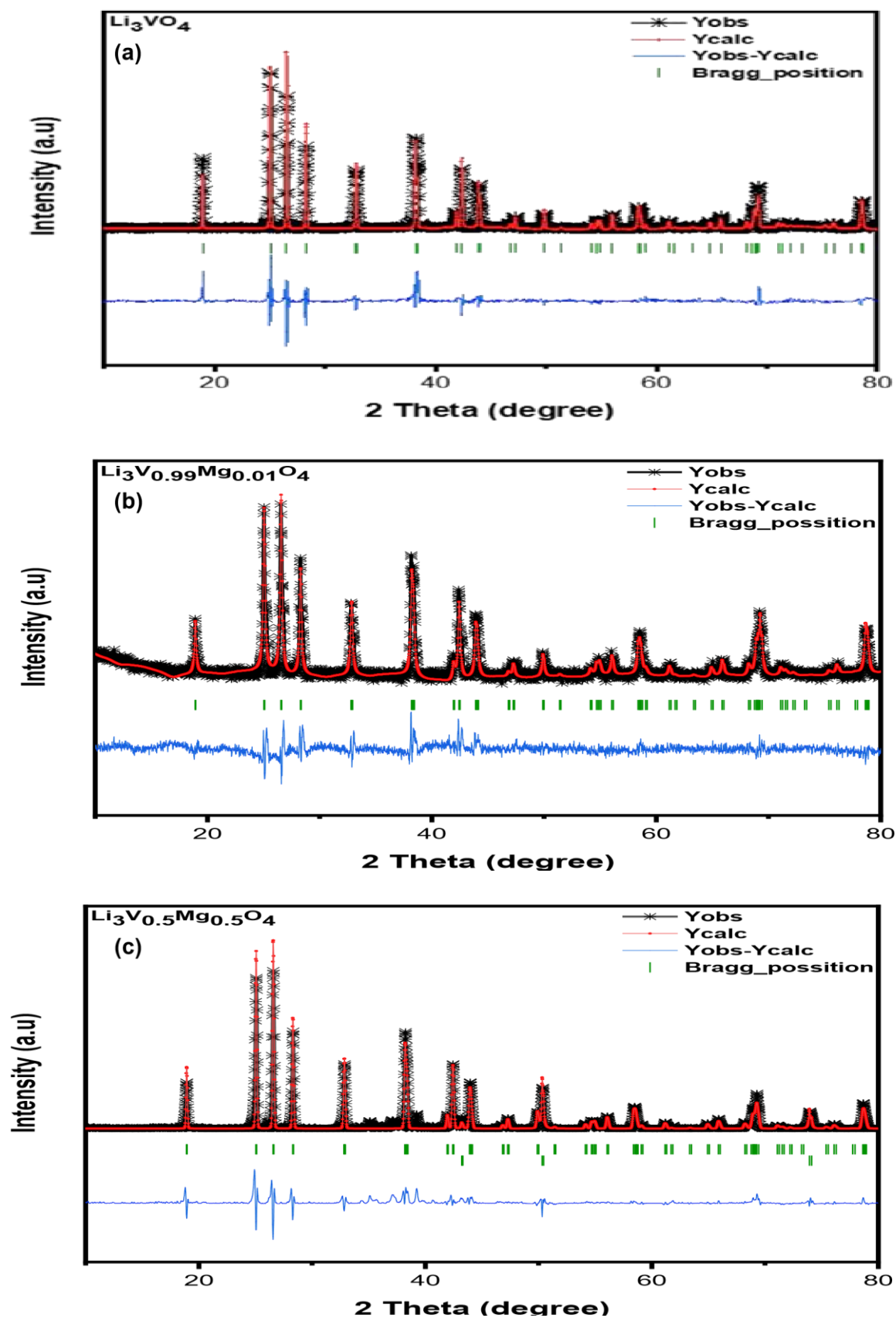


Figure 4.18 Typical results of Rietveld refinement of $\text{Li}_3\text{V}_{1-x}\text{Mg}_x\text{O}_4$: (a) $x = 0.0$, (b) $x = 0.01$, (c) $x = 0.5$.

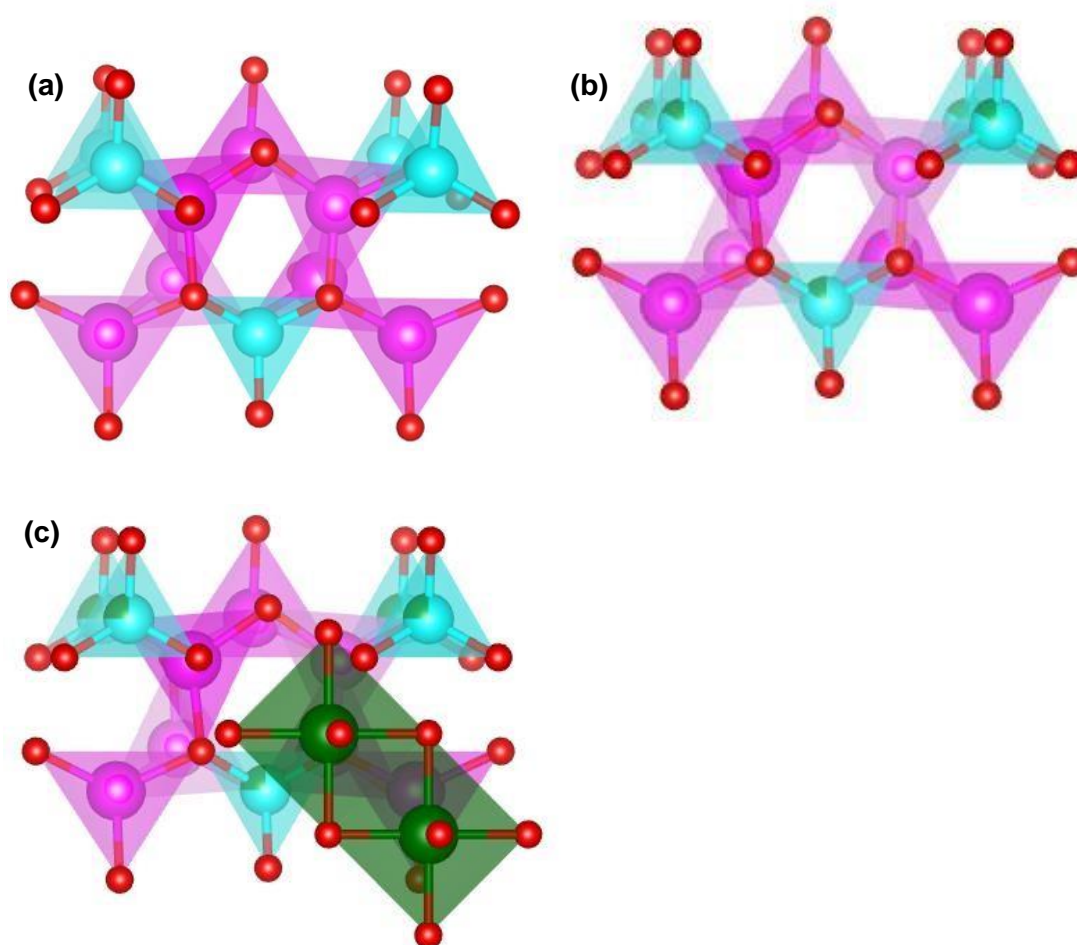


Figure 4.19 (a) Crystal structures of $\text{Li}_3\text{V}_{1-x}\text{Mg}_x\text{O}_4$ samples for $x = 0$, $x = 0.05$ and $x = 0.5$, Blue atoms = Vanadium, Purple atoms = Lithium, Red atoms = Oxygen and Green atom = Magnesium.

The SEM image (Figure 4.20 (a)) of the as-prepared Li_3VO_4 polycrystalline powder shows agglomerated particles with particle size ranging from 200 nm to 100 nm, while the EDS mapping (Table 4.12) indicates the presence of V, O, and Mg. The presence of carbon is due to the use of carbon (conducting layer) as a coating agent for SEM analysis while Li cannot be detected since it has a very low characteristic radiation energy. Figure 4.20(b-d) shows the morphologies of the Mg-doped Li_3VO_4 series with $x = 0.01$, $x = 0.1$, $x = 0.5$, similar to undoped Li_3VO_4 . Figure 4.20(b) shows agglomerated particles to chunks with non-uniform particle size. However, Figure 4.20(c, d) shows more uniform particles with smaller particle sizes (average from 90 nm to 5 μm) compared to the particles of the undoped Li_3VO_4 (Figure 4.20(a)). It should be mentioned that the uniformity and particle size of the electrode material play an important role in improving the electrochemical performance of the battery

(Zhao *et al.*, 2018; Zhao *et al.*, 2015). The EDS mapping in Figure 4.21 (a-c) shows that the elements V, O, and Mg are distributed uniformly in $\text{Li}_3\text{V}_{0.99}\text{Mg}_{0.01}\text{O}_4$, the EDS spectrum also shows some trace foreign elements (Si and Al) which are found in the sample coming from the MgOH which was used as the starting material for the source of Mg and where given as trace element less than 0.01%.

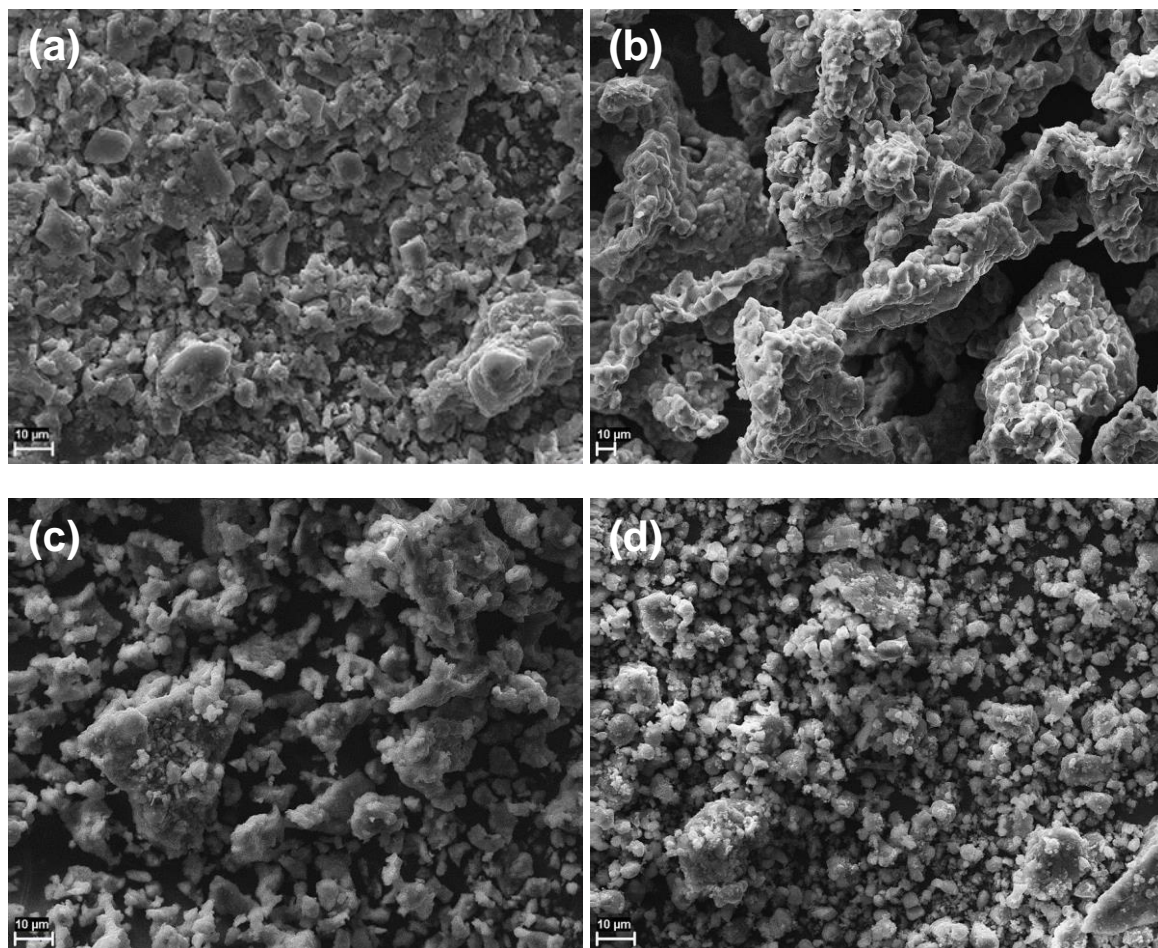


Figure 4.20 SEM images of $\text{Li}_3\text{V}_{1-x}\text{Mg}_x\text{O}_4$ samples: (a) $x = 0$, (b) $x = 0.01$, (c) $x = 0.3$, (d) $x = 0.5$.

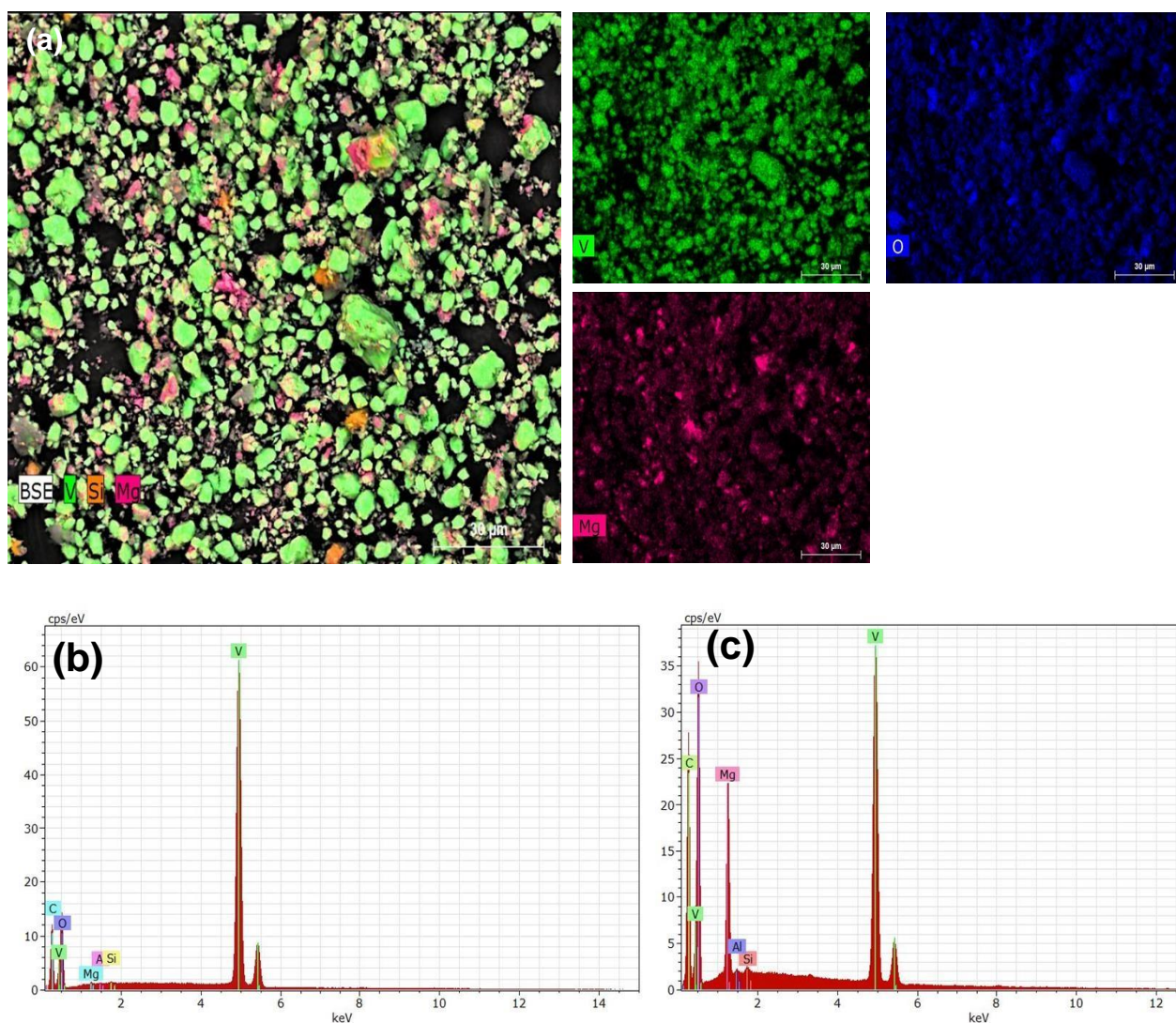


Figure 4.21 (a) EDS mappings of the elements of $\text{Li}_3\text{V}_{1-x}\text{Mg}_x\text{O}_4$ ($x = 0.01$); EDS spectra of (b) $\text{Li}_3\text{V}_{0.95}\text{Mg}_{0.05}\text{O}_4$ and (c) $\text{Li}_3\text{V}_{0.5}\text{Mg}_{0.5}\text{O}_4$.

Table 4.12 Semi-quantitative energy dispersive X-ray microanalysis (wt.%) of the EDS for all the samples.

Sample x	O (wt.%)	V (wt.%)	Mg (wt.%)
0.00	33.5	66.5	
0.01	27.4	67.9	4.7
0.05	30.2	62.6	7.2
0.1	31.8	58.9	9.3
0.3	38.4	27.5	32.1
0.5	40.4	41.2	20.4

4.2.6 Zinc Doped Lithium Vanadates, $\text{Li}_3\text{V}_{1-x}\text{Zn}_x\text{O}_4$

Figure 4.22(a) shows the XRD pattern of Li_3VO_4 and a series of Zn-doped Li_3VO_4 samples. The peaks in these patterns can be assigned to the low-temperature orthorhombic phase of Li_3VO_4 which belongs to the $Pmn21$ (31) space group (crystallography open database file number 1528868, entry number 96-152-8869). At low Zn concentration there is only single-phase Li_3VO_4 indicating that Zn^{2+} successfully substituted V^{5+} to form $\text{Li}_3\text{V}_{1-x}\text{Zn}_x\text{O}_4$ (for $x < 0.1$), as in Figure 4.22(b) the expanded region between 34° and 39° (peak (200)), showing that the diffraction of the doped sample has shifted to a lower 2θ value compared to undoped Li_3VO_4 ($x = 0$); thus, Zn doping has enlarged the interlayer spacing. However, at high Zn concentration, the presence of ZnO is evident, indicated by asterisks. As can be seen in Figure 4.22(b), the presence of the ZnO peak starts showing from $x = 0.05$, due to the ionic radius of Zn^{2+} (0.74 \AA) that is greater than that of V^{5+} (0.355 \AA) (Choi *et al.*, 2019).

To further understand the effect of Zn doping on the Li_3VO_4 crystal structure, Rietveld refinement of the XRD patterns was carried out using Match XRD with Fullprof software (Rodriguez-Carjaval, 2001); the single Li_3VO_4 phase with space group $Pmn21$ was selected as the initial refining structure (Table 4.13). Refined XRD patterns are shown in Figure 4.23(a-c) for the samples with $x = 0$, $x = 0.01$, and $x = 0.5$, and their crystal structures (Figure 4.24(a-c)) were drawn based on the refinement results. The Zn doping does not break the orthorhombic Li_3VO_4 crystal structure, remaining stable as shown in Figure 4.24(a). The lattice parameters are listed in Table 4.14 and show a slight lattice expansion as evidenced in the values of a , b , c , and volume V , caused by doping with Zn. Figure 4.24(a) shows that the doped Zn ions mainly occupy V sites. The tunnel structure of corner-sharing adjacent LiO_4 and ZnO_4 tetrahedra present in the doped samples causes an increase in the lattice parameters. It should be mentioned that the slight lattice expansion of Zn doped Li_3VO_4 should be beneficial for the intercalation and deintercalation of lithium ions, leading to more rapid Li-ion diffusion. The crystallite size (D) was calculated using Scherrer's Eq. 4.1 (Iqbal *et al.*, 2007) from the broadening of the peaks and the approximate crystallite size of samples ranges from $28\text{-}38 \pm 0.01 \text{ nm}$.

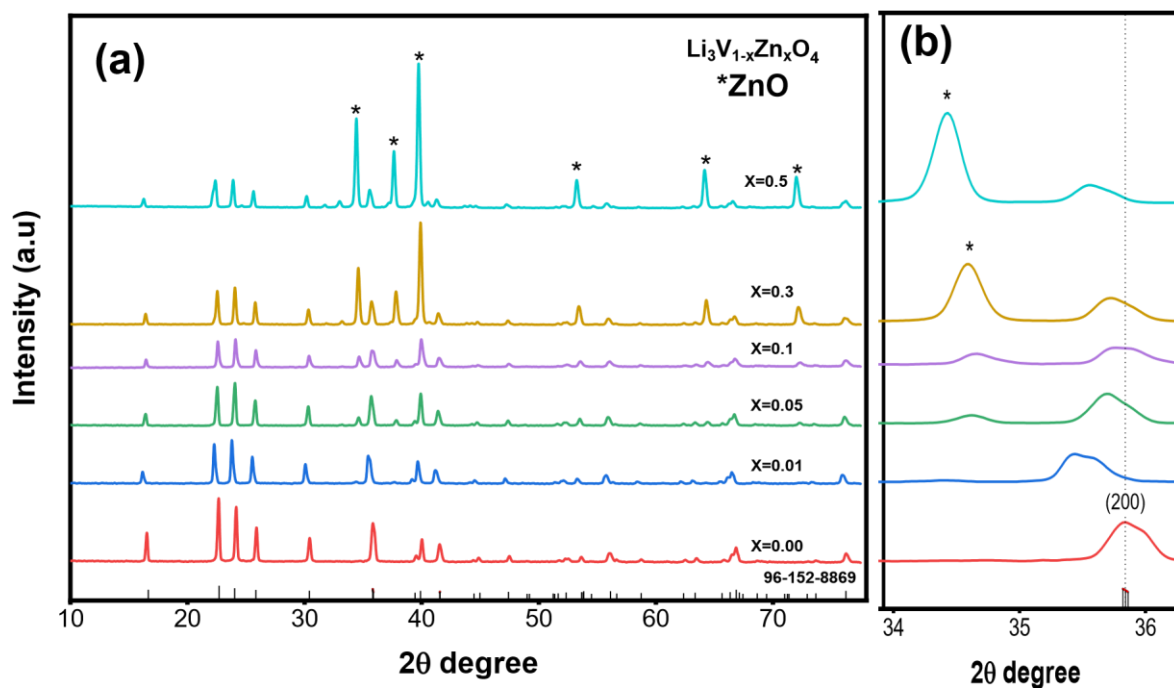


Figure 4.22 (a) XRD pattern of $\text{Li}_3\text{V}_{1-x}\text{Zn}_x\text{O}_4$ ($x = 0.0, x = 0.05, x = 0.1, x = 0.3$, and $x = 0.5$); (b) enlargement of the XRD pattern between 35° and 38° 2θ values.

Table 4.13 The key structure parameters of $\text{Li}_3\text{V}_{0.99}\text{Zn}_{0.01}\text{O}_4$ ($x = 0.01$) obtained by Rietveld refinement.

Atom	Site	x	y	z
Li1	4b	0.24700	0.33150	0.98720
Li2	2a	0.50000	0.83260	0.98480
O1	4b	0.22390	0.68040	0.89100
O2	2a	0.00000	0.12960	0.89520
O3	2a	0.50000	0.17360	0.84780
V1	2a	0.00000	0.82961	0.00000
Zn1	2a	0.00000	0.82961	0.00000

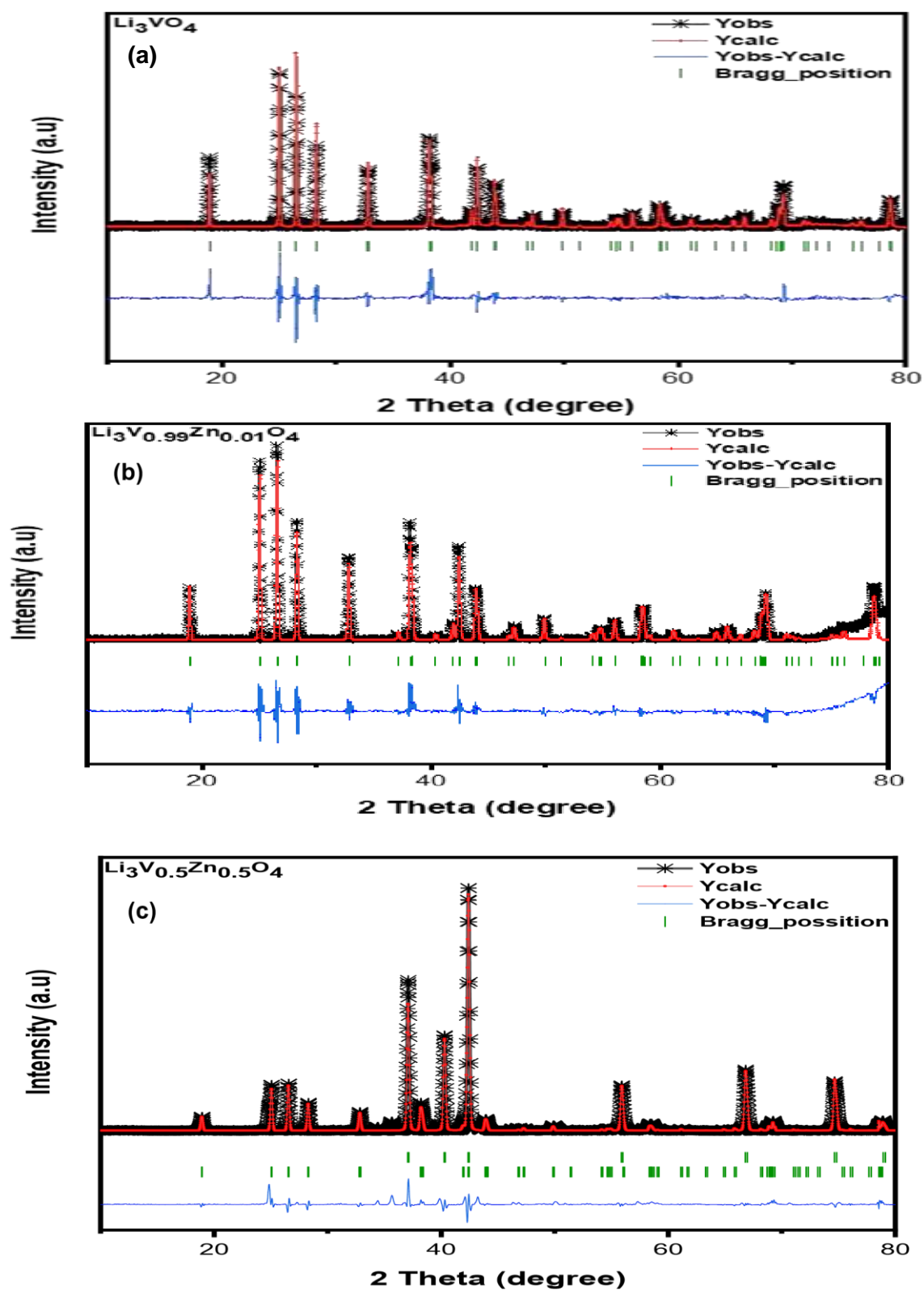


Figure 4.23 Typical results of Rietveld refinement of $\text{Li}_3\text{V}_{1-x}\text{Zn}_x\text{O}_4$: (a) $x = 0.0$, (b) $x = 0.01$, (c) $x = 0.5$.

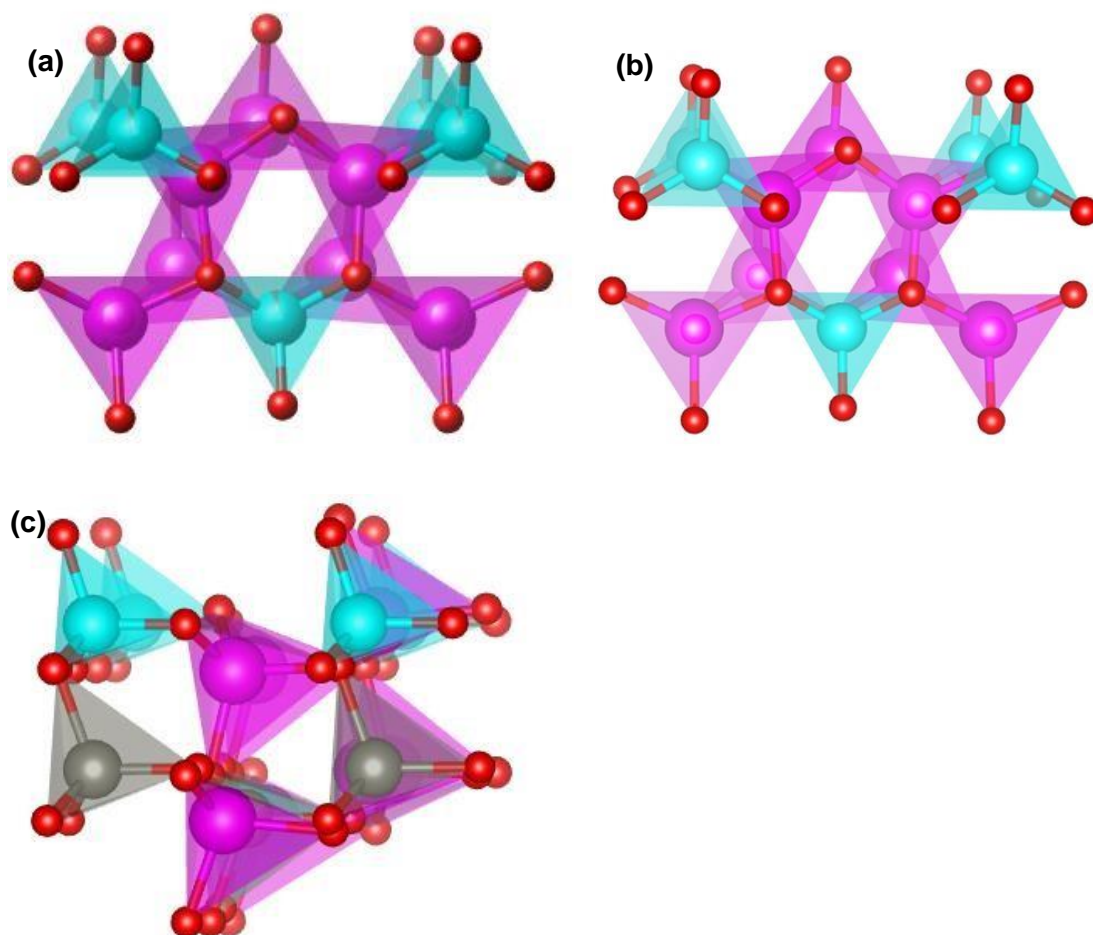


Figure 4.24 Crystal structures of $\text{Li}_3\text{V}_{1-x}\text{Zn}_x\text{O}_4$ samples for (a) $x = 0$; (b) $x = 0.05$; (c) $x = 0.5$, respectively. Blue atoms = Vanadium, Purple atoms = Lithium, Red atoms = Oxygen and Grey atom = Zinc.

Table 4.14 Calculated lattice parameters of $\text{Li}_3\text{V}_{1-x}\text{Zn}_x\text{O}_4$ samples, based on XRD data refinement.

Sample	a [Å]	b [Å]	c [Å]	V (Å ³)	Crystallite size (D) nm
$x = 0.00$	6.32184	5.44279	4.94440	170.489	32.00
$x = 0.01$	6.32593	5.44366	4.95240	170.512	34.82
$x = 0.05$	6.32750	5.44740	4.96086	170.520	32.65
$x = 0.1$	6.33101	5.44848	4.96885	170.549	33.00
$x = 0.3$	6.33384	5.44846	4.97015	170.603	29.75
$x = 0.5$	6.3346	5.44973	4.97192	170.794	33.54

The SEM image (Figure 4.25(a)) of the Li_3VO_4 polycrystalline powder shows agglomerated particles with particle size ranging from 200 nm to 100 nm, while the

EDS (Table 4.15) mapping indicates the presence of V, O, and C. The presence of carbon is due to the use of carbon (conducting layer) as a coating agent for SEM analysis while Li cannot be detected since it has very low energy of characteristic radiation. Figure 4.25(b-d) shows the morphologies of the Zn-doped Li_3VO_4 series with $x = 0.01$, $x = 0.1$, and $x = 0.5$, similar to undoped Li_3VO_4 . Figure 4.25(b) shows agglomerated particles to chunks with non-uniform particle size. However, Figure 4.25(c, d) shows more uniform particles with smaller particle sizes (average from 90 nm to 5 μm) compared to the particles of the undoped Li_3VO_4 (Figure 4.25(a)). It should be mentioned that the uniformity and particle size of the electrode material play an important role in improving the electrochemical performance of the battery (Zhao *et al.*, 2018; Zhao *et al.*, 2015). The EDS mapping in Figure 4.26(a-c) shows that the elements V, O, and Zn are distributed uniformly in $\text{Li}_3\text{V}_{0.99}\text{Zn}_{0.01}\text{O}_4$.

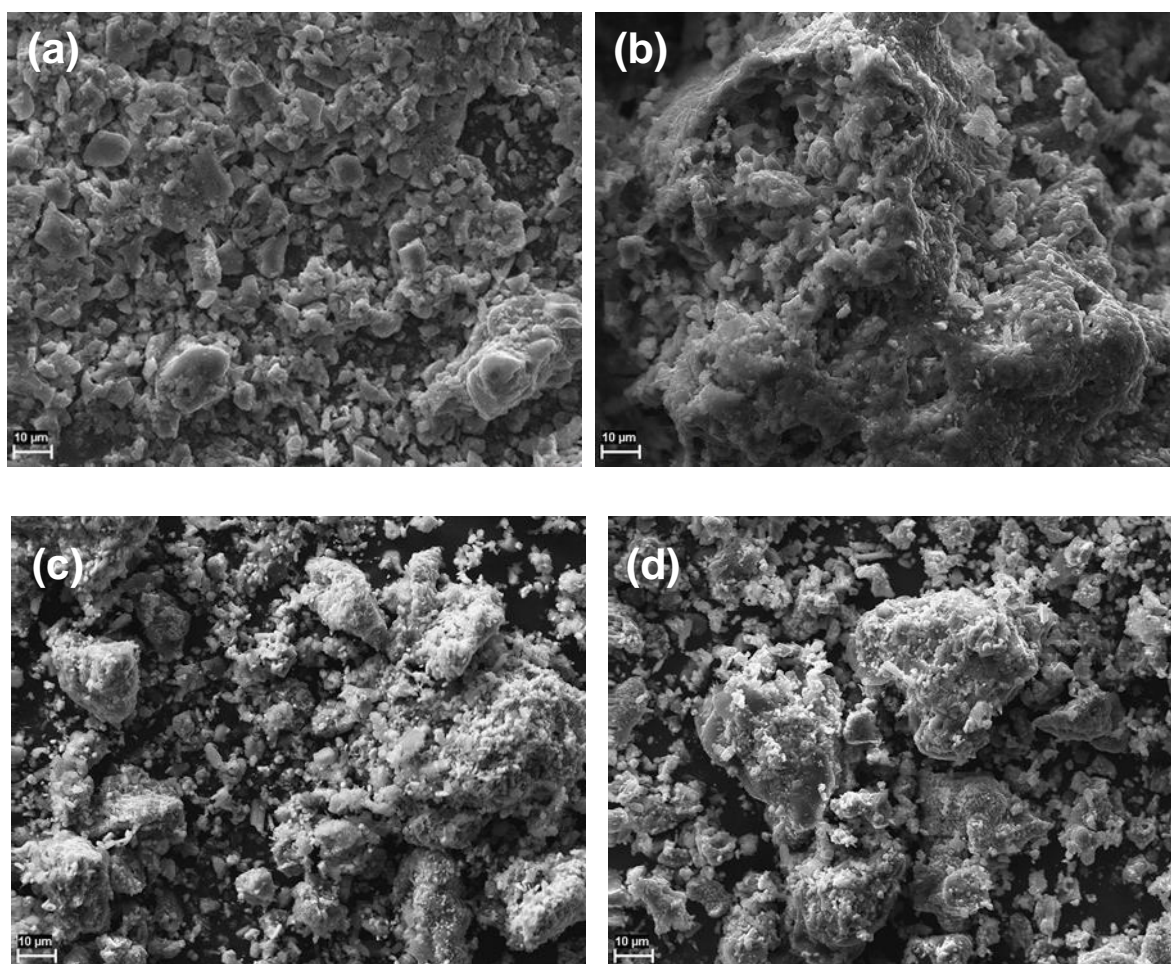


Figure 4.25 SEM images of $\text{Li}_3\text{V}_{1-x}\text{Zn}_x\text{O}_4$ samples: (a) $x = 0$, (b) $x = 0.01$, (c) $x = 0.3$, (d) $x = 0.5$.

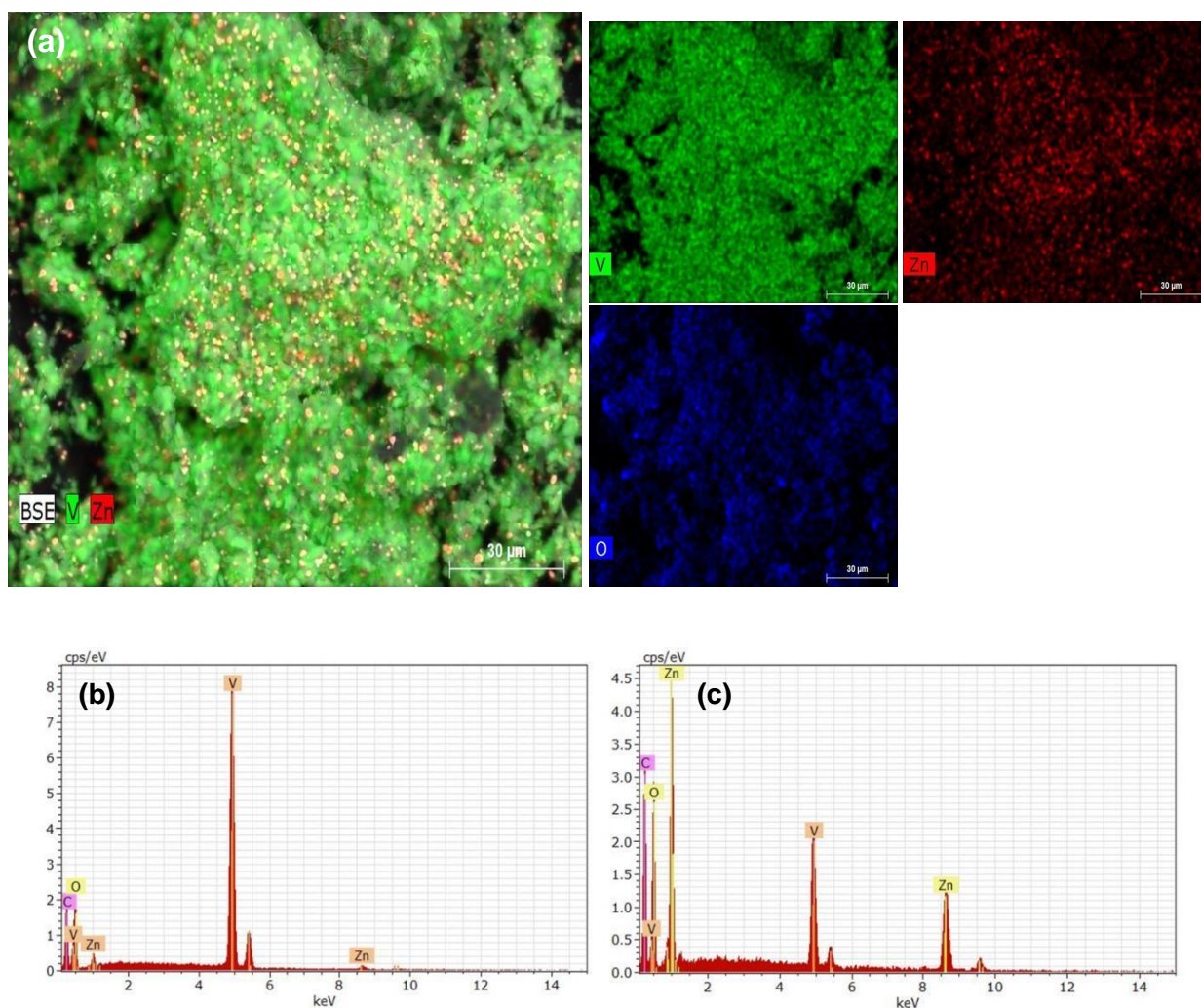


Figure 4.26 (a) EDS mappings of related elements for $\text{Li}_3\text{V}_{1-x}\text{Zn}_x\text{O}_4$ ($x = 0.01$); EDS spectra of (b) $\text{Li}_3\text{V}_{0.95}\text{Zn}_{0.05}\text{O}_4$ and (c) $\text{Li}_3\text{V}_{0.5}\text{Zn}_{0.5}\text{O}_4$.

Table 4.15 Semi-quantitative energy dispersive X-ray microanalysis (wt.%) of the EDS for all the samples.

Sample x	O (wt.%)	V (wt.%)	Zn (wt.%)
0.00	33.5	66.5	
0.01	28.7	67.2	4.0
0.05	33.3	58.5	8.2
0.1	32.7	51.8	15.5
0.3	32.0	31.1	36.8
0.5	31.7	22.6	45.7

5. Conclusions and Future Work

Bifunctional electrolyte additives have been developed and characterized successfully. The 2-((2,2-dimethyl-3,6,9,12-tetraoxa-2-silatetradecan-14-yl)oxy)-1,3-dihydrobenzo[d][1,3,2]diazaphosphole-2-oxide (DTSDP) and 2-phenylbenzo[d][1,3,2]dioxaborole bifunctional electrolyte additives will be beneficial in improving the safety of the LIBs, because of the presence of phosphorus- and boron-containing functional groups that are known to be effective in terms of their fire retardant properties. In addition, nitrogen will produce by-product N_2 that will provide thermal insulation (Fei & Allcock, 2010; Troitzsch, 1998). The presence of boronic ester in the structure is expected to work as a bifunctional additive, facilitating the formation of stable SEI which will stabilize the graphite anode and work as flame retardant (Bebeda and van Ree, 2015).

Doped LVO electrode materials were also developed successfully. The study revealed that the V^{5+} site of the LVO can be doped with Silver (Ag^+), Cerium (Ce^{3+}), Chromium (Cr^{3+}), Magnesium (Mg^{2+}), and Zinc (Zn^{2+}) without affecting the LVO orthorhombic crystal structure as long as the concentration of the dopant is less than or equal to 10%. It has been seen at a high concentration of the dopant result in the introduction of dopant oxide as a secondary impurity phase which could affect the intercalation and deintercalation of lithium ions.

Future work in this project will be to study the performance of the developed materials by preparing coin cells, using the doped LVO as a negative electrode and study its electrochemical behaviour. Future work on the additives will be to study the flame test of the developed bifunctional electrolyte additives and study their effect on electrochemical performance when they are used as electrolyte additives in the commercialized LIBs.

References

- Agubra, V.; Fergus, J. (2013). Lithium-Ion Battery Anode Aging Mechanism. *Materials* 2013, 1310-1325.
- Amine, K.; Liu, J.; Belharouak, I. (2005). High-temperature storage and cycling of CLiFePO_4 /graphite Li-ion cells. *Electrochem. Commun.* 7(7), 669–673.
- An, S.J.; Li, J.; Daniel, C.; Mohanty, D.; Nagpure, S.; Wood, D.L. (2016). The state of understanding of the lithium-ion-battery graphite solid electrolyte interphase (SEI) and its relationship to formation cycling. *Carbon* 105, 52-76.
- Arai, H. (1998). Thermal behavior of $\text{Li}_{1-y}\text{NiO}_2$ and the decomposition mechanism. *Solid State Ionics* 109(3-4), 295–302.
- Armstrong, A.R.; Bruce, P.G. (1996). Synthesis of layered LiMnO_2 as an electrode for rechargeable lithium batteries. *Nature* 381(6582), 499-500.
- Aurbach D.; Markovsky, B.; Levi, M.D.; Levi, E.; Schechter, A.; Moshkovich, M. (1999). New insights into the interactions between electrode materials and electrolyte solutions for advanced nonaqueous batteries. *J. Power Sources* 81– 82, 95–111.
- Baginska, M.; Sottos, N.R.; White, S.R. (2018). Core-Shell Microcapsules Containing Flame Retardant Tris(2-chloroethyl phosphate) for Lithium-Ion Battery Applications. *ACS Omega* 3(2), 1609–1613.
- Bagotsky, V.S. (2005). Fundamentals of Electrochemistry, Vol. 44, John Wiley & Sons, New York.
- Balbuena, P.B.; Wang, Y. (Eds). (2004). Lithium-Ion Batteries: Solid-Electrolyte Interphase. London: Imperial College Press.
- Bard, A.J; Faulkner, L.; Leddy, R.J.; Zoski, C.G. (1980). Electrochemical Methods: Fundamentals and Applications, Vol. 2, Wiley, New York.
- Barsoukov, E.; Kim, J.H.; Kim, D.H.; Hwang, K.S.; Yoon, C.O.; Lee, H. (2000). Parametric analysis using impedance spectroscopy: the relationship between material properties and battery performance, *J. New Mat. Electrochem. Syst.* 3, 303310.
- Bebeda, A.W.; van Ree, T. (2015). Conformational Preferences and Electrochemical Performance of Ethyleneoxy Phenylboronate Electrolyte Additives. *Arab. J. Sci. Engin.* 40, 2841 – 2851.

- Bhagwat, M.; Ramaswamy, A.V.; Tyagi, A.K.; Ramaswamy, V. (2003). Rietveld refinement study of nanocrystalline copper doped zirconia. *Mat. Res. Bull.* 38(13), 1713–1724.
- Bloom, I.; Jones, S.A.; Battaglia, V.S; Henriksen, G.L.; Christophersen, J.P.; Wright, R.B.; Ho, C.D.; Belt, J.R.; Motloch, C.G. (2003). Effect of cathode composition on the capacity fade, impedance rise, and power fade in high-power, lithium-ion cells. *J. Power Sources* 124, 538-550.
- Brain, M. (2006). How Lithium-ion Batteries Work. [<https://electronics.howstuffworks.com/everyday-tech/lithium-ion-battery2.htm>, viewed 09 January 2020],
- Brett, C; Oliveira, A.M. (1993). *Electrochemistry: Principles, Methods, and Applications*, Oxford University Press
- Bruce, P.G; Scrosati, B.; Tarascon, J-M. (2008). Nanomaterials for rechargeable lithium batteries. *Angew. Chem. Int. Ed.* 47, 2930-2946.
- Buqa, H.; Würsig, A.; Vetter, J.; Spahr, M.E.; Krumeich, F.; Novák, P. (2006). SEI film formation on highly crystalline graphitic materials in lithium-ion batteries. *J. Power Sources* 153(2), 385–390.
- Buller, S. (2003). *Impedance-based simulation models for energy storage devices in advanced automotive power systems*, Ph.D. dissertation, ISEA, RWTH Aachen, Aachen, Germany.
- Campion, C.L.; Li, W.; Euler, W.B.; Lucht, B.L.; Ravdel, B.; DiCarlo, J.F.; Abraham, K.M. (2004). Suppression of Toxic Compounds Produced in the Decomposition of Lithium-Ion Battery Electrolytes. *Electrochem. Solid-State Lett.* 7(7), A194.
- Ceder, G.; Mishra, S.K. (1999). Stability of orthorhombic and monoclinic-layered LiMnO_2 . *Electrochem. Solid-State Lett.* 2, 550-552.
- Chen, Y.B.; Hu, Y.; Lian, F.; Liu, Q.G. (2010). Synthesis and characterization of spinel $\text{Li}_{1.05}\text{Cr}_{0.1}\text{Mn}_{1.9}\text{O}_{4-z}\text{F}_z$ as cathode materials for lithium-ion batteries. *Int. J. Metall. Mater.* 17, 220–224.
- Chen, Z.; Amine, K. (2007). Bifunctional electrolyte additive for lithium-ion batteries. *Electrochem. Commun.* 9(4), 703–707.

- Chen, Z.; Qin, Y.; Amine, K.; Sun, Y.-K. (2010). Role of surface coating on cathode materials for lithium-ion batteries. *J. Mat. Chem.* 20(36), 7606.
- Choi, A.; Lim, J.; Kim, H.; Doo, S.W.; Lee, K.T. (2019). In situ Electrochemical Zn^{2+} doping for Mn-rich layered oxides in Li-ion batteries. *ACS Appl. Energy Mater.* 2, 3427–3434
- Cultu, M. (2009). Batteries and their Chemistry, *In: Energy Storage Systems*, Vol. II, Y. Gogus (Ed.), Oxford: EOLSS Publishers.
- Dixon, B.G.; Morris, R.S.; Dallek, S. (2004). Non-flammable polyphosphonate electrolytes. *J. Power Sources* 138, 274–276.
- Feng, J.K.; Cao, Y.L.; Ai, X.P.; Yang, H.X. (2008). Tri-(4-methoxythphenyl) phosphate: A new electrolyte additive with both fire-retardancy and overcharge protection for Li-ion batteries. *Electrochim. Acta* 53(28), 8265–8268.
- Feng, C.Q.; Li, H.; Zhang, P.; Guo, Z.P.; Liu, H.K. (2010). Synthesis and modification of non-stoichiometric spinel ($\text{Li}_{1.02}\text{Mn}_{1.90}\text{Y}_{0.02}\text{O}_{4-y}\text{F}_{0.08}$) for lithium-ion batteries. *Mater. Chem. Phys.* 119, 82–85.
- Hashem, A.; Abdehany, G.; Ashraf, E.; Scheuermann, M.; Sylvio, I.; Ehrenberg, H.; Christian, M. (2019). Doped Nanoscale NMC333 as Cathode Materials for Lilon Batteries. *Materials* 12, 2899.
- Huang, C.; Huang, K.; Wang, H.; Liu, S.; Zeng, Y. (2011). The effect of solid electrolyte interface formation conditions on the aging performance of Li-ion cells. *J. Solid State Electrochem.* 15, 1987-1995.
- Idris, N.H.; Rahman, M.M.; Wang, J.-Z.; Chen, Z.-X.; Liu, H.-K. (2011). Synthesis and electrochemical performance of LiV_3O_8 /carbon nanosheet composite as cathode material for lithium-ion batteries. *Composites Sci. Techn.* 71, 343-349.
- Itou, Y.; Ukyo, Y. (2005). Performance of LiNiCoO_2 materials for advanced lithium ion batteries. *J. Power Sources* 146, 39-44.
- Jeong, G.; Kim, Y.U.; Kim, H.; Kim, Y.J.; Sohn, H.G. (2011). Prospective materials and applications for Li secondary batteries. *Energy Environ. Sci.* 4, 1986–2002.
- Jiang, C.H; Hosono, E.; Zhou, H.S. (2016). Nanomaterials for lithium-ion batteries, *Nano Today* 1, 28–33.
- Joho, F.; Novák, P. (2000). *Electrochim. Acta* 45, 3589-3599.

- Karden, E. (2001). *Using low-frequency impedance spectroscopy for characterization, monitoring, and modeling of industrial batteries*, PhD. dissertation, ISEA, RWTH Aachen, Aachen, Germany
- Lee, H.; Kim, S.; Jeon, J.; Cho, J.J. (2007). *J. Power Sources* 173, 972–978.
- Lee, H.; Lee, J.H.; Ahn, S.; Kim, H.-J.; Cho J.-J. (2006). *Electrochem. Solid-State Lett.* 9, A307–A310.
- Li, T.; Balbuena, P.B. (2000). Theoretical studies of the reduction of ethylene carbonate. *Chem. Phys. Lett.* 317(3–5), 421–429.
- Li, W; Campion, C; Lucht, B.L; Ravdel, B; Dicarlo, J; Abraham, K.M. (2005). *J. Electrochem. Soc.* 152, A1361.
- Liu, P.; Lee, S-H.; Cheong, H.M.; Tracy, C.E.; Pitts, J.R.; Smith, R.D. (2002). Stable Pd/V₂O₅ Optical H₂ Sensor. *J. Electrochem. Soc.* 149, H76-H80.
- Liu, X.M.; Huang, Z.D.; Oh, S.; Ma, P.C.; Chan, P.C.; Vedam, G.K.; Kang, K.; Kim, J.K. (2010). Sol-Gel Synthesis of Multiwalled Carbon Nanotube-LiMn₂O₄ Nanocomposites as Cathode Materials for Li-Ion Batteries. *J. Power Sources* 195, 4290–4296.
- Mai, L.Q.; Gao, Y.; Guan, J.G.; Hu, B.; Xu, L.; Jin, W. (2009). Formation and Lithiation of Ferroselite Nanoflowers as High-energy Li-ion Battery Electrodes. *Int. J. Electrochem. Sci.* 4, 755-761.
- Matadi, B.P.; Geniès, S.; Delaille, A.; Waldmann, T.; Kasper, M.; Wohlfahrt-Mehrens, M.; Aguesse, F.; Bekaert, E.; Jiménez-Gordon, I.; Daniel, L.; Fleury, X.; Bardet, M.; Martin, J.-F.; Bultel, Y. (2017). *J. Electrochem. Soc.* 164, A1089–A1097.
- Minter, S. (2017). Samsung blames faulty batteries for causing Galaxy Note 7 fires, [[https://www.theguardian.com/technology/2017/jan/23/samsung-blamesfaulty](https://www.theguardian.com/technology/2017/jan/23/samsung-blamesfaulty-batteries-for-causing-galaxy-note-7-fires)batteries-for-causing-galaxy-note-7-fires, viewed 09 January 2020].
- MIT (Massachusetts Institute of Technology). (2008). A Guide to Understanding Battery Specifications. [http://web.mit.edu/evt/summary_battery_specifications.pdf, accessed on 21.02.2018]
- Murphy, DW.; Trumbore, F.A. (1976). The Chemistry of TiS₃ and NbSe₃ Cathodes. *J. Electrochem. Soc.* 123, 960-964.

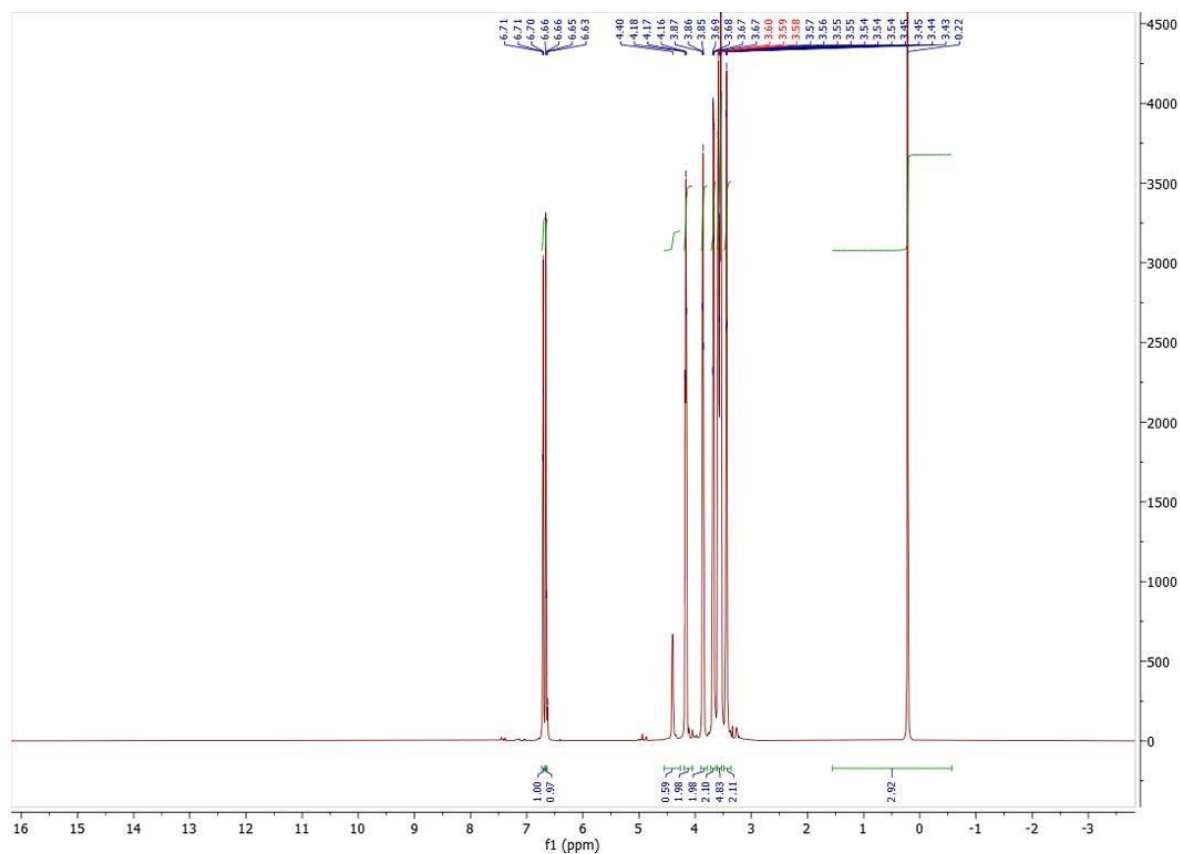
- Okamoto, Y. (2013). *J. Electrochem. Soc.* 160, A404.
- Oswal, M.; Paul, J.; Zhao, R. (2010). A Comparative Study of Lithium-Ion Batteries, Project Report AME578, University of Southern California. [www.ehcar.net/library/rapport/rapport204.pdf, last accessed on 25.01.2018]
- Peng, W. (2011). *Accurate circuit model for predicting the performance of lead-acid AGM batteries*, Master of Science dissertation, University of Nevada, Las Vegas. Available from: UNLV Theses, Dissertations, Professional Papers, and Capstones, 1244. [http://digitalscholarship.unlv.edu/thesesdissertations/1244, last accessed on 25.01.2018]
- Peng, Z.D.; Jiang, Q.L.; Du, K.; Wang, W.G.; Hu, G.R.; Liu, Y.X. Effect of Cr-sources on the performance of $\text{Li}_{1.05}\text{Cr}_{0.04}\text{Mn}_{1.96}\text{O}_4$ cathode materials prepared by the slurry spray drying method. *J. Alloys Compd.* 2010, 493, 640–644.
- Pistoia, G.; Panero, S.; Tocci, M. (1984). Solid solutions $\text{Li}_{1+x}\text{V}_3\text{O}_8$ as cathodes for high rate secondary Li batteries. *Solid State Ionics* 13, 311-318.
- Qi, W.; Chapter, J.G.; Wu, Q.; Yin, T.; Gao, G.; Cui, D. (2017). Nanostructured anode materials for lithium-ion batteries: principle, recent progress, and future perspectives. *J. Mat. Chem. A* 5, 19521–19540.
- Qiao, Y.Q.; Qiao, X.L.; Wang, J.P.; Zhou, J.; Zhang, C.D.; Gu, J.P.; Tu, (2012). Synthesis and electrochemical performance of rod-like LiV_3O_8 cathode materials for rechargeable lithium batteries. *J. Power Sources* 198, 287-293.
- Qu, Q.T.; Zhang, P.; Wang, B.; Chen, Y.H.; Tian, S.; Wu, Y.P.; Holze, R. (2009). *J. Phys. Chem. C* 113, 14020.
- Raja, M.W.; Mahanty, S.; Basu, R.N. (2009). *J. Mater. Chem.* 19, 6161.
- Ramaite, I.D.I.; van Ree, T. (2017). Computational Studies of Substituted Phenylboronic Acids in Common Electrolyte Solvents. *Arab. J. Sci. Engin.* 42, 42274237.
- Rougier, A.; Saadoun, I.; Gravereau, P.; Willmann, P.; Delmas, C. (1996). *Solid State Ionics* 90, 83-90.
- Roy, P.; Srivastava, S.K. (2015). Nanostructured anode materials for lithium-ion batteries. *J. Mat. Chem. A* 3, 2454-2484.
- Safari, M.; Delacourt, C. (2011). *J. Electrochem. Soc.* 158(10), A1123.
- Smith, A.J.; Burns, J.C.d Dahn, J.R. (2011). *Electrochem. Solid-State Lett.*, 14(4), A39.

- Tang, W.; Liu, L.; Tian, S.; Li, L.; Yue, Y.B.; Wu, Y.P.; Guan, S.Y.; Zhu, K. (2010). *Electrochem. Commun.* 12, 1524.
- Tang, W.; Tian, S.; Liu, L.L.; Li, L.; Zhang, H.P.; Yue, Y.B.; Bai, Y.; Wu, Y.P.; Zhu, K. (2011). Nanochain LiMn_2O_4 as ultra-fast cathode material for aqueous rechargeable lithium batteries, *Electrochem. Commun.* 13, 205–208.
- Tarascon, J-M.; Armand, M. (2011). Issues and challenges facing rechargeable lithium batteries. *Nature* 41, 359-367.
- Tweed, K. (2013). Tesla's Lithium-Ion Battery Catches Fire. [https://spectrum.ieee.org/energywise/transportation/advanced-cars/teslaslithiumion-battery-catches-fire, viewed 09 January 2020].
- Verma, P.; Maire, P.; Novak, P. (2010). A Review of the Features and Analyses of the Solid Electrolyte Interphase in Li-Ion Batteries. *Electrochim. Acta* 55(22), 6332–6341.
- Vetter, J.; Novak, P.; Wagner, M.R.; Veit, C.; Moller, K.C.; Besenhard, J.O.; Winter, M.; Wohlfahrt-Mehrens, M.; Vogler, C.; Hammouche, A. (2005). *J. Power Sources* 147, 269-281.
- Wang, B.; Yun, X.Y.; Zhao, S.Y.; Wu, Y.P.; van Ree, T. (2015). Chapter 9: Liquid electrolytes, *In Lithium-ion Batteries: Fundamentals and Applications* (Ed. YP Wu), Boca Raton: CRC Press Taylor&Francis.
- Wang, B.; Qu, Q.T.; Xia, Q.; Wu, Y.P.; Li, X.; Gan, C.L.; van Ree, T. (2008). Effects of 3,5-bis(trifluoromethyl)benzene boronic acid as an additive on the electrochemical performance of propylene carbonate-based electrolytes for lithiumion batteries. *Electrochim. Acta* 54, 816–820
- Wang, Q.; Sun, J.; Yao, X.; Chen, C. (2005) 4-Isopropyl Phenyl Diphenyl Phosphate as Flame-Retardant Additive for Lithium-Ion Battery Electrolyte. *Electrochem. Solid-State Lett.* 8, A467.
- Wang, L.; Li, J.; He, X.; Pu, W.; Wan, C.; Jiang, C. (2009). Recent advances in layered $\text{LiNi}_x\text{Co}_y\text{Mn}_{1-x-y}\text{O}_2$ cathode material for lithium-ion batteries. *J. Solid State Electrochem.* 13, 1157-1164.
- Wang, Y.; Nakamura, S.; Ue, M.; Balbuena, P.B. (2001). Theoretical studies to understand surface chemistry on carbon anodes for lithium-ion batteries: reduction mechanisms of ethylene carbonate. *J. Amer. Chem. Soc.* 123(47), 11708–11718.

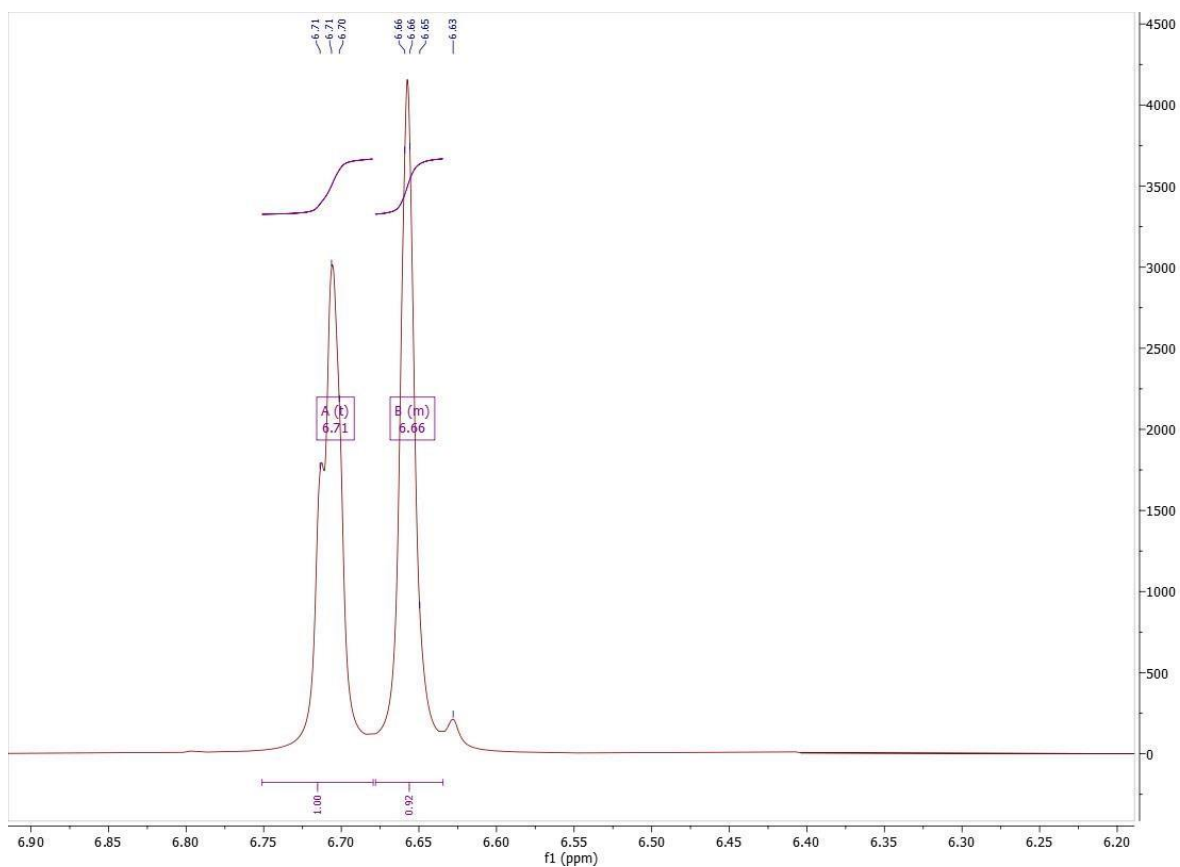
- Wang, Y.; Nakamura, S.; Tasaki, K.; Balbuena, P.B. (2002). *J. Amer. Chem. Soc.* 124, 4408-4421.
- World Energy Council. (2018). World energy Resources. [https://www.worldenergy.org/assets/images/imported/2016/10/World-EnergyResources-Full-report-2018.10.03.pdf, viewed 05 May 2019],
- Wu, Y.P. (Ed). 2015. *Lithium-Ion Batteries: Fundamentals and Applications*. Boca Raton: CRC Press Taylor&Francis.
- Wu, X.; Li, H.; Chen, L.; Huang, X. (2002). *Solid State Ionics* 149, 185-192.
- Wu, Y.P.; Yuan, X.Y.; Zhao, S.Y.; van Ree, T. 2015. Chapter 1. Introduction, *In* Lithium-Ion Batteries: Fundamentals and Applications, YP Wu (Ed). Boca Raton: CRC Press Taylor&Francis.
- Xia, H.; Luo, Z.; Xie, J. (2012). Nanostructured LiMn_2O_4 and their composites as high-performance cathodes for lithium-ion batteries. *Progress in Natural Science: Materials International* 22, 572–584.
- Xu, W.M.; Yuan, A.B.; Tian, L.; Wang, Y.Q. Improved high-rate cyclability of sol-gel derived Cr-doped spinel $\text{LiCr}_y\text{Mn}_{2-y}\text{O}_4$ in an aqueous electrolyte. *J. Appl. Electrochem.* 2011, 41, 453–460
- Xu, K. (2004). Non-aqueous liquid electrolytes for lithium-based rechargeable batteries. *Chem. Rev.* 104, 4303–4417.
- Xu, K.; Zhang, S.S.; Jow, T.R.; Xu, W.; Angell, C.A. (2002). *Electrochem. Solid-State Lett.* 5, A26.
- Yang, X.; Rogach, A.L. (2019). *Electrochemical Techniques in Battery Research: A Tutorial for Nonelectrochemists*. Advanced Energy Materials.
- Yang, S.; Zavalij P.Y.; Whittingham, M.S. (2001). Hydrothermal synthesis of lithium iron phosphate cathodes. *Electrochem. Commun.* 9(3), 505-508
- Yang, L.C.; Gao, Q.S.; Zhang, Y.H.; Tang, Y.; Wu, Y.P. (2008). *Electrochem. Commun.* 10, 118.
- Yang, L.C.; Qu, Q.T.; Shi, Y.; Wu, Y.P.; van Ree, T. (2010). *in*: Małgorzata SopickaLizer (Ed.), High Energy Ball Milling: Mechanochemical Production of Nanopowders, Woodhead Publishing Limited, Oxford, 2010, p. 372.
- Yang, C.R.; Wang, Y.Y.; Wan, C.C. (1998). Composition analysis of the passive film on the carbon electrode of a lithium-ion battery with an EC-based electrolyte. *J. Power Sources* 72, 66-70.

- Zavalis, T.G.; Klett, M.; Kjell, M.H.; Behm, M.; Lindstrom, R.W.; Lindbergh, G. (2013). *Electrochim. Acta* 110 335–348.
- Zhang, S.S. (2006). *J. Power Sources* 162, 1379.
- Zhang, L.; Zhang, Z.; Wu, H.; Amine, K. (2011). Novel redox shuttle additive for high voltage cathode materials. *Energy Env. Sci.* 4(8), 2858.
- Zhang Z. (2015). *Development of advanced materials for rechargeable lithium-ion batteries*, Doctor of Philosophy Thesis, Institute for superconducting and electronic materials, University of Wollongong, p. 52.
[<http://ro.uow.edu.au/theses/4344>, last accessed on 25.01.2018]
- Zhang, J.J.; Yu, A.S. (2015). Nanostructured transition metal oxides as advanced anodes for lithium-ion batteries, *Sci. Bull.* 60 823–838.
- Zhang, Q.F.; Uchaker, E; Candelaria, S.L; Cao, G.Z. (2013). Nanomaterials for energy conversion and storage, *Chem. Soc. Rev.* 42 3127–3171.
- Zhang, Q.; Qiu, C.; Fu, Y.; Ma, X. (2009). Xylene is a new polymerizable additive for overcharge protection of lithium ion batteries. *Chin. J. Chem.* 27, 1459.
- Zheng, J.; Zhang, N.; Wang, N.; Zhao, Y.; Tian, F.; Meng, C. (2016). Facile synthesis and characterization of LiV_3O_8 with sheet-like morphology for high-performance supercapacitors. *Mat. Lett.* 171, 240-243.

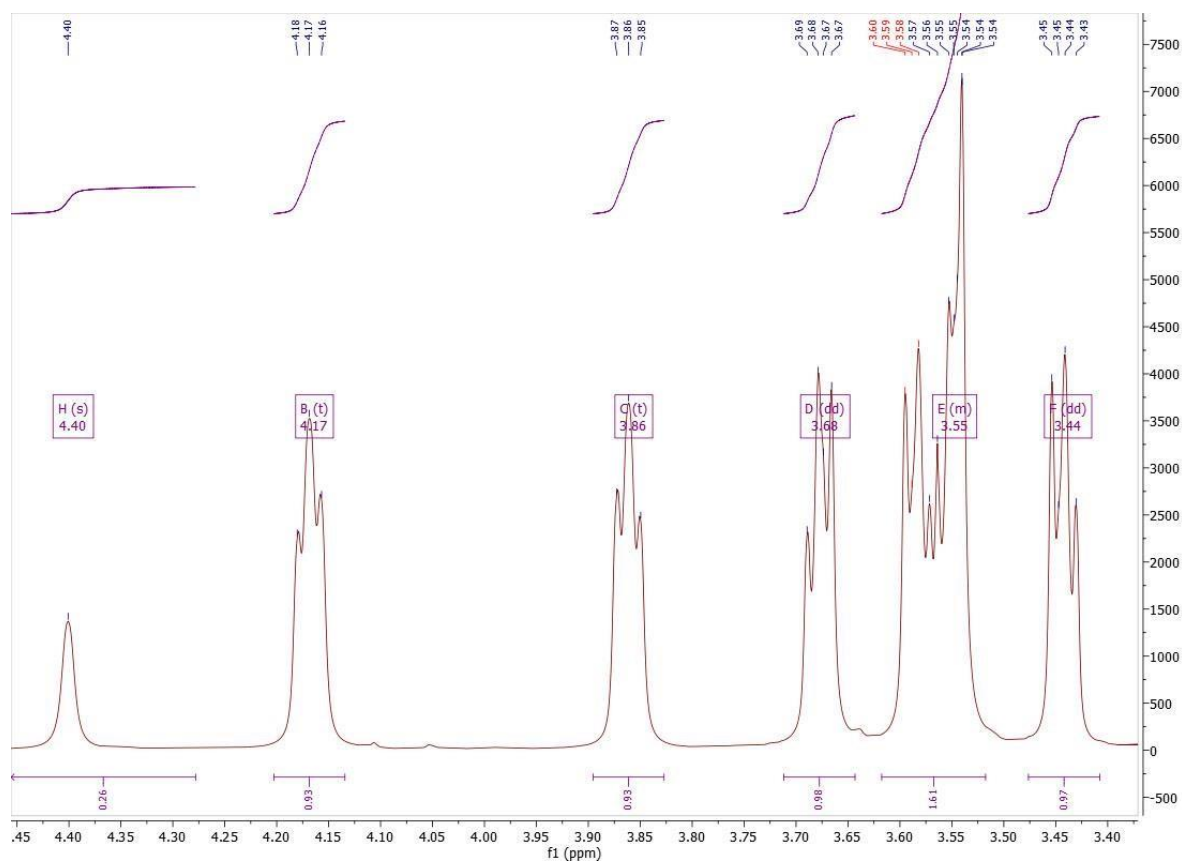
Appendix A NMR Spectra of 2-((2,2-dimethyl-3,6,9,12tetraoxa-2-silatetradecan-14-yl)oxy)-1,3-dihydrobenzo[d][1,3,2]diazaphosphole 2-oxide.



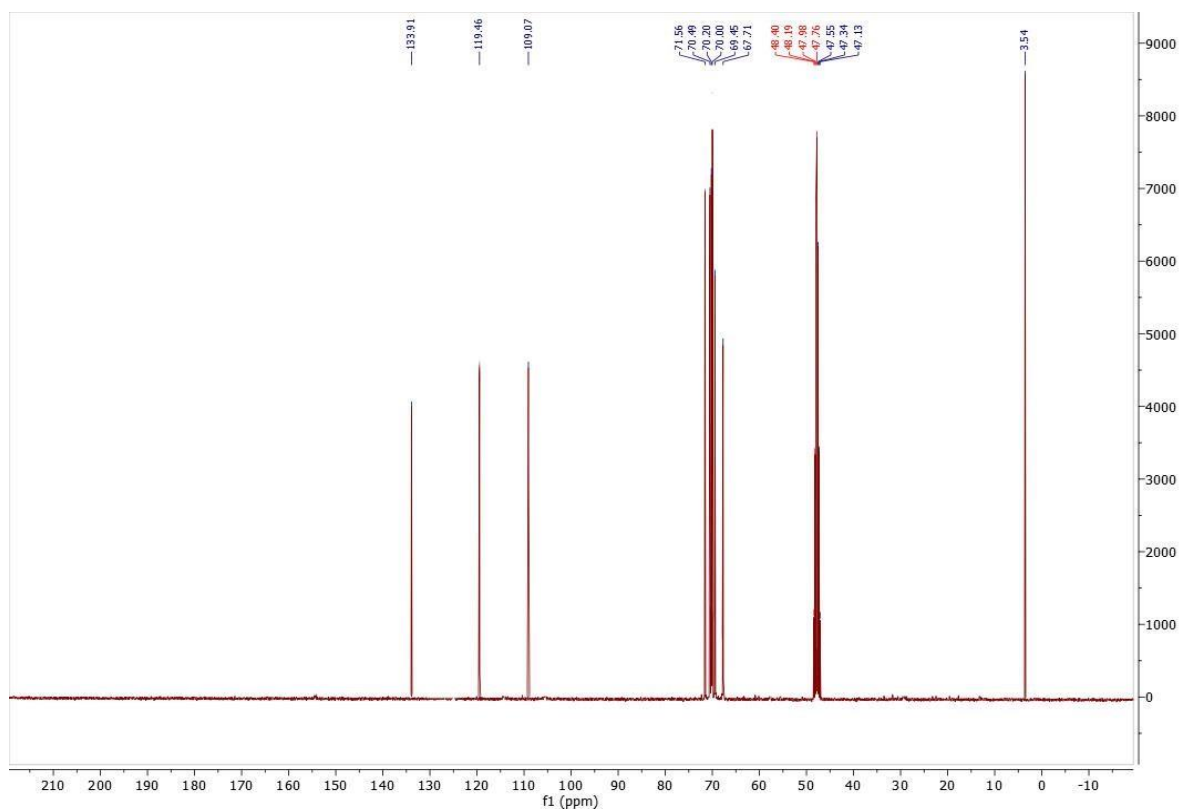
¹H NMR spectrum



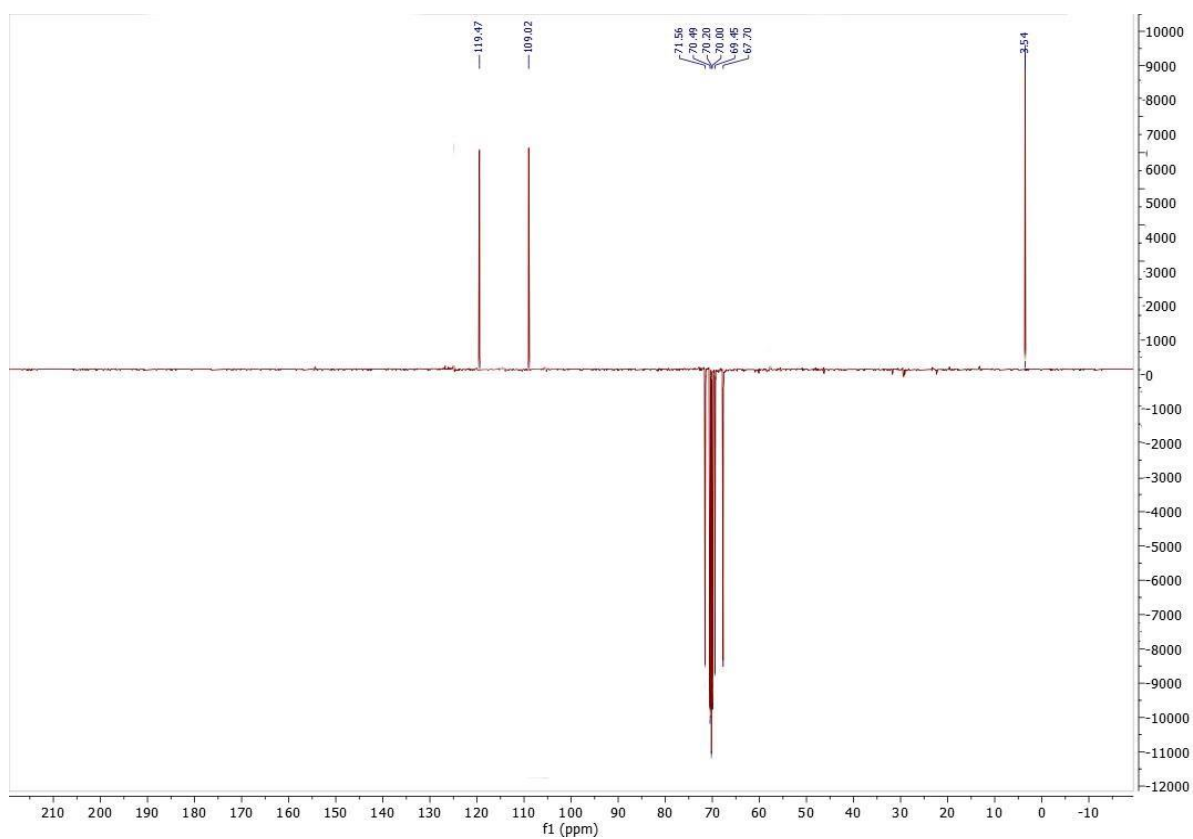
¹H NMR spectrum (aromatic region expansion)



¹H NMR (Aliphatic Region expansion)

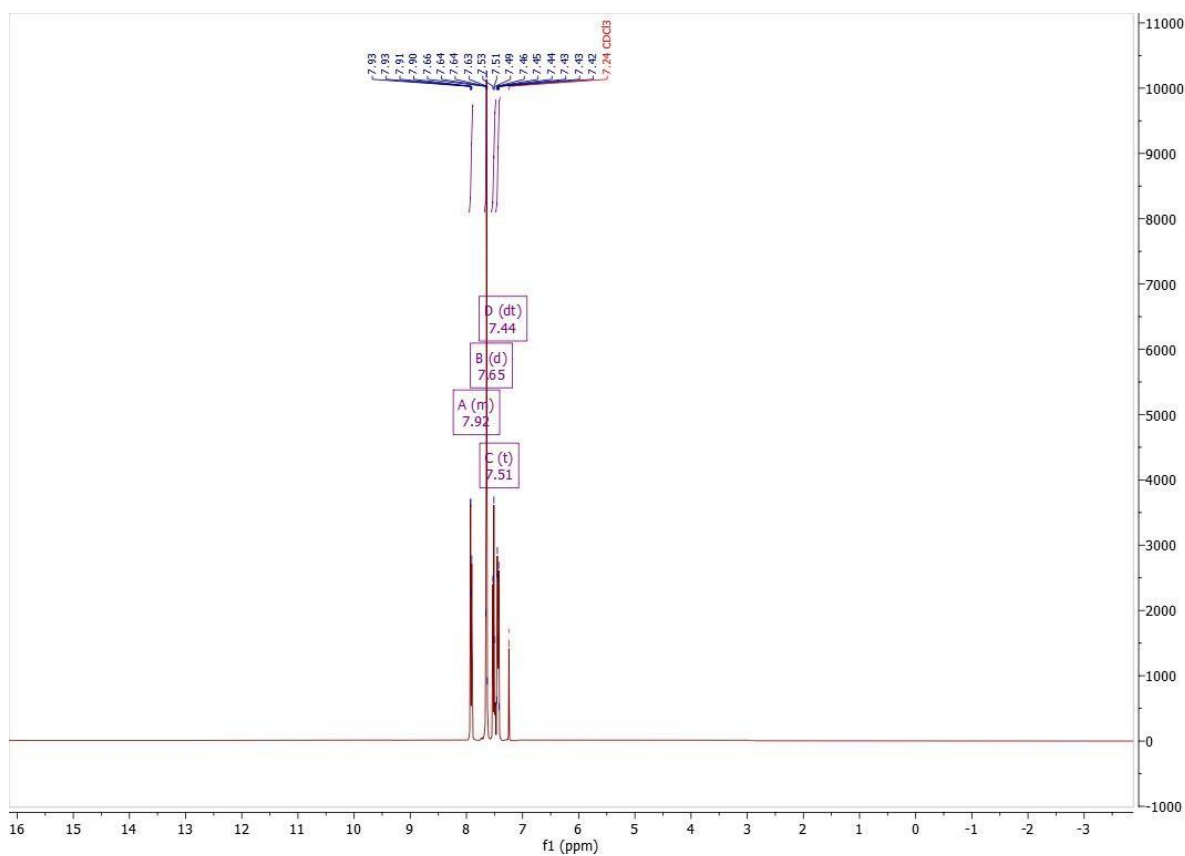


^{13}C NMR spectrum

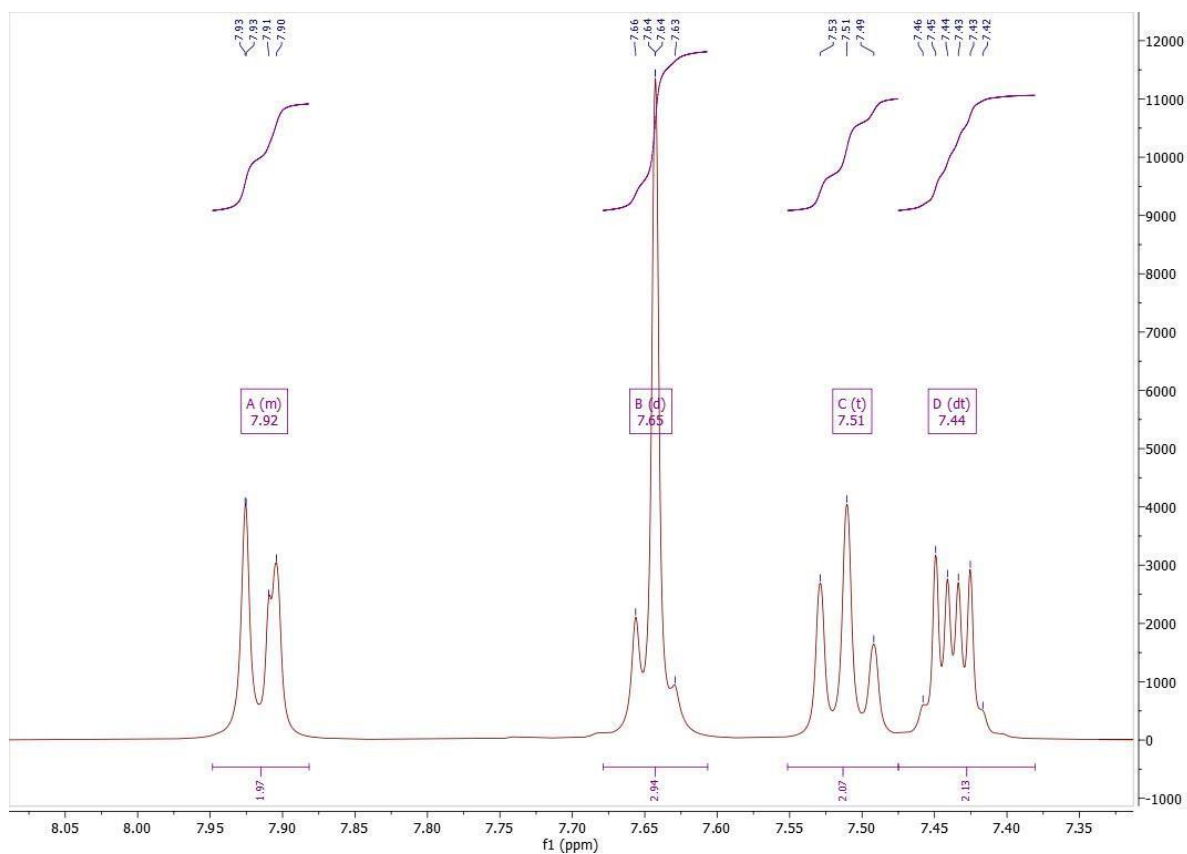


DEPT135 spectrum

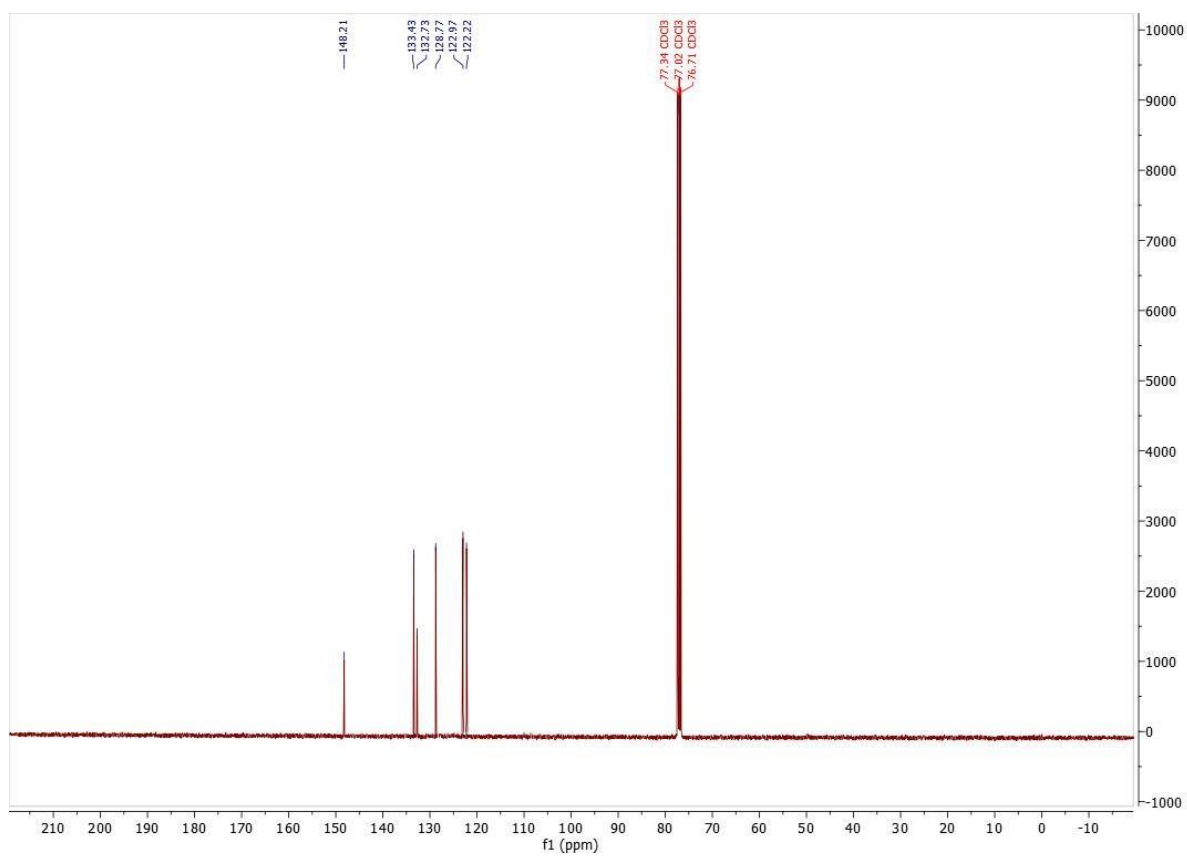
Appendix B NMR Spectra of 2-phenylbenzo[d][1,3,2]dioxaborole



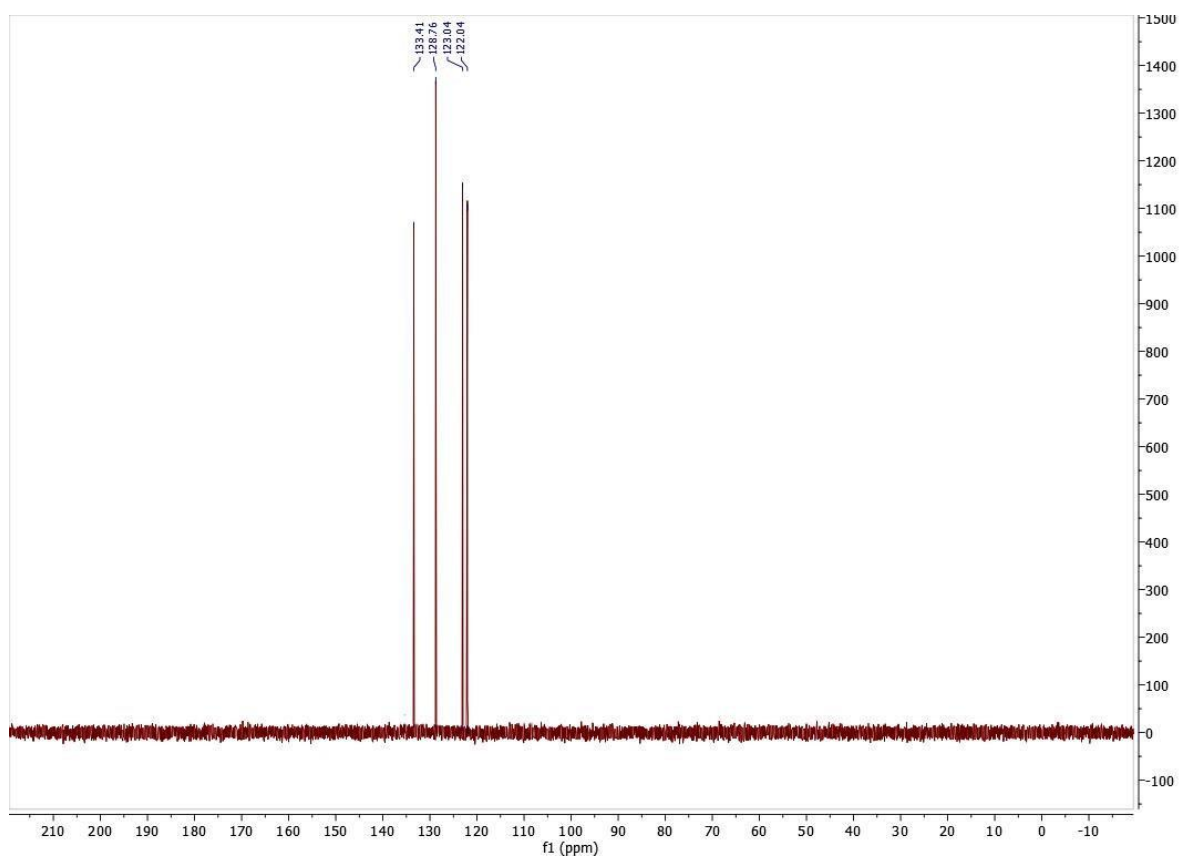
¹H NMR spectrum



¹H NMR spectrum (expansion aromatic region)



¹³C NMR spectrum



DEPT135 NMR spectrum